UNIVERSITÀ DI PARMA

Department of Food and Drug
Laboratories of Biochemistry and Molecular Biology

PhD course in
Drugs, Biomolecules and Health Products
XXX cycle

From molecule to cell: investigation of DNA architecture by Atomic Force and Fluorescence microscopy

Coordinator: Prof. Marco Mor

Tutor: Prof. Claudio Rivetti

PhD student:
Stefano Maggi

Abstract

In living organisms, the spatial organization of genetic information encoded in the molecule of deoxyribonucleic acid (DNA) requires the right balance between the physical properties of the molecule and the biological needs of the cell. DNA is an extremely long polymer when compared to the size of the cell and therefore it requires a high degree of compaction to be contained within the cell envelope. However, the compaction of DNA is at odds with its biological role as various classes of enzymes must have access to information for the development of vital processes.

In cells, a regulatory system is thus established that extends from the nanoscopic dimension of the molecules that mediate biological processes at DNA level, to the microscopic dimension of cellular organelles.

During my doctorate, I studied the spatial organization of DNA at both molecular and cellular levels. In particular, I have dealt with two transcriptional factors of Helicobacter pylori, HpFur and HpNikR, which modulate the architecture and the degree of compaction of DNA by facilitating or hindering the accessibility of RNA polymerase to the arsR gene promoter sequence. The data collected have allowed us to develop a molecular model in which, in the presence of HpFur iron, it is able to multimerize and induce a compaction of the entire promoter sequence, thus preventing the binding of RNA polymerase to DNA. In the absence of iron, however, HpFur changes its quaternary structure and binds a sequence upstream of the promoter, allowing the binding of RNA polymerase to the promoter. The transcription factor HpNikR is only able to bind DNA in the presence of nickel and is able to limit the propagation of promoter compaction, mediated by HpFur in the presence of iron. This control circuit allows Helicobacter pylori to finely control the synthesis of HpArsR depending on the availability of metal cofactors.

During my PhD I also investigated the three-dimensional organization of the whole genome of the model organism *Escherichia coli*. With different number of studies in literature, my study focuses on the analysis of the mechanical properties of the entire genome of the bacterium without proceeding to the lysis of the cell wall, thus disturbing the physiological environment in which the nucleoid is organized.

Escherichia coli cells have been visualized in different growth stages, after several drying procedures or by subjecting the cells to specific intercalating molecules through a combined AFM-FM procedure. The data obtained have allowed us to correlate morphological changes in cells with the state of the nucleoid organized inside them.

The same imaging procedure was also used in the characterization of *E. coli* membrane and nucleoid rearrangements following the expression of a small hydrophobic peptide (Lpt) belonging to the toxin-antitoxin type I system of *Lactobacillus rhamnosus*. The expression of toxin causes a significant general morphological refraction of the cell, which manifests itself through the formation of hole-like structures on the membrane and the compaction of the bacterial nucleoid. The data collected have demonstrated the toxic nature of peptide, highlighting its tendency to damage the structural integrity of the membrane.

Summary

General introduction

Recording information on a storage medium has been one of the major breakthrough of human being and the development of high capacity storage media, from paper to silicon chip, has been a human challenge.

Evolution over its million years of selecting pressure has "elected" the Deoxyribonucleic acid (DNA) as an ideal supporting medium for storing the information of life processes. DNA is a very stable molecule in cold, dry and dark conditions and can store huge amount of information in a very little weight. George Church, Sri Kosuri, and colleagues encoded a 52,000-word book in thousands of snippets of DNA. Their particular encoding scheme could store 1.28 million gigabytes per gram of DNA.

DNA is an organic polymer consisting of two polynucleotide chains wound on one another in the double helical structure. A nucleotide consists of a phosphate group, a 2'-deoxyribose and one of the four nitrogenous bases adenine, guanine, cytosine and thymine that bind the deoxyribose with a N-glycosidic bond.

The nucleotides are linked together in polynucleotide chains by means of a phosphodiester linkage between the 3' hydroxyl group of one nucleotide and the 5' phosphate group of the another nucleotide. The phosphodiester linkage forms a repetitive sugar-phosphate scaffold which is a constant structural feature of DNA, while the sequence of the nitrogen bases along the chain encodes the genetic information.

Of the three possible helix conformations, A-DNA, B-DNA and Z-DNA, the B form is believed to predominates in cells. The B-helix is 23.7 Å wide and extends 34 Å per 10 bp of sequence and makes one complete turn about its axis every 10.4-10.5 base pairs. Although these topological dimensions could appear very small, it has to be considered that a complete genome reaches dimensions in the range of millions base pairs in bacteria and billions base pairs in high order organisms. Thus, given the small dimensions of the cell envelope, the DNA need to be organized into highly compacted structures. For

instance, the bacteriophage T7 genome is 4×10^4 bp long with a physical length of 14 µm and an unconstrained volume of about 2 µm^3. This DNA is packed into a capsid of only 9×10^{-5} µm^3, with an overall DNA compaction of about 22000-fold . Within the capsid DNA is so concentrated that it reaches a hexagonal crystalline phase [1]. Such an high DNA concentration is not in contrast with the processes of life because much of virus biogenesis (DNA replication, transcription, capsid assembly etc.) occurs outside the capsid exploiting the biochemical machinery of the bacterial host, thus making the capsid fully available for the DNA storage. Likewise, the 5 Mbp genome of an *Escherichia coli* cell is about 1.5 mm long with an unconstrained volume of 200 µm^3 [2]. It is contained in an envelope of about 1 µm^3, of which about one half is occupied by DNA [3], thus resulting in a DNA compaction of at least 400-fold. Bacteria achieve such a high degree of DNA compaction by supercoiling the DNA by mean of proteins (NAP) which pack the DNA into a compact structure called nucleoid. DNA compaction is a carefully regulated process since the compaction of the nucleoid is in contrast with DNA metabolism and gene expression.

In the introductory chapter, I review current knowledge of the mechanisms through which the long genomic DNA molecule can be compacted and folded into a highly dynamic nucleoid structure that fulfills the requirements for accomplishing crucial vital processes.

Then I describe the work published in the article "Metal-responsive promoter DNA compaction by the ferric uptake regulator". This work was done in collaboration with Prof. Danielli (University of Bologna), it was possible to analyze how the binding of two proteins to DNA is able to modulate the spatial organization of the transcription promoting sequence.. Atomic Force Microscopy was employed to collect high resolution images of nucleoprotein complexes. Variation of the DNA contour length and volumetric analysis of DNA-protein complexes has led to the determination of both the oligomeric state and binding stoichiometry of the bound protein. A molecular model describing the

interaction of the two transcriptional factors with the promoter and their role in gene expression control was proposed.

Finally, I describe the development and the use of a combined atomic force and fluorescence microscopy approach to investigate the *E. coli* nucleoid conformation under different growth conditions. By means of this technique, I was able to characterized the shape of the bacterial nucleoid at different resolutions. The procedure was also applied to study the nucleoid compaction and membrane damage caused by the expression of a small hydrophobic peptide belonging to a type I toxin-antitoxin system of *Lactobacillus rhamnosus*.

Physical forces compacting the nucleoid: Supercoiling

DNA is a flexible molecule and the structural parameters that characterize it depend on the ionic conditions of the environment and on the nature of the proteins that bind to it . Bacteria reduce the volume of the genome exploiting the torsional constrain of topologically closed DNA known as DNA supercoiling. Bacteria have many enzymes capable of changing the topology of DNA in order to accumulate supercoiling . The Escherichia coli genome is circular covalently closed molecule (cccDNA) and its topology can be quantitatively described by the linking number (Lk) that is the sum of the number of times the helix winds around its central axis (called twist, Tw) and the number of times the helix crosses itself (called writhe Wr).

The difference between the linking number of the supercoiled state (Lk) and the relaxed state (Lk_0) is defined ΔLk. ΔLk is positive for positively supercoiled DNA, negative for negatively supercoiled DNA.

Since ΔLk depends on the length of the DNA it is sometimes useful to define the DNA supercoiling in terms of superhelical density ($\sigma = \Delta Lk/Lk0$).The *E. coli* genome has a $\sigma = -0.06$ [4]. The biological meaning of a negative σ value lies in the fact that negatively supercoiled DNA can assist biological processes, such as transcription and replication, that require the separation of the two DNA strands.

The superhelical density of chromosomal DNA must be within ±20% the normal σ value for cell growth [5]. Hypo-supercoiling causes segregation problems [6,7] and leads to poor chromosome function that can be toxic or lethal [8] . Hyper-supercoiling promotes the formation of Z-DNA at positions with long alternating GC or AT base pairs, causing the extrusion of cruciforms at inverted repeats and stabilizing other unusual structures such as inter- and intra-molecular DNA triplex helix and R-loops [9].

The supercoil density can occur in two forms: diffusible supercoil density (σD) that moves freely around the chromosome in 10 kb domains, and constrained supercoil density (σC)

resulting   from the binding nucleoid associated proteins (NAPs) that bend, loop, or unwind DNA at many sites.

Topoisomerases are proteins capable of changing the DNA supercoiling: Type I topoisomerases relax (−) supercoils, and DNA gyrase on the contrary is the only topoisomerase that can increase the (−) supercoiling of relaxed plasmids.

The homeostatic supercoil control mechanism was proposed by Menzel and Gellert and postulates that when DNA becomes hyper-supercoiled, the Topo I promoter is activated to recruit RNAP and increase the relaxing potential by synthetizing more cellular Topo I. When DNA becomes relaxed, gyrA and gyrB promoters are activated to produce gyrase in order to increase negative supercoiling. The homeostatic supercoil control mechanism is not the only factor controlling the levels of DNA supercoiling, in fact, a 10% increase or decrease in the expression levels of gyrase or Topo I only results in a 1.5% change in supercoiling density [10].

Gene transcription *per se* can vary the degree of DNA supercoiling. Liu and Wang proposed the twin domain model [11], by which, in bacteria, as transcription and translation are coupled to DNA, large biological complexes are formed consisting of RNA polymerase molecules, mRNA and translating ribosomes that would require the template DNA to rotate along its axis rather than the RNA polymerase rotating around the double helix. The model predicts domains of negative supercoiling being generated behind the transcription/translation machinery and positive supercoiling accumulating downstream of the machinery. This model, which was demonstrated for *rrnG* operon of *Salmonella enterica* [12], underlines the large impact of transcription on supercoiling since highly transcribed genes, as the *rRNA* operons, can carry up to 50 RNAP creating a huge torsional stress that could stop supercoil diffusion. For these reasons, RNAP can be considered as a chromosome domain boundary maker [10].

Diffusible supercoiling (σD) causes DNA to collapse into a tightly interwound plectonemic structure, which represents the first level of a DNA condensation that permit to a 4.6

5

Mbp chromosome to fit into the small space available in a bacterial cell [10]. This plectonemic structure has been visualized by means of EM by Prof. Kavenoff (Figure2)[13].

This plectonemic structure is organized into topological domains that are insulated from their immediate neighbors and are on average 10 kb in length and, more importantly, their boundaries are dynamic[14] .

Recent experiments with 45.7Kbp cosmid, revealed that, in the presence of attractive DNA−DNA interactions, plectonemes were packed into a single higher-order filament called hyperplectoneme[15] (Figure 2).
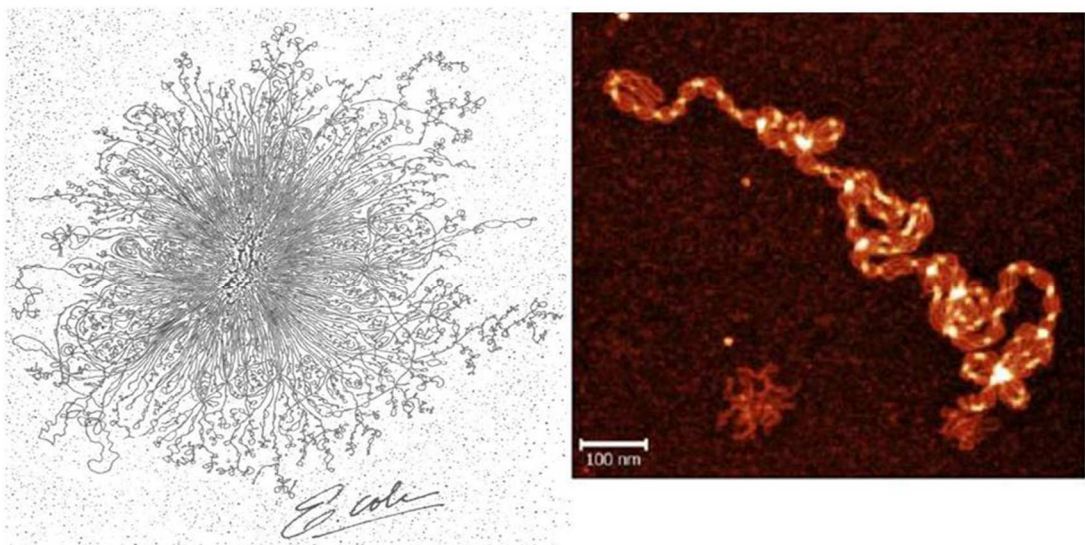
Figure 2. EM image of isolated nucleoid f *E. coli* [13](left panel). Hyperplectonemes folding of a 45,7 Mbp cosmid [15].

In addition to its functional rule in DNA packaging super helical density is a parameter that reflect metabolic state of the cell: the ATP-dependent DNA-supercoiling activity of DNA gyrase ensure that when ATP/ADP concentration drops due to nutrient starvation or stress, the superhelical density will decrease. A decrease in superelical density is a key

feature enhancing transcription of RNAPσ^{38} dependent gene leading to adaptation to stress conditions [16].

Physical forces compacting the nucleoid: Macromolecular Crowding

The term "macromolecular crowding" refers to non-specific effects caused by high concentrations of background macromolecules in cells.

The interior of *E. coli* can be considered crowded because, besides DNA, proteins and RNA are present in concentrations of 300-400 gL^{-1}.

In order to understand the role of macromolecular crowning on chromosome folding I will consider the cross interaction in a mixture of two, different sized, hard spheres.

In dilute solutions the small spheres are excluded from a layer of thickness r around the big spheres called the depletion zone (figure 1A). At high concentrations, when two large spheres approach each other to a distance smaller than radius of the small spheres, the depletion zones start to overlap (figure 1B) so that the small spheres are depleted from the void between the two big particles. At concentrations where the gap between the two spheres is smaller than 2r, the depletion zones start overlapping and the small particles are expelled from the space between the large particles. A consequence of these so-called depletion interactions is that the small spheres experience a decrease in their freedom of motion or translational entropy. Moving the big spheres together (figure 1C) results in an overlap of the depletion layers and thus in a decrease in the volume excluded to the small spheres. This gain in entropy reduces the total free energy of the system. To simulate the crowded cytoplasmatic environment on isolated nucleoid Pelletier et colleague [17] used high molecular weight polyethylene glycol (PEG20000) and monitored the genome folding over time using a micro chamber device coupled with a fluorescence microscope. The work clearly demonstrate that molecular crowning can cause compaction at in vivo concentration of depletants (0,1-0,2 g/ml).

Furthermore, because depletion interactions tend to reduce inter-DNA spacing and thus enhance looping, molecular crowding may indirectly enhance binding of nucleoid-associated proteins to DNA [17].

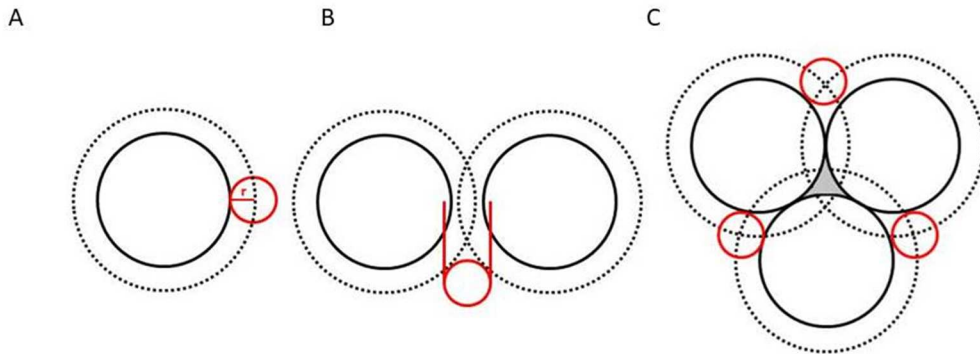**Figure 1. A)** In diluted solutions when two molecule of different radius interact there is the formation of a deplation zone (dotted circol); **B)** At higher concentration the depletion zones start to overlap if the distance between them is smaller than the radius of the smallest molecule. **C)** At very high concentration the big molecules are so close as to reduce the total volume accessible to the small molecules.

The nucleoid associated proteins (NAP)

The nucleoid associated proteins (NAP) are a group of small, generally basic proteins that are able to bind both specific and non-specific DNA and induce bending, wrapping or bridging of the genome. As mentioned earlier, supercoiling is one of the major processes through which the genome of *E. coli* is compacted. The supercoiling imposed topology is fragile without additional stabilization since single strand breaks would relax hundreds of kilobases of the *E. coli* chromosome causing cell death.

NAPs through their ability to bend and making contact points between distant regions of the chromosome contribute to the formation and stabilization of topologically closed regions of about 10 kb named microdomain .

Beside organizing the lowest level of genome architecture, NAPs play also an important role in cellular processes such as transcription, recombination, nucleoid segregation, and DNA storage.

Based on the architecture imposed to DNA, NAPs can be classified as DNA bridging proteins, DNA bending proteins and DNA compacting proteins. A particular type of DNA binding protein are able to cluster plectonemic domains forming macrodomain (MD), that are specific spatial arrangement of large DNA regions displaying higher interaction frequencies [18].

DNA bridging proteins

Histone-like nucleoid structuring protein (H-NS)

E. coli H-NS (histone-like nucleoid structuring protein) is a 137 amino acids long protein, consisting of three domains: an N-terminal domain(NTD), a carboxy-terminal domain (CTD) and a flexible linker that connects the two. The precise structure of H-NS is unknown since the structure of the full-length H-NS protein has not been resolved yet.

An AT-hook motif located in the CDT is responsible for the DNA binding activity of H-NS[19]: R114 can interact with the minor grove of the DNA and this interaction is favored by AT-rich sequences that exhibit a narrow minor groove. For this reason H-NS is capable to bind DNA without any sequence specificity even though it displays a preferential binding for bent and/or flexible DNA. AFM images of HNS nucleoprotein complexes revealed that at high concentration (H-NS–bp ratio 0.1:1), the DNA showed a repetitive bridged organization that could be quantified in a 20 ± 3 nm periodic structure[15].

The H-NS aptitude to form bridged structures on the DNA makes it a gateway able to preserve supercoiling even in nicked DNA.

The ability to recognize A-T rich sequences, makes H-NS to compete with RNA polymerase. In fact i) H-NS binds to the TATA box preventing RNA polymerase promoter binding; ii) H-NS appears to interact directly with the RNA polymerase alpha subunit to prevent transcription initiation; iii) RNA polymerase loop-mediated trapping [20].

Super resolution analysis of H-NS discovered a clustered distribution with 2-4 spots, following cell division [21]. The authors hypothesize that H-NS can function as anchor points for distant DNA loci distributed throughout the genome, potentially stabilizing DNA loops. These anchor points (or organizing centers) can act in concert with previously described chromosome domains to shape the architecture of the *E.coli* chromosome. However, this study also revealed that while the H-NS clusters appeared largely static, the H-NS specific

genes were mobile and did not always co-localize with the H-NS clusters, suggesting that the nucleoprotein complex is a heterogeneous and dynamic entity.

Leucine-responsive Regulatory Protein (Lrp)

Lrp is a 15 kDa protein that binds a DNA degenerate consensus sequence and influences the transcription of $\cong$ 10% of the *E. coli* genes and its activity can be potentiated, inhibited or unaffected by leucine [22] . Lrp exists in different oligomeric forms: dimer, octamer and hexadecamer, with leucine binding favoring the dissociation of the hexadecamer to the octamer form [23]. The N-terminus consist of three α-helices that adopt a helix-turn-helix motif which is believed to mediate the interaction with DNA [24]. As shown by electron microscopy images of *B. subtilis* LrpC–DNA complexes, Lrp can bridge and wrap the DNA duplex [25]. Among the gene influenced by Lrp, the most important are the rRNA operons (that are inhibited) and genes involved in the phase-variable expression of pili (that are induced). The phase-variable expression of pili and rRNA is mediated by a positive control of the alormone ppGpp on the expression of *lrp* gene, but the molecular mechanism are still unknown [26]. This means that Lrp levels are highest at the end of the exponential phase of growth, when the demand for stable RNA and other components of the translational machinery is declining and the bacterium needs high mobility in order to search for nutrient.

MukB

Escherichia coli MukB was the first member of the structural maintenance of chromosomes (SMC) protein family to be discovered. MukB mutants cause the production of anucleate cells, cells with two nucleoids, and cells with small amounts of DNA caused by a "guillotine effect" [27].

MukB consists of two globular (the N- and C-terminal) domains connected by two long α-helices with a hinge region in between [28]. In solution MukB dimerizes via the hinge

domain to form a distinctive V-shaped molecule where two long coiled-coils protruding from the hinge terminate in globular head domains [29]. The DNA binding site is located on the positively charged hinge-proximal side of the head domain and spreads over its sides. The proteins MukE and MukF bind MukB [30]. MukEF does not show any DNA binding activity but it modulates MukB-DNA interactions[31]. MukF serves as a kleisin that interacts with MukB heads and links MukE to the complex.

When overproduced in living cells [32] or mixed in vitro with long phage DNA [33], MukB induces DNA condensation. The mechanism by which MukB condenses DNA is unknown. Presumably, by trapping distal segments of the chromosome or by forming loops between DNA segments.

Perhaps the most striking feature of MukB hinge is its association with ParC, a subunit of DNA topoisomerase IV [34,35]. Although this association is rather weak, it seems essential. Mutations in ParC or MukB that disrupt their interface are detrimental for the cell[36]. Because the interaction is fairly weak, it is unclear whether ParC should be viewed as a part of MukBEF complex or a transient cofactor. Specifically, MukB stimulates topo IV-catalyzed relaxation of negatively supercoiled DNA but has no effect on relaxation of positive supercoils or decatenation and promotes DNA knotting [37]. How topo IV affects reactions of MukBEF is yet to be determined.

Fluorescence images indicates that MukBEF accumulates as 'spots' at ~1-3 discrete chromosome locations, typically at midcell and/or quarter cell, in the same regions as the replication origins in *E. coli*, but no polar anchoring complex has been identified. However, MukBEF in *E. coli* is required to maintain the correct genome orientation inside the cell [38].

DNA bending proteins

Integration host factor (IHF)

IHF was originally discovered as an essential co-factor for site-specific recombination of phage lambda in *E. coli* and is composed of two subunits, α-subunit and β-subunit. The α-subunit t is 11kDa and the β-subunit about 9.5kDa in size. The structure of the hetero-dimeric protein has been resolved and can be described as a body with protruding flexible arms [39]. The compact body of IHF is made of intertwined α-helices from both IHF subunits. This compact body is capped by β -sheets that extends into two flexible β-ribbon arms that can be inserted into the minor groove of DNA [39,40]. At the tip of each β -ribbon arm that is inserted into the minor groove upon binding there is a highly conserved Proline. This residue intercalates between adjacent base pairs and induces or stabilizes DNA bending. The insertion of the two Proline residues (one from each β-ribbon arm) results in extensive hydrophobic interactions with the DNA bases, which leads to an unusual narrow minor groove. This in turn leads to two sharp kinks at the sites were the β-arms are inserted (9 bp apart), which results in sharp DNA bending (up to 180°) [39]. The DNA bend is stabilized by interactions between the negatively charged DNA sugar-phosphate backbone and positively charged residues along the body of IHF [40]. The binding of IHF to DNA can result in up to 30% length reduction attributed to bending [41].

The IHF DNA-bending activity can influence transcription by facilitating, upon bending, contact between regulatory proteins and RNA polymerase [42] but also by means of a mechanism called supercoiling-induced duplex destabilization(SIDD): IHF-binding site display a tendency of becoming single-stranded and upon IHF-induced DNA bending, this tendency is transferred to the next-nearest labile region, mediated by displacement of the torsional energy that arises from DNA twist in negatively supercoiled DNA. This mechanism assists the formation of the single-stranded 'bubble' necessary for the formation of the open transcription complex [43].

Because, in vivo, the majority of IHF is bound to the DNA, [44,45] the non-specific binding is frequent and probably important.

The observation that non-specific binding and bending leads to effective compaction *in vitro* suggests that IHF contributes significantly to the compact form of the nucleoid *in vivo*, in particular during early stationary growth .

The factor for inversion stimulation (FIS)

The factor for inversion stimulation (Fis) is a 22kDa homo-dimeric protein and the structure of the nucleoprotein complex has been resolved [46]. A helix-turn-helix motif is involved in DNA binding [47,48].

FIS inserts an alpha helix of each monomer into two consecutive major grooves where it mkes non-specific bonds, however, for the complex to be stable the minor groove towards the protein has to be narrowed. For this reason, the sequence showing greater affinity is composed of a rich AT central region that better accommodates this narrowed conformation.

Depending on the core sequence, the DNA adopts an overall curvatures ranging from 60° to 75° as measured in the crystals.

There are approximately 6000 sites in the genome that match the consensus sequence, which leaves the majority of Fis (during early exponential growth) capable of binding non-specifically to DNA. Studies of FIS action at individual regulatory regions have revealed different mechanisms by which it affects gene expression: direct interaction with αCTD of RNA polymerase; competition of RNA polymerase binding site; displacement of an essential trancription activator; jamming of RNA polymerase and, as HIF, SIDD. The ability to regulate the expression of the two major topoisomerases (*topA* 88 and DNA gyrase) allows Fis to influence DNA supercoiling globally [49–51]. It has also been suggested that Fis

can preserve a negatively supercoiled DNA micro-domain at the some promoters by constrains negative supercoils upon binding to its sites [52].

It is interesting to note that Fis is the most abundant NAP in early exponentially growing cells (1 Fis/450 bp), on the contrary is completely absent during stationary growth. This expression pattern seems to correlate with the rise in demand for components of the translation apparatus to support rapid growth [53].

HU

In *E. coli*, Hu exists as homodimer or heterodimer made of 9.5kDa subunitswith 70% homology, depending on the stage of growth of the bacterium. Homodimeric HUα_2 is more abundant at the beginning of logarithmic growth, whereas heterodimeric HU$\alpha\beta$ predominates late in growth and during the stationary phase [54]. HU and IHF have a similar structure, in which two β-ribbon arms protrude from a globular body. They share about 30–40% homology but HU binds DNA non-specifically, with a higher affinity for supercoiled DNA and distorted DNA structures, such as bends or four-way junctions [55].

Like IHF, HU employs the intercalation of two conserved Proline residues that are inserted into the minor groove and stabilize DNA bending. In addition, X-ray crystallography of HU-DNA complexes has revealed that the protein can form multimers consisting of octamers organized in a left-handed αβ spiral. The physiological role of high order multimers is emphasized by the fact replacement of the HUβ-E38A residue, critical for interdimeric interface, significantly decreased the ability in generating negative DNA supercoils compared to the wild type [56]. However, in vivo evidence that multimeric HU is the biological unit are lacking.

In addition to its influence on DNA bending , HU contributes to relieve extra DNA supercoiling by binding and stabilizing cruciform structures since, in vitro, it binds with high affinity to such structures [57,58]. HU is also able to bind RNA, and induce an RNA dependent DNA condensation in vitro, but the mechanism is unknown[59].

DNA compacting proteins

The DNA protection during starvation protein (Dps)

Dps is a member of the ferritin/bacterioferritin superfamily that becomes the most abundant protein upon entering the stationary phase (180 000 molecules per cell) [60]. The Dps monomer is a 19kDa protein with a four helix bundle core resembling the monomer core of bacterial ferritin[61]. Like bacterial ferritin, Dps forms dodecamers resulting in a large (90Å) hollow sphere[61]. Both inner and outer surfaces of the *E. coli* Dps are charged negatively, based on the X-ray structure [61] and AFM analysis [62]. It is thought that the N-terminal tails, lacking a DNA-binding module, but containing positively charged amino acid residues, are responsible for interaction with DNA, Dps self-aggregation and binding/aggregation-mediated DNA condensation [63]. Recent experiments have revealed that Dps can interact within or nearby the sequence responsible for the starting of genome replication during exponential phase, thus inducing a delay in the genome replication [64]. The genomic regions bound by Dps in this area contain many repeated sequences, including three pairs of inverted heptanucleotides within the origin. Thus, it is possible that inverted repeats, forming a 4-way junction create a platform for interaction with the Dps-DnaA sub-molecular complex. Indeed, in vitro experiments show that Dps has a high affinity for three-way junctions in artificial DNA molecules. Despite the DNA binding mode, the Dps molecular mechanism is still poorly understood. During stationary phase DPS co-crystalize with DNA inducing a high degree of genome compaction, protecting DNA from oxidative cleavage or redox-stress, thermal shock and UV-light [65].

Macrodomain associated protein

Plectonemic domains, (described in the supercoiling chapter) can be clustered in space forming specific spatial arrangement of large DNA regions displaying higher interactions called macrodomain (MD) frequencies [18]. The *E. coli* chromosome is divided into 4 macrodomain : Ori, Ter, Left, Right and two Non Structured domains (NS). The Ter MD is centered on *dif*, a 28bp sequence involved in chromosome dimer resolution while the Ori MD encompasses oriC, the origin of replication locus. The Ori MD is flanked by the two NS regions called NS Right (NSR) and NS Left (NSL) and the Right and Left MD are adjacent to the Ter MD.

The molecular mechanisms responsible for MDs organization have been partially uncovered. The structuring of the Ter MD relies on the binding of MatP to 23 matS sequences distributed along the Ter domain [66]. Localization and segregation of MD are tightly controlled during the cell cycle: Ter MD is anchored to the division machinery through an interaction of MatP with ZapB [67], a component of the divisome, and the DNA translocase FtsK removes MatP from the Ter MD to achieve chromosome segregation [68]. In the absence of MatP, loci belonging to the Ter MD exhibit a higher level of mobility, and segregation of the Ter MD occurs earlier in the cell cycle[66,69]. In addition SlmA and SeqA proteins are unable to bind Ter MD. SlmA binds specifically DNA duplexes containing a 12-bp palindromic site with the consensus, 5'-GTGAGTACTCAC-3' named SlmA–DNA-binding sequence (SBS). SBS sites are essentially absent in the Ter MD and largely absent from the MDs that surround the Ter. SlmA is able to antagonize FtsZ assembly in higher order spiral-like structures [70]. Therefore, after replication of the Ter domain the mid-cell position is free of SlmA and, in cooperation with the Min system, FtsZ can polymerize in the Z-ring leading to proper cell splitting [71]. SeqA binds to hemi-methyleted GATC motifs that are generated upon replication and more abundant near oriC and almost absent in the Ter MD. DNA bound SeqA proteins prevents DnaA from starting a new replication initiation. From cell fractionation experiments and PALM

experiment a fraction of SeqA results localized at the membrane but the molecular mechanism through which this soluble protein can bind the membrane remains unknown [72].

The organization of the Ori MD depends on the MaoP protein and on a single sequence of 17 bp, called maoS, located close to oriC. How the maoS/MaoP system structures the DNA over several hundred of kilobases is still unknown.

The macrodomain organization influences the segregation of sister chromatids, the mobility of chromosomal DNA and the cellular localization of the chromosome[73].

Conclusion

The role of NAPs in compacting the global nucleoid is still unclear. Since NAPs have the tendency to bind AT rich region it is conceivable to consider overlapping as a key feature of the various NAPs function. In fact bacterial cells missing one of the NAPs usually have subtly different phenotypes. For example, HU and IHF single mutants are viable while HU IHF double mutants have compromised growth and survival [74].

NAPs-DNA organization is a highly dynamic structure as the genome is subject to processes that alter the DNA's mechanical properties such as transcription, replication and segregation of the genome.

Although it is not fully understood the role of NAPs in the global nucleoid structuring they have important effects on local nucleoid structure. The nucleoid is organized in topologically independent loops of about 10 kb [14]. DNA bending proteins could affect the local arrangement of the nucleoid by determining the location of the apex of supercoiled loops, thus modulating the expression of nearby genes. In contrast, bridging of the loops may prevent duplex slithering preserving the loop's gene succession.

Binding experiment with hyperplectonemes DNA bound with IHF, FIS and HNS highlights the link between the nanomechanical properties of nucleoprotein complexes and the protein regulatory function. FIS, which is a transcriptional activator, stabilized dynamic and soft DNA complexes, as opposed to H-NS, a global transcriptional repressor, which stabilized more stiffen and organized nucleoprotein complexes preventing duplex slithering [15]. In this scenario NAP could act as potential 'bacterial chromatin remodellers' able to modulate the organization of plectonemic loop [15]. NAP could also affect super helical density by recruiting RNA polymerase to the promoter in particular loci, such as rRNA operon during fast growth [75].

All processes involved in genome folding are differentially modulated in a growth phase-depended state. Different sets of NAPs are expressed according to the state of bacterial growth stage [53,76].

In early exponential phase Fis is the most abundant NAP reaching 30000 dimers/cell followed by Hu (17500 dimers/cell), HNS(13000 dimers/cell),IHF(7000 dimers/cell), DPS(2500 dodecamers/cell) and LRP(375 octamers/cell). Upon entry in late exponential Fis disappear and the most abundant NAP becames IHF (30000 dimers) followed by HU(27500 dimers) DPS(10416 dodecamers), HNS (9500 dimers) and LRP (62 octamers). In early stationary IHF decreas half of the concentration (15000 dimers) DPS became the second most aboundant nap (14580 dodecamers) , like IHF, HU and HNS decreases their concentration(7500 dimers and 3250 dimers respectively) and LRP concentration don't varied. Upon starved condition DPS became the most abundant NAP(15000 dodecamers), while all the concentration of the other NAP are begun stable.

The transition from exponential to stationary phase is accompanied also by a reduction in the number of negative supercoils of both plasmid [77] and genomic DNA[78]. In addition, a decrease of the cellular metabolism can induce a reduction of the cytoplasmic fluidity [79] which, in turn, affects macromolecular crowding and genome compaction.

Overall, the data suggest that at any given bacterial growth phase there is a high level of DNA bending proteins (antagonizing the action of DNA bridging proteins) that modulate the nucleoid structure ensuring an "open", transcriptionally active, conformation during phases of relatively fast growth. Dps becomes the most abundant protein in late stationary cells and its ability to form large collapsed nucleoprotein complexes, coupled with reprogramming of RNA polymerase, transforms the dynamic nucleoid into a static, transcriptionally inactive, structure that is protected against damage.
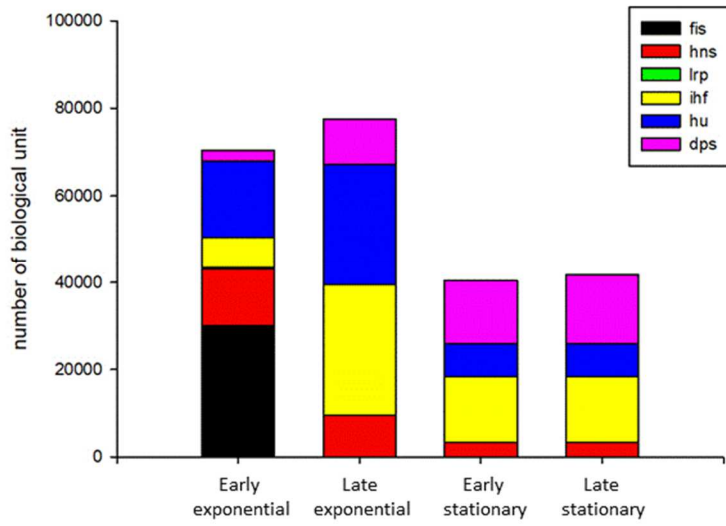
Figure 8 . Expression pattern of the major nap in different growth stage (based on the data of T. A. Azam, Iwata, Nishimura, Azam, & Ueda, 1999).

Bibliography

1. Cerritelli, M.E., Cheng, N.Q., Rosenberg, A.H., McPherson, C.E., Booy, F.P., and Steven AC. Encapsidated conformation of bacteriophage T7 DNA. *Cell*. 1997;91:271–280.

2. Becker NA, Kahn JD, Maher LJ. Effects of nucleoid proteins on DNA repression loop formation in Escherichia coli. *Nucleic Acids Res*. 2007;35(12):3988-4000. doi:10.1093/nar/gkm419.

3. Luijsterburg MS, White MF, Van Driel R, Th. Dame R. The major architects of chromatin: Architectural proteins in bacteria, archaea and eukaryotes. *Crit Rev Biochem Mol Biol*. 2008;43(6):393-418. doi:10.1080/10409230802528488.

4. Bates A.D. ; Maxwell A. *DNA Topology*.; 1999.

5. Drlica K. Control of bacterial DNA supercoiling. *Mol Microbiol*. 1992;6(4):425-433. doi:10.1111/j.1365-2958.1992.tb01486.x.

6. Holmes VF, Cozzarelli NR. Closing the ring: links between SMC proteins and chromosome partitioning, condensation, and supercoiling. *Proc Natl Acad Sci U S A*. 2000;97(4):1322-1324. doi:10.1073/pnas.040576797.

7. Sawitzke J a, Austin S. Suppression of chromosome segregation defects of Escherichia coli muk mutants by mutations in topoisomerase I. *Proc Natl Acad Sci U S A*. 2000;97(4):1671-1676. doi:10.1073/pnas.030528397.

8. Zechiedrich EL, Khodursky AB, Cozzarelli NR. Topoisomerase IV, not gyrase, decatenates products of site-specific recombination in Escherichia coli. *Genes Dev*. 1997;11(19):2580-2592. doi:10.1101/gad.11.19.2580.

9. Deng S, Stein RA, Higgins NP. Organization of supercoil domains and their reorganization by transcription. 2006;57(6):53-66.

10. N. Patrick Higgins. RNA Polymerase: Chromosome Domain Boundary Maker and Regulator of Supercoil Density. 2015;25(4):368-379. doi:10.1016/j.cogdev.2010.08.003.Personal.

11. Liu LF, Wang JC. Supercoiling of the DNA template during transcription. *Proc Natl Acad Sci U S A*. 1987;84(20):7024-7027. doi:10.1073/pnas.84.20.7024.

12. Booker BM, Deng S, Higgins NP. DNA topology of highly transcribed operons in Salmonella enterica serovar Typhimurium. *Mol Microbiol*. 2010;78(6):1348-1364. doi:10.1111/j.1365-2958.2010.07394.x.

13. Kavenoff R, Bowen BC. Electron microscopy of membrane-free folded chromosomes from Escherichia coli. *Chromosoma*. 1976;59(2):89-101. doi:10.1007/BF00328479.

14. Lisa Postow, Christine D. Hardy, Javier Arsuaga NRC. Topological domain structure of the Escherichia coli chromosome. *Genes Dev*. 2004;3(5):1766-1779. doi:10.1101/gad.1207504.Fortunately.

15. Japaridze A, Muskhelishvili G, Benedetti F, et al. Hyperplectonemes: A Higher Order Compact and Dynamic DNA Self-Organization. *Nano Lett*. 2017;17(3):1938-1948. doi:10.1021/acs.nanolett.6b05294.

16.	Shuichi Kusano QD, Nobuyuki Fujita and AI. Promoter Selectivity of Escherichia coli RNA Polymerase. 1984;259(3):1951-1957.

17.	Pelletier J, Halvorsen K, Ha B-Y, et al. Physical manipulation of the Escherichia coli chromosome reveals its soft nature. *Proc Natl Acad Sci*. 2012;109(40):E2649-E2656. doi:10.1073/pnas.1208689109.

18.	Valens M, Penaud S, Rossignol M, Cornet F, Boccard F. Macrodomain organization of the Escherichia coli chromosome. *EMBO J*. 2004;23(21):4330-4341. doi:10.1038/sj.emboj.7600434.

19.	Esposito D, Petrovic A, Harris R, et al. H-NS oligomerization domain structure reveals the mechanism for high order self-association of the intact protein. *J Mol Biol*. 2002;324(4):841-850. doi:10.1016/S0022-2836(02)01141-5.

20.	Grainger DC. Structure and function of bacterial H-NS protein. *Biochem Soc Trans*. 2016;44(6):1561-1569. doi:10.1042/BST20160190.

21.	Wang W, Li G-W, Chen C, Xie XS, Zhuang X. Chromosome Organization by a Nucleoid-Associated Protein in Live Bacteria. *Science (80-)*. 2011;333(6048):1445-1449. doi:10.1126/science.1204697.

22.	Cho B-K, Barrett CL, Knight EM, Park YS, Palsson BO. Genome-scale reconstruction of the Lrp regulatory network in Escherichia coli. *Proc Natl Acad Sci*. 2008;105(49):19462-19467. doi:10.1073/pnas.0807227105.

23.	Chen, S. & Calvo JM. Leucine-induced dissociation of Escherichia coli Lrp hexadecamers to octamers. *J Mol Biol*. 2002;318:1031–1042.

24.	Leonard PM, Smits SHJ, Sedelnikova SE, et al. Crystal structure of the Lrp-like transcriptional regulator from the archaeon Pyrococcus furiosus. *EMBO J*. 2001;20(5):990-997. doi:10.1093/emboj/20.5.990.

25.	Beloin C, Jeusset J, Révet B, Mirambeau G, Le Hégarat F, Le Cam E. Contribution of DNA conformation and topology in right-handed DNA wrapping by the Bacillus subtilis LrpC protein. *J Biol Chem*. 2003;278(7):5333-5342. doi:10.1074/jbc.M207489200.

26.	Landgraf JR, Wu J, Calvo JM. Effects of nutrition and growth rate on Lrp levels in Escherichia coli. *J Bacteriol*. 1996;178(23):6930-6936.

27.	Niki H, Jaffe A. The new gene mukB codes for a 177 kd protein with coiled-coil domains involved in chromosome partitioning of E.coli. 1991;1(1):183-193.

28.	Melby TE, Ciampaglio CN, Briscoe G, Erickson HP. The symmetrical structure of structural maintenance of chromosomes (SMC) and MukB proteins: Long, antiparallel coiled coils, folded at a flexible hinge. *J Cell Biol*. 1998;142(6):1595-1604. doi:10.1083/jcb.142.6.1595.

29.	Matoba K, Yamazoe M, Mayanagi K, Morikawa K, Hiraga S. Comparison of MukB homodimer versus MukBEF complex molecular architectures by electron microscopy reveals a higher-order multimerization. *Biochem Biophys Res Commun*. 2005;333(3):694-702. doi:10.1016/j.bbrc.2005.05.163.

24

30. Woo JS, Lim JH, Shin HC, et al. Structural Studies of a Bacterial Condensin Complex Reveal ATP-Dependent Disruption of Intersubunit Interactions. *Cell*. 2009;136(1):85-96. doi:10.1016/j.cell.2008.10.050.

31. Petrushenko ZM, Lai C-H, Rybenkov V V. Antagonistic interactions of kleisins and DNA with bacterial condensin MukB. *J Biol Chem*. 2006;281(45):34208-34217. doi:10.1074/jbc.M606723200.

32. Wang Q, Mordukhova EA, Edwards AL, Rybenkov V V. Chromosome condensation in the absence of the non-SMC subunits of MukBEF. *J Bacteriol*. 2006;188(12):4431-4441. doi:10.1128/JB.00313-06.

33. Chen N, Zinchenko AA, Yoshikawa Y, et al. ATP-induced shrinkage of DNA with MukB protein and the MukBEF complex of escherichia coli. *J Bacteriol*. 2008;190(10):3731-3737. doi:10.1128/JB.01863-07.

34. Li Y, Stewart NK, Berger AJ, et al. Escherichia coli condensin MukB stimulates topoisomerase IV activity by a direct physical interaction. *Proc Natl Acad Sci U S A*. 2010;107(44):18832-18837. doi:10.1073/pnas.1008678107.

35. Hayama R, Marians KJ. Physical and functional interaction between the condensin MukB and the decatenase topoisomerase IV in Escherichia coli. *Proc Natl Acad Sci*. 2010;107(44):18826-18831. doi:10.1073/pnas.1008140107.

36. Valentin V. Rybenkov*, Viridiana Herrera, Zoya M. Petrushenko and HZ. MukBEF, a chromosomal organizer. *J Mol Microbiol Biotechnol*. 2014;24:371–383.

37. Hayama R, Bahng S, Karasu ME, Marians KJ. The MukB-ParC interaction affects the intramolecular, not intermolecular, activities of topoisomerase IV. *J Biol Chem*. 2013;288(11):7653-7661. doi:10.1074/jbc.M112.418087.

38. Danilova O, Reyes-Lamothe R, Pinskaya M, Sherratt D, Possoz C. MukB colocalizes with the oriC region and is required for organization of the two Escherichia coli chromosome arms into separate cell halves. *Mol Microbiol*. 2007;65(6):1485-1492. doi:10.1111/j.1365-2958.2007.05881.x.

39. Rice PA, Yang SW, Mizuuchi K, Nash HA. Crystal structure of an IHF-DNA complex: A protein-induced DNA U-turn. *Cell*. 1996;87(7):1295-1306. doi:10.1016/S0092-8674(00)81824-3.

40. Swinger KK, Rice PA. IHF and HU: Flexible architects of bent DNA. *Curr Opin Struct Biol*. 2004;14(1):28-35. doi:10.1016/j.sbi.2003.12.003.

41. Ali BMJ, Amit R, Braslavsky I, Oppenheim a B, Gileadi O, Stavans J. Compaction of single DNA molecules induced by binding of integration host factor (IHF). *Proc Natl Acad Sci U S A*. 2001;98(19):10658-10663. doi:10.1073/pnas.181029198.

42. Santero E, Hoover TR, North AK, Berger DK, Porter SC, Kustu S. Role of integration host factor in stimulating transcription from the σ54-dependent nifH promoter. *J Mol Biol*. 1992;227(3):602-620. doi:https://doi.org/10.1016/0022-2836(92)90211-2.

43. Sheridan SD, Benham CJ, Hatfield W, Hatfield GW. Inhibition of DNA Supercoiling-dependent Transcriptional Activation by a Distant B-DNA to Z-DNA Transition Inhibition of DNA Supercoiling-dependent Transcriptional Activation by a Distant B-DNA. 1999;274(12):8169-8174.

44. Engelhorn M, Boccard F, Murtin C, Prentki P, Geiselmann J. In vivo interaction of the Escherichia coli integration host factor with its specific binding sites. *Nucleic Acids Res*. 1995;23(17):2959-2965. doi:10.1093/NAR/23.15.2959.

45. Yang SW, Nash H a. Comparison of protein binding to DNA in vivo and in vitro: defining an effective intracellular target. *EMBO J*. 1995;14(24):6292-6300. doi:10.1016/0092-8674(89)90801-5.

46. Stella S, Cascio D, Johnson RC. The shape of the DNA minor groove directs binding by the DNA-bending protein Fis. *Genes Dev*. 2010;24(8):814-826. doi:10.1101/gad.1900610.

47. Johnson RC, Johnson LM, Schmidt JW, Gardner JF. Major Nucleoid Proteins in the Structure and Function of the Escherichia coli Chromosome. In: *The Bacterial Chromosome*. American Society of Microbiology; 2005:65-132. http://www.asmscience.org/content/book/10.1128/9781555817640.chap5.

48. Pan CQ, Finkel SE, Cramton SE, Feng J a, Sigman DS, Johnson RC. Variable structures of Fis-DNA complexes determined by flanking DNA-protein contacts. *J Mol Biol*. 1996;264:675-695. doi:10.1006/jmbi.1996.0669.

49. Dame RT. The role of nucleoid-associated proteins in the organization and compaction of bacterial chromatin. *Mol Microbiol*. 2005;56(4):858-870. doi:10.1111/j.1365-2958.2005.04598.x.

50. Dame RT, Dorman CJ. Bacterial chromatin. *Bact Chromatin*. 2010:1-448. doi:10.1007/978-90-481-3473-1.

51. Dame RT, van Mameren J, Luijsterburg MS, et al. Analysis of scanning force microscopy images of protein-induced DNA bending using simulations. *Nucleic Acids Res*. 2005;33(7):1-7. doi:10.1093/nar/gni073.

52. Rochman M, Blot N, Dyachenko M, Glaser G, Travers A, Muskhelishvili G. Buffering of stable RNA promoter activity against DNA relaxation requires a far upstream sequence. *Mol Microbiol*. 2004;53(1):143-152. doi:10.1111/j.1365-2958.2004.04126.x.

53. Azam TA, Iwata A, Nishimura A, Azam T a LI, Ueda S. Growth Phase-Dependent Variation in Protein Composition of the Escherichia coli Nucleoid Growth Phase-Dependent Variation in Protein Composition of the Escherichia coli Nucleoid. *J Bac*. 1999;181(20):6361. doi:<p></p>.

54. Claret L, Rouviere-Yaniv J. Variation in HU composition during growth of Escherichia coli: the heterodimer is required for long term survival. *J Mol Biol*. 1997;273(1):93-104. doi:10.1006/jmbi.1997.1310.

55. Swinger KK, Lemberg KM, Zhang Y, Rice PA. Flexible DNA bending in HU-DNA cocrystal structures. *EMBO J*. 2003;22(14):3749-3760. doi:10.1093/emboj/cdg351.

56. Guo F, Adhya S. Spiral structure of Escherichia coli HU provides foundation for DNA supercoiling. *Proc Natl Acad Sci*. 2007;104(11):4309-4314. doi:10.1073/pnas.0611686104.

57. Pontiggia A, Negri A, Beltrame M, Bianchi ME. Protein HU binds specifically to kinked DNA. *Mol Microbiol*. 1993;7(3):343-350. doi:10.1111/j.1365-2958.1993.tb01126.x.

58.   Bonnefoy E, Takahashi M, Yaniv JR. DNA-binding Parameters of the HU Protein of Escherichia coli to Cruciform DNA. *J Mol Biol*. 1994;242(2):116-129. doi:https://doi.org/10.1006/jmbi.1994.1563.

59.   Qian Z, Macvanin M, Dimitriadis EK, He X, Zhurkin V, Adhya S. A new noncoding RNA arranges bacterial chromosome organization. *MBio*. 2015;6(4):1-8. doi:10.1128/mBio.00998-15.

60.   Azam T, Ishihama A. Twelve species of the nucleoid-associated protein 481 from Escherichia coli. *Seq Recognit Specif DNA Bind …*. 1999;274(46):33105-33113. doi:10.1074/jbc.274.46.33105.

61.   Grant RA, Filman DJ, Finkel SE, Kolter R HJ. The crystal structure of DPS, a ferritin homolog that binds and protect DNA. *Nat Struct Biol*. 1998;(5):400-406. doi:10.1038/nsb0698-432.

62.   Ceci P, Cellai S, Falvo E, Rivetti C, Rossi GL, Chiancone E. DNA condensation and self-aggregation of Escherichia coli Dps are coupled phenomena related to the properties of the N-terminus. *Nucleic Acids Res*. 2004;32(19):5935-5944. doi:10.1093/nar/gkh915.

63.   Ceci P, Mangiarotti L, Rivetti C, Chiancone E. The neutrophil-activating Dps protein of Helicobacter pylori, HP-NAP, adopts a mechanism different from Escherichia coli Dps to bind and condense DNA. *Nucleic Acids Res*. 2007;35(7):2247-2256. doi:10.1093/nar/gkm077.

64.   Chodavarapu S, Gomez R, Vicente M, Kaguni JM. Escherichia coli Dps interacts with DnaA protein to impede initiation: A model of adaptive mutation. *Mol Microbiol*. 2008;67(6):1331-1346. doi:10.1111/j.1365-2958.2008.06127.x.

65.   Frenkiel-Krispin D, Ben-Avraham I, Englander J, Shimoni E, Wolf SG, Minsky A. Nucleoid restructuring in stationary-state bacteria. *Mol Microbiol*. 2004;51(2):395-405. doi:10.1046/j.1365-2958.2003.03855.x.

66.   Mercier R, Petit MA, Schbath S, et al. The MatP/matS Site-Specific System Organizes the Terminus Region of the E. coli Chromosome into a Macrodomain. *Cell*. 2008;135(3):475-485. doi:10.1016/j.cell.2008.08.031.

67.   Espéli O, Borne R, Dupaigne P, et al. A MatP-divisome interaction coordinates chromosome segregation with cell division in *E. coli*. *EMBO J*. 2012;31(14):3198-3211. doi:10.1038/emboj.2012.128.

68.   Stouf M, Meile J-C, Cornet F. FtsK actively segregates sister chromosomes in Escherichia coli. *Proc Natl Acad Sci*. 2013;110(27):11157-11162. doi:10.1073/pnas.1304080110.

69.   Dupaigne P, Tonthat NK, Esp??li O, Whitfill T, Boccard F, Schumacher MA. Molecular Basis for a Protein-Mediated DNA-Bridging Mechanism that Functions in Condensation of the E. coli Chromosome. *Mol Cell*. 2012;48(4):560-571. doi:10.1016/j.molcel.2012.09.009.

70.   Du S, Lutkenhaus J. SlmA Antagonism of FtsZ Assembly Employs a Two-pronged Mechanism like MinCD. *PLoS Genet*. 2014;10(7). doi:10.1371/journal.pgen.1004460.

71.   Tonthat NK, Arold ST, Pickering BF, et al. Molecular mechanism by which the nucleoid occlusion factor , SlmA , keeps cytokinesis in check. *EMBO J*. 2010;30(1):154-164. doi:10.1038/emboj.2010.288.

72.   Mika JT, Vanhecke A, Dedecker P, et al. A study of SeqA subcellular localization in *Escherichia coli*

using photo-activated localization microscopy. *Faraday Discuss*. 2015;184:425-450. doi:10.1039/C5FD00058K.

73.   Espeli O, Mercier R. DNA dynamics vary according to macrodomain topography in the E . coli chromosome. 2008;68(April):1418-1427. doi:10.1111/j.1365-2958.2008.06239.x.

74.   Kano Y, Imamoto F. Requirement of integration host factor (IHF) for growth of Escherichia coli deficient in HU protein. *Gene*. 1990;89(1):133-137. doi:https://doi.org/10.1016/0378-1119(90)90216-E.

75.   Jun Jin D, Cagliero C, Zhou YN. Role of RNA Polymerase in the Organization of the Bacterial Nucleoid. *Chem Rev*. 2014;113(11). doi:10.1021/cr4001429.Role.

76.   Talukder AA, Hossain MA, Yamada M, Ishihama A. Nucleoids Dynamic in Escherichia coli : A Growth Phase Dependent Process. *bangladesh j Microb*. 2006;23(2):81-88.

77.   Balke VL, Gralla JD. Changes in the linking number of supercoiled DNA accompany growth transitions in Escherichia coli. *J Bacteriol*. 1987;169(10):4499-4506. doi:10.1128/jb.169.10.4499-4506.1987.

78.   Lal A, Dhar A, Trostel A, Kouzine F, Seshasayee ASN, Adhya S. Genome scale patterns of supercoiling in a bacterial chromosome. *Nat Commun*. 2016;7(April):1-8. doi:10.1038/ncomms11055.

79.   Parry BR, Surovtsev I V., Cabeen MT, O'Hern CS, Eric Dufresne R, Jacobs-Wagner C. The bacterial cytoplasm has glass-like properties and is fluidized by metabolic activity. 2009;42(1):115-125. doi:10.1086/498510.Parasitic.

Metal-responsive promoter DNA compaction by the ferric uptake regulator

Davide Roncarati[1,*], Simone Pelliciari[1,*], Nicola Doniselli[2,*], Stefano Maggi[2], Andrea Vannini[1], Luca Valzania[1], Luca Mazzei[1], Barbara Zambelli[1], Claudio Rivetti[2] & Alberto Danielli[1]

Short-range DNA looping has been proposed to affect promoter activity in many bacterial species and operator configurations, but only few examples have been experimentally investigated in molecular detail. Here we present evidence for a metal-responsive DNA condensation mechanism controlled by the *Helicobacter pylori* ferric uptake regulator (Fur), an orthologue of the widespread Fur family of prokaryotic metal-dependent regulators. *H. pylori* Fur represses the transcription of the essential *arsRS* acid acclimation operon through iron-responsive oligomerization and DNA compaction, encasing the *arsR* transcriptional start site in a repressive macromolecular complex. A second metal-dependent regulator NikR functions as nickel-dependent anti-repressor at this promoter, antagonizing the binding of Fur to the operator elements responsible for the DNA condensation. The results allow unifying *H. pylori* metal ion homeostasis and acid acclimation in a mechanistically coherent model, and demonstrate, for the first time, the existence of a selective metal-responsive DNA compaction mechanism controlling bacterial transcriptional regulation.

[1] Department of Pharmacy and Biotechnology (FaBiT), University of Bologna, 40126 Bologna, Italy. [2] Department of Life Sciences, University of Parma, 43124 Parma, Italy. * These authors contributed equally to this work. Correspondence and requests for materials should be addressed to C.R. (email: claudio.rivetti@unipr.it) or to A.D. (email: alberto.danielli@unibo.it).

29

D NA condensation and looping are fundamental mechanisms for genome biology and gene regulation in prokaryotes and eukaryotes. In bacteria, long-range DNA compaction and gene expression impact on the topological organization of the nucleoid[1], while local DNA bending by transcription factors and nucleoid-associated proteins (NAPs) has provided early paradigmatic evidence for the importance of DNA looping in the regulation of promoter elements[2,3].

Accordingly, short-range DNA looping has been proposed to account for particular operator configurations and promoter responses in countless reports and many bacterial species. Nevertheless, only few examples have been experimentally investigated in molecular detail, principally, but not exclusively, involving phage repressors[4], and the sugar, nitrogen or nucleotide catabolism regulation in *Escherichia coli*[5–8]. The capability to constrain and to locally distort the DNA is also a key feature of NAPs and global regulators involved in transcriptional control[9]. Remarkably, the involvement of transcription factor-mediated DNA looping in the transduction of metal-dependent transcriptional responses has not been reported to date, although several metal ions and metal-sensing regulators (such as Fe^{2+}-Fur and Ni^{2+}-NikR) have fundamental roles in bacterial viability, virulence and host–pathogen interactions[10]. A unique exception pertains to the recent prediction of a putative Fur-dependent DNA looping at the *fepB-entCEBAH* promoter, inferred from theoretical binding site annotations of *E. coli* promoters[6]. Fur proteins belong to an ubiquitously conserved superfamily of prokaryotic regulators involved in the homeostasis of different metal ions and oxidative stress responses[11]. Because of their ability to oligomerize in a metal-dependent fashion[12,13] and to bind promoters at multiple sites[14–16], they represent ideal candidates for the investigation of metal-dependent DNAe. In addition, topological modifications of the DNA induced by Fur binding, such as bending and wrapping, have been reported *in vitro* using various footprinting and microscopy techniques, including atomic force microscopy (AFM)[17,18].

Herein, we use the thoroughly characterized *H. pylori* Fur regulator as a model to explore the metal-dependent short-scale DNA compaction mechanisms involved in transcriptional regulation. To this aim, we investigate the Fur-regulated *arsR* promoter by a combination of DNase I footprinting, AFM and promoter functional analysis. The rationale behind the choice of this promoter derives from the ChIP-chip and functional evidence that Fur regulates and targets the *arsRS* operon *in vivo*[19,20]. This operon encodes a two-component system that controls transcription of many *H. pylori* pH-dependent genes through the activity of the auto-regulated ArsR response regulator[21]. ArsR is crucial for the positive regulation of the nickel-dependent urease metallo-enzyme, which is important for acid acclimation[22]. This transcriptional regulator also appears to positively regulate other essential pH-independent functions of *H. pylori* because, unlike the *arsS* histidine kinase gene, *arsR* deletion mutants have not been attainable to date. Interestingly, the acid tolerance of *H. pylori* was shown to be impaired in both *fur* and *nikR* (nickel-dependent regulator) deletion mutants[23,24], fostering the hypothesis of a shallow regulatory circuit linking metal-ion homeostasis with acid acclimation[25].

In this work, we characterize the role of these metal-dependent regulators in the transcriptional control of the essential *arsR* operon. We demonstrate the direct wiring of Fur and NikR with the ArsR regulon, and highlight the contribution of DNA compaction to this process. In particular, we show that the *arsR* promoter sports a complex operator architecture with multiple Fur and NikR operators, bound with different affinities according to the metallation state of the regulators. Evidence is presented that this promoter architecture allows for iron- and

Fur-dependent repression (FeOFF) through the compaction of the promoter in a nucleo–protein complex. In the presence of nickel ions, binding of NikR antagonizes Fur binding and DNA compaction thus relieving Fur repression (NikRON). The fundamental implications of this metal-responsive promoter compaction mechanism are discussed, together with its pivotal role in the *H. pylori* transcriptional regulatory circuit.

Results

ArsR transcription is controlled by Fur and NikR metallo-regulators. To investigate how metal homeostasis regulation could transcriptionally feed into the ArsR regulon, we performed primer extension analyses of the native P*arsR* promoter using total RNA extracted from exponential phase *H. pylori* cultures and we compared the responses elicited by treatment with different metal ions (Fe^{2+} and Ni^{2+}) or iron chelator (Dipy), under different genetic backgrounds (Fig. 1).

In a wild-type background, P*arsR* transcription was repressed by either iron or nickel, while iron chelation caused de-repression of the promoter, pointing to a prominent role of Fur in *arsR* regulation. Accordingly, P*arsR* was constitutively de-repressed in a *fur* knockout strain, suggesting a prototypical holo-Fur repression in which the iron ion acts as co-repressor (FeOFF). While the slight repression observed after nickel treatment could indicate a repressive role of NikR on P*arsR*, we observed a
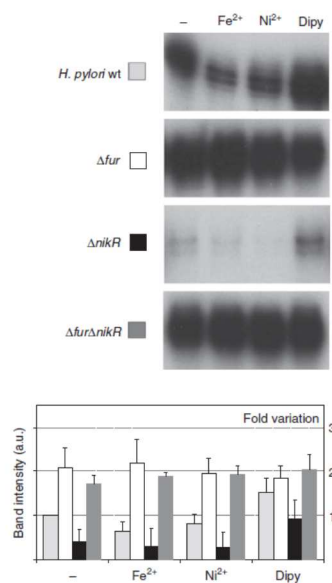

Figure 1 | Transcriptional analysis of the *arsR* gene in response to metal ion treatment. Primer extensions performed on total RNA extracted from wild-type, Δ*fur*, Δ*nikR* and Δ*fur*Δ*nikR* double mutants *H. pylori* strains grown to exponential phase and treated for 15 min with 1 mM $(NH_4)_2Fe(SO_4)_2$ (Fe^{2+}), 1 mM $NiSO_4$ (Ni^{2+}) or 100 μM 2-2 dipyridyl (Dipy); untreated control RNA (−). Full gel is shown in Supplementary Fig. 6. Fold variation of the band intensities is reported in the graph. Error bars represent the standard deviation recorded in four independent experiments.

30

generalized decrease of *arsR* transcript levels in the $\Delta nikR$ strain, in which the responses to metal-ions and chelators were maintained. At a first glance, this could be interpreted as a NikR-dependent transcriptional activation of P*arsR*; however, while the responses in wild-type and *fur*-deletion mutants proved highly reproducible, the $\Delta nikR$-dependent deregulation of P*arsR* was more variable. In a $\Delta fur\Delta nikR$ double mutant background, the *ars* promoter remained constitutively de-repressed, excluding the requirement of NikR for full promoter activation, and suggesting that the observed nickel-induced repression is directly or indirectly mediated by Fur, which would be responsible for the transduction of the Ni^{2+} signal. The documented ability of Ni^{2+} to substitute Fe^{2+} as Fur cofactor in footprinting experiments[14] supports this interpretation.

These results demonstrate that the essential ArsR acid response regulator is under the transcriptional control of the metal ion circuit regulated by Fur and NikR, with the former acting as metal-responsive master repressor (FeOFF) and the latter as positive modulator of *arsR* transcription.

Complex architecture of the *arsR* promoter. To elucidate the molecular mechanisms responsible for the regulation of *arsR*, the protein–DNA interactions of recombinant Fur and NikR at the P*arsR* promoter were investigated by DNase I footprinting (Fig. 2).

Fur exhibited a complex pattern of iron-sensitive (apo-) and iron-dependent (holo-) operators: when iron was chelated from the reaction, the resulting apo-Fur protein protected two distinct elements (Fig. 2a; left gel): (i) a distal high affinity apo-operator (fOPII; full protection at 30 nM apo-Fur) located from -114 to -154 bp upstream of the transcriptional start site (TSS) and (ii) a central operator (fOPI) extending from -49 to -82 bp upstream of the TSS (protection at 75 nM apo-Fur). When Fur was pre-incubated with iron the affinities for these operators changed (Fig. 2a; right gel). In particular, while the affinity for the distal apo-operator decreased, the affinity for the central operator increased 5-fold (protection at 12 nM holo-Fur). In addition, a third low-affinity element (fOPIII) appeared beneath and immediately downstream of the TSS (protection at 125 nM holo-Fur). To better define the interactions of Fur within the promoter region, apo- and holo-Fur DNA footprinting was performed with a P*arsR* probe labelled on the noncoding (antiparallel) strand (Fig. 2b). The observed protection patterns matched closely those observed on the coding strand, mapping the principal holo-Fur protection from $+5$ to $+40$ bp downstream of the *arsR* TSS, with a weaker but reproducible upstream extension of the footprint into the core promoter. This low affinity holo-Fur element overlaps the core promoter and the ArsR operator[26] required for auto-repression by ArsR.

Notably, distinct hypersensitive and/or persistent bands appeared upon Fur binding under different metallation states (see arrowheads in Fig. 2). When iron was chelated two persistent bands, encompassed between the central (fOPI) and the distal apo-Fur operators (fOPII), appeared. Upon binding of holo-Fur, these persistent bands repositioned more closely, while a strong hypersensitive band became visible between the central (fOPI) operator and the downstream low affinity holo-Fur operator (fOPIII), indicating bending of the DNA in this region upon Fur binding. In addition, another two bands distal to fOPII appeared stronger with increasing amounts of Fur, which may be imputable to an overrepresentation of longer DNA fragments due to inhibition of DNAse I by higher conentrations of Fur. These results suggest the existence of different DNA topologies determined by the binding of apo- or holo-Fur to P*arsR*.

The pattern of NikR interactions with the P*arsR* probe proved more straightforward. In the absence of Ni^{2+} ions (Fig. 2c; left

gel), apo-NikR was unable to bind DNA, in accordance with previous reports[27]. When NikR was preincubated with nickel (Fig. 2c; right gel), two regions of DNase I protection appeared at approximately similar NikR concentrations (protection at 40–60 nM holo-NikR). The distal element (nOPII) (from -115 to -154) perfectly overlapped the distal apo-Fur operator, while the proximal NikR element (nOPI; from -14 to -50) mapped adjacent and downstream of the central Fur operator. In contrast to Fur, binding of NikR to the P*arsR* probe did not elicit DNase I hypersensitive bands.

Overall, the regions protected by holo-Fur, apo-Fur and NikR match well to the previously identified consensus sequences[12,28] (Fig. 2d) and reveal a complex architecture of the *arsR* promoter region, which can be schematized as shown in Fig. 2e. It will be noted that Fur and NikR operators are counterintuitively positioned on the *ars* promoter with regard to their regulatory function. In particular, the Fur-iron repression of P*arsR* observed in primer extension experiments, would suggest at least one high affinity holo-Fur operator overlapping the core promoter. Actually, the high affinity Fur operators (fOPI and fOPII) map further upstream, in positions usually occupied by class I activators, whereas only a low affinity element (fOPIII) is found in a position compatible with promoter occlusion and transcriptional repression. A similar discrepancy applies for NikR, as the nOPI operator maps immediately upstream of the -10 box, in a position frequently occupied by transcriptional repressors, albeit NikR acts as a positive regulator of P*arsR*.

Distinct macromolecular assemblies upon Fur and NikR binding to P*arsR*. The positions of persistent and hypersensitive bands observed upon binding of Fur to DNA, indicate that the metal-dependent transcriptional responses of *arsR* could derive from different macromolecular conformations of the *arsR* promoter region, shaped by Fur or NikR binding. To ascertain this hypothesis, AFM experiments were carried out to capture the structural details conferred by the binding of these regulators to the P*arsR* promoter region.

First, we analysed the oligomerization state of apo- and holo-Fur in the absence of DNA. To this end, we constructed a volume calibration curve using proteins of known molecular weight (Supplementary Fig. 1). Deposition of both apo- and holo-Fur onto freshly cleaved mica, followed by AFM imaging, resulted in a similar distribution of monomers and dimers (Supplementary Fig. 2A,B). This result was unexpected because previous reports indicated that apo-Fur is mainly a dimer while holo-Fur is prevalently represented by tetramers or higher order oligomers[12]. Because the high surface charge of mica can readily disrupt the protein quaternary structure, we used glutaraldehyde crosslinking to fix the Fur oligomeric states. Under these conditions, apo-Fur mostly comprised monomers and dimers even though the dimeric state is more populated than the monomeric one and a discrete number of particles have an inferred mass of tetramers (Supplementary Fig. 2C). Conversely, the oligomers formed by holo-Fur comprise dimers, tetramers, octamers and even higher oligomeric states (Supplementary Fig. 2D). This analysis confirms previous observations of the iron effect on the stoichiometry of Fur, and validate the application of AFM for the characterization of these complex macromolecular assemblies.

Next we analysed the DNA-binding properties of apo- and holo-Fur to a 818 bp fragment harbouring the P*arsR* promoter region (Fig. 3a). From the binding of apo-Fur to P*arsR*, we observed two different categories of complexes: one characterized by a small globular feature with an average volume of 123 ± 33 nm^3 (Fig. 3b) and the other characterized by a larger
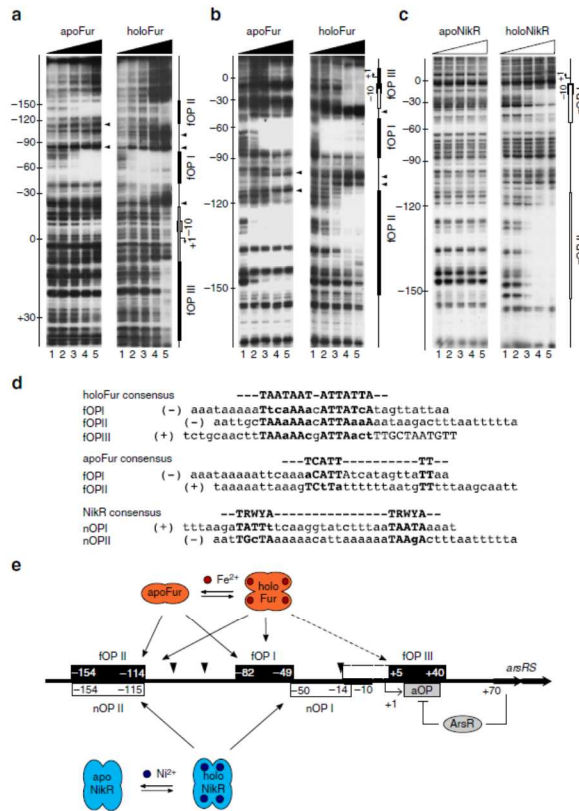
31

Figure 2 | DNA footprinting of apo/holo-Fur and apo/holo-NikR at ParsR. (a) apo-Fur (left gel) and holo-Fur (right gel) on the coding strand; (b) apo-Fur (left gel) and holo-Fur (right gel) on noncoding strand; (c) apo-NikR (left gel) and holo-NikR (right gel) on noncoding strand. Lanes 1–5: 0, 35, 70, 140 and 280 nM monomeric Fur or NikR, respectively. The scale bar on the left of each gel shows the distance from the TSS. A schematic representation of the promoter is presented on the right side of each gel with Fur and NikR footprints outlined as black and white boxes, respectively. Black arrowheads indicate persistent or hypersensitive bands. (d) Comparison of the Fur and NikR operator sequences on ParsR with the previously defined consensus motifs of the regulators. (e) Inferred schematic representation of the operator layout in the ParsR promoter. Fur operators named fOPI, fOPII and fOPIII are depicted as black boxes, while NikR operators named nOPI and nOPII are depicted as white boxes. The position of the ArsR operator aOP is mapped as reported in ref. 26. Positions are indicated with respect to the TSS.

globular feature with an average volume of $270 \pm 56 \, nm^3$ (Fig. 3c). By means of the calibration curve, we could infer that the former complexes correspond to a particle with a MW of $56 \pm 21 \, kDa$, which fits well the molecular mass of a Fur dimer (35 kDa) bound to 34 bp of DNA (22 kDa) (Table 1). Analysis of the DNA contour length of these complexes further indicates that Fur dimers are bound closely to the centre of the DNA template, in a position corresponding to the fOPI site. Furthermore, the DNA contour length is not altered by the binding of Fur (Table 1), thus suggesting the absence of a large protein-induced DNA deformation[29]. The second category of apo-Fur–DNA complexes is characterized by globular features with a larger volume and a higher image profile, bound to the DNA template slightly off centre. The inferred mass of these complexes is $113 \pm 30 \, kDa$ (Table 1), in line with a nucleoprotein complex of two apo-Fur dimers (70 kDa) bound to about 100 bp of DNA, comprising fOPI and either fOPII or fOPIII. However, on the basis of the footprinting results, binding of apo-Fur to fOPIII can be disregarded. In some images, this particular arrangement is supported by the observation of a double peak in the image profile (Fig. 3c; panels 2 and 4). Interestingly, the DNA contour length analysis of these complexes reveals a decrease of $17.4 \pm 2.5 \, nm$ suggesting that most, if not all, the bound DNA is compacted within the nucleo–protein complex.

AFM analysis of the holo-Fur interaction with the ParsR operator sites revealed remarkably different type of complexes,
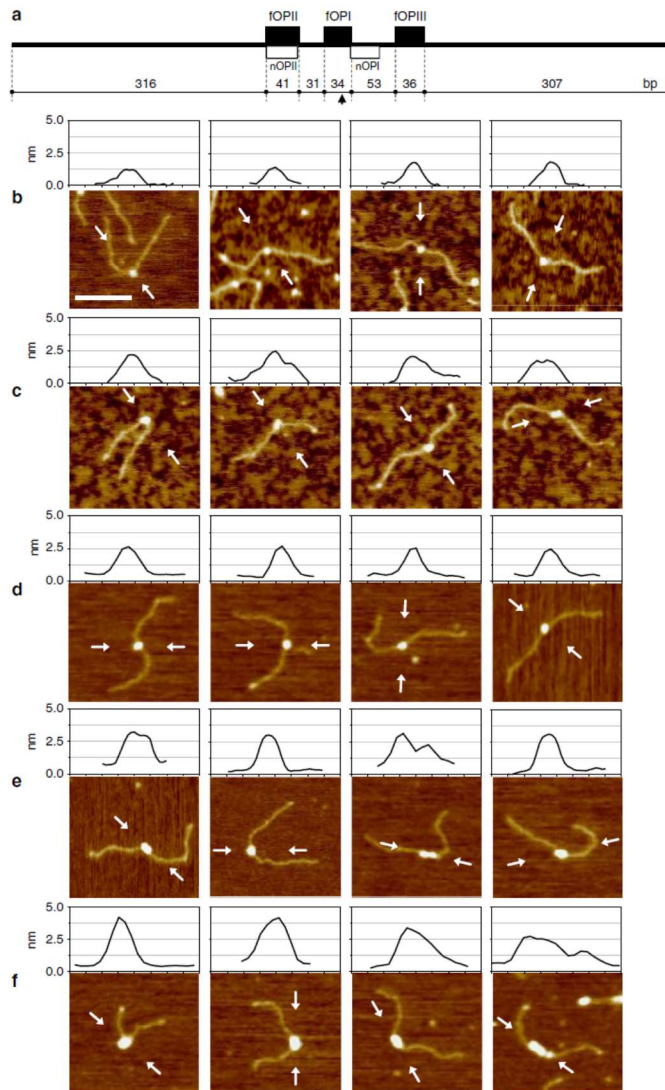
Figure 3 | AFM images of Fur–DNA complexes. (a) Scaled representation of the 818 bp DNA template used in the AFM experiments. Fur operator sites (black boxes) and NikR operator sites (white boxes) are indicated. Distances are in base pairs and the arrow indicates the midpoint of the template. **(b)** One apo-Fur dimer bound to the central fOPI site. **(c)** Two apo-Fur dimers bound to fOPI and fOPII sites. **(d)** One holo-Fur tetramer bound to the central fOPI site. **(e)** Two holo-Fur tetramers bound to fOPI and fOPII sites. **(f)** Three or more tetramers bound to fOPI, fOPII and fOPIII sites with consequent large DNA compaction. The image profile along the direction indicated by white arrows is shown on top of each panel. Scale bar, 100 nm. The profile plots have a width of 80 nm.

33

Table 1 | AFM measurements of Fur and NikR nucleoprotein complexes with P*arsR*.

	Volume (nm^3)	Inferred MW (kDa)	DNA compaction (nm)	Oligomerization state
Apo-Fur	123 ± 33	56 ± 21	0.0 ± 2.0	One dimer
Apo-Fur	270 ± 56	113 ± 30	17.4 ± 2.5	Two dimers
Holo-Fur	220 ± 39	93 ± 24	7.4 ± 3.0	One tetramer
Holo-Fur	568 ± 136	228 ± 61	14.9 ± 1.8	Two tetramers
Holo-Fur	1089 ± 244	430 ± 103	65.4 ± 10.8	Three or more tetramers
Holo-NikR-nOPI	257 ± 36	102 ± 14	11.8 ± 1.3	One tetramer
Holo-NikR-nOPII	243 ± 37	96 ± 12	10.8 ± 1.1	One tetramer

which were subdivided into three categories with features summarized in Table 1. The first category (Fig. 3d) comprises complexes with a volume of $220 \pm 39\,nm^3$ and an inferred molecular mass of $93 \pm 24\,kDa$, which well fits the molecular mass of one holo-Fur tetramer (70 kDa) bound to 34 bp of DNA (22 kDa). As before, the position of the complex indicates binding to the fOPI site. Notice that, in contrast to the two apo-Fur dimers shown in Fig. 3c, the image profiles reveal complexes formed by a compact globular feature with a single (slightly higher) peak. DNA contour length measurements indicate that binding of the tetramer to fOPI results in a DNA compaction of $7.4 \pm 3\,nm$ ($23 \pm 9\,bp$). This small DNA compaction can arise from the different path that the DNA can take upon deposition (see legend to Supplementary Fig. 2).

The second type of complexes formed by holo-Fur at the P*arsR* promoter is characterized by globular features with a volume of $568 \pm 136\,nm^3$ that corresponds to a molecular mass of $228 \pm 61\,kDa$. These complexes are most likely formed by two holo-Fur tetramers (140 kDa) bound to fOPI and fOPII and thus including more than 100 bp of DNA, which in terms of mass can account for additional 70–80 kDa. The DNA contour length analysis reveals a decrease of $14.9 \pm 1.8\,nm$ suggesting, as in the case of the two apo-Fur dimers, that contact between the two tetramers determines a significant DNA compaction, an observation supported by the dumb-bell shape of the complexes captured in a few cases (Fig. 3e).

Finally, the third category of complexes is represented by very large globular features bound near the centre of the DNA template, which appears visibly shortened (Fig. 3f). These complexes have an average volume of $1,089 \pm 244\,nm^3$ and an inferred mass of $430 \pm 103\,kDa$. The DNA contour length compaction is of $65.4 \pm 10.8\,nm$, corresponding to $204 \pm 34\,bp$ of DNA in agreement with the 195 bp DNA region spanned by the three operators fOPI, fOPII and fOPIII. Therefore, we propose that these complexes are formed by three holo-Fur tetramers each bound to one of the three operator sites. Given the tendency of holo-Fur to oligomerize, protein–protein interaction between the tetramers condenses the P*arsR* promoter region into a large nucleo–protein complex. In few cases, the particular deposition of the complex makes it possible to distinguish three individual tetramers bound to this promoter region (Fig. 3f; last panel).

The AFM experiments described above have been performed using complexes crosslinked with glutaraldehyde to prevent oligomers dissociation upon deposition onto mica. To verify that this treatment does not lead to artifactual results, we imaged the 818 bp bare DNA fragment incubated with 10 mM glutaraldehyde either for 2 or 10 min (Supplementary Fig. 3A,B). Under these conditions, we did not observe significant changes of the DNA shape, indicating that crosslinking does not affect the overall structure of the DNA. Furthermore, to assess that the higher order Fur oligomerization observed in the presence of iron is due to the peculiar architecture of the P*arsR* promoter, we constructed a mutated variant by inserting a 315 bp spacer

between the fOPI and fOPII sites to drastically change their distance. This mutant was designed also with the aim to visualize a possible DNA loop that would be formed by the interaction of Fur bound to the distant operator sites. Under these conditions, we observed complexes prevalently bound to fOPI, with an image profile height and volume consistent with a holo-Fur tetramer. Neither DNA looping nor higher order oligomers were observed (Supplementary Fig. 3C,D). These results demonstrate that the oligomeric states of holo-Fur bound to the P*arsR* promoter and the consequent DNA compaction are determined by the unique architecture of this promoter and not by artifacts introduced with the crosslinking procedure.

The AFM analysis was then applied to investigate binding of NikR to the P*arsR* promoter. Because apo-NikR does not bind DNA (Fig. 2c), the analysis was carried out only at saturating Ni^{2+} concentrations (1 mM). Under these conditions, holo-NikR forms stable tetramers that do not oligomerize in particles of high molecular mass[27]. For complexes assembly, we used the 818 bp-long DNA fragment described above as it harbours also two NikR operator sites (nOPI and nOPII) separated by 65 bp (103 bp, centre-to-centre; Fig. 2d). AFM images of NikR–DNA complexes showed that holo-NikR binds frequently near the centre of the DNA template, either on nOPI or nOPII (Fig. 4a,b, respectively), and in a few cases we could observe two NikR bound to the same DNA molecule (Fig. 4c). The distribution in Fig. 4d shows that among a total of 249 complexes, 98 were bound to nOPI and 151 to nOPII, in agreement with the slightly higher binding affinity of NikR for nOPII observed in footprinting experiments. Volume analysis of the complexes confirms that NikR binds each operator site as a tetramer (see Table 1). In addition, under our imaging conditions, we did not observe DNA looping nor large DNA compaction as it would be expected by the interaction between two NikR tetramers bound to nOPI and nOPII. This result is consistent with the absence of hypersensitive bands in NikR DNaseI footprinting.

Role of the Fur and NikR operators in *arsR* regulation. To characterize the functional significance of this complex promoter architecture, a bioluminescent *H. pylori lux* reporter strain was used[30]. Wild-type and mutagenized constructs of the P*arsR* promoter were fused upstream of a chromosomal *luxCDABE* reporter cassette and assayed for reporter expression (luminescence) and transcription (quantitative PCR with reverse transcription (RT–qPCR)) shortly after metal repletion or chelation. Concomitantly, Fur and NikR binding to each of these constructs was assayed by DNase footprinting (Supplementary Fig. 4).

The luminescence measured from the wild-type P*arsR* promoter fused to the *lux* reporter recall the responses observed in primer extension analysis at the endogenous *ars* promoter (Fig. 1 and Fig. 5a). These responses were independently substantiated also at the transcriptional level by RT–qPCR, indicating that the reporter construct could be reliably used to further dissect the complex operator architecture of P*arsR*.
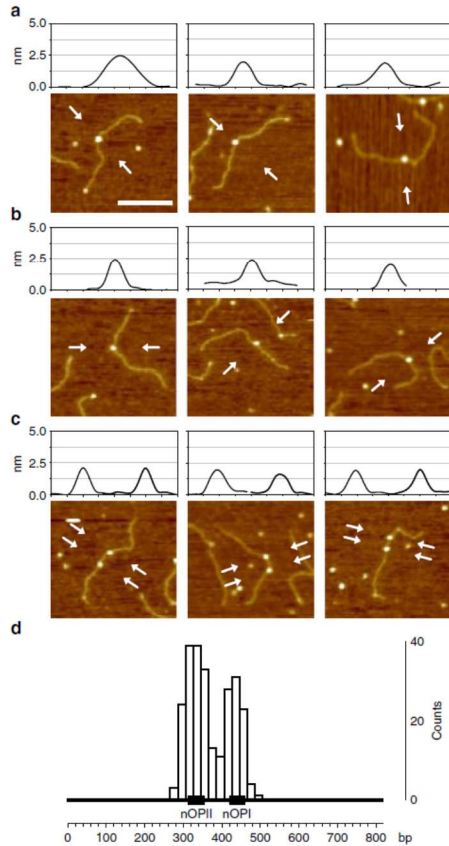
34

Figure 4 | AFM images of holo-NikR–DNA complexes. The image profile along the direction indicated by white arrows is shown on top of each panel. (**a**) One holo-NikR tetramer bound to the central nOPI site. (**b**) One holo-NikR tetramer bound to the slightly off-centre nOPII site. (**c**) Two holo-NikR tetramers bound to both nOPI and nOPII sites. (**d**) Bar chart representing the position of NikR bound along the DNA template (black line) with the nOPI and nOPII sites represented, in scale, as black boxes. Graph scale in base pairs. Scale bar, 100 nm. Width of the profile plot, 80 nm.

When the central high affinity holo-Fur operator was deleted, we observed a consistent general de-repression of the promoter with respect to the wild-type construct. Since the fusion still responded to the presence of metals, the de-repression proved to be not constitutive as in the *Δfur* strain (Fig. 5b). In fact, the promoter was consistently repressible by iron and nickel ions with fold-repression levels similar to the wild-type construct, likely due to uncompromised binding of holo-Fur to either fOPII and/or fOPIII (Supplementary Fig. 4B). On the contrary, transcription of the reporter was also inhibited after iron withdrawal, indicating a lack of inducibility.

This effect can be explained if the metal-dependent multi-merization of Fur is taken into account. In native conditions, with some iron present, Fur will be in dimeric and partly also in tetrameric state (dimer of dimers). Some Fur tetramers may, therefore, bind to fOPII and allow activation, much as the dimer of dimers formed by apo-Fur between fOPI and fOPII appears to induce the promoter (see Fig. 5c below). When metals are in excess, Fur tetramerizes and binds also the fOPIII element, promoting repression (Figs 1–3, and also Fig. 6b). On the other hand, when iron is chelated by adding dipyridyl, the prevalent state of Fur becomes dimeric, with binding only to fOPII (Supplementary Fig. 4B). However, binding of the apo-Fur dimer *per se* on fOPII seems to be insufficient to allow induction.

Thus, the deletion of fOPI determines a pleiotropic de-repression of the P*ars* promoter and a loss in the response provoked by iron depletion. This suggests that the central high affinity fOPI operator has a dual role: it is crucial for repression—even though dispensable for the transcriptional response to iron (FeOFF)—and, at the same time, it is required for induction of the P*arsR* promoter by apo-Fur. In fact, two concomitant conditions have to be fulfilled to allow Fur-dependent P*arsR* inducibility: the binding of a tetramer or dimer of dimers to a distal (upstream) position and the absence of binding to the downstream fOPIII element (see Fig. 5c below and ΔfOPIII mutant in Fig. 6b, respectively). These data are consistent with the AFM observation indicating that fOPI is involved both in apo- and holo-Fur promoter-DNA compaction.

Next, we deleted the distal operator encompassing the overlapping apo-Fur and NikR binding sites (fOPII/nOPII). Interestingly, this deletion did not impair significantly the basal levels of transcription from P*arsR*, as it did not impair Fur binding to the other operators (Supplementary Fig. 4C). Instead, as in the case of fOPI deletion, we observed a loss of inducibility in response to iron depletion (Fig. 5c). Thus, both fOPI and fOPII are required for Fur-dependent induction of P*arsR*. In light of the apo-Fur mediated DNA compaction observed with AFM, the data indicate that the distal operator fOPII approaches the central operator fOPI through Fur-mediated interactions to ensure P*arsR* induction upon iron chelation. Intriguingly, a similar mechanism has been postulated for the control of the P*fur* promoter itself[31] (see 'Discussion' section).

To explore the function of nOPI, targeted site-directed mutagenesis of the NikR binding consensus sequence was performed, substituting three critical nucleotides of the hemi-operator motif (ATA→GGG)[14], while leaving the −10 box intact (nOPI*, Fig. 5d). Footprinting analysis confirmed that binding of NikR to this mutated element was abolished (Supplementary Fig. 4D), with a consequent drastic reduction of the transcript levels (Fig. 5d). Nevertheless, the transcriptional response resulting in iron-dependent repression (FeOFF) was maintained, reproducing to a large extent the responses observed at the endogenous P*ars* promoter in the Δ*nikR* strain (see Fig. 1). These results indicate that NikR can either activate the *ars* promoter directly, as a class I activator, or indirectly through an anti-repression mechanism that impairs the binding of Fur to the *arsR* promoter. However, although some MerR-type activators have been reported to activate transcription by binding and changing the conformation of a nonoptimal spacer sequence between −10 and −35 boxes[32], the position of the nOPI operator would be rather unconventional for a RHH-regulator-like NikR to act as such a transcriptional activator. Accordingly, the primer extension analyses clearly show that in the double mutant background (Δ*fur*Δ*nikR*), the endogenous P*ars* promoter is constitutively de-repressed (Fig. 1). This is a strong indication that NikR may act as an anti-repressor of the Fur-regulated *ars* promoter, by binding to nOPI.
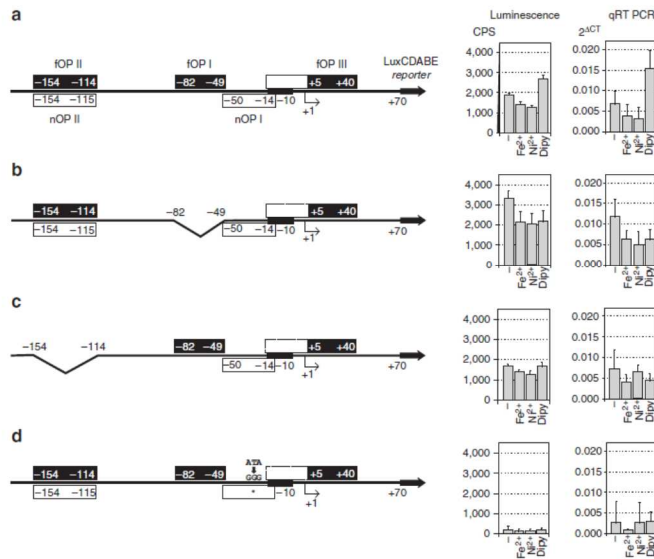
35

Figure 5 | Functional analysis of Fur and NikR operators on *ParsR*. Expression and transcription levels monitored through a *ParsR–lux* reporter fusion. Histograms are shown for *in vivo* luminescence and *in vitro* RT-qPCR. (**a**) Wild-type *ParsR* promoter; (**b**) *ParsR* lacking the central holo-Fur operator (ΔfOPI); (**c**) *ParsR* lacking the distal Fur and NikR operators (ΔfOPII/nOPII); (**d**) *ParsR* mutated in the NikR proximal operator nOPI* (ATA→GGG). Fur and NikR operators are depicted as black and white boxes, respectively. From left to right, bars represent the untreated control (−), a 15 min treatment with iron (Fe^{2+}), nickel (Ni^{2+}) and iron chelator (Dipy). Error marks indicate the standard deviation of eight (luminescence) and four (RT-qPCR) independent experiments.

NikR has an antagonistic effect on Fur binding and repression. To further characterize the regulatory interplay between Fur and NikR, we performed competitive footprinting experiments by varying the concentrations of one regulator in the presence of a fixed amount of the second, and vice versa. Except for the distal overlapping fOPII/nOPII operator, for which both proteins competed as expected, increasing amounts of Fur had no effect on the binding affinity of NikR to nOPI, indicating absence of positive or negative cooperativity at this operator (data not shown). Conversely, when increasing amounts of NikR were added to the preformed Fur–DNA complexes, we observed a marked reduction of the Fur footprint at the low-affinity fOPIII operator, together with the anticipated Fur-NikR competition for the distal fOPII site. Interestingly, protection of the high-affinity operator fOPI remained unaltered (Fig. 6a).

These results further support the hypothesis that binding of NikR to the *ars* promoter impairs binding of Fur to fOPII and to the fOPIII low-affinity operator, most probably by destabilizing the repressive *ParsR* DNA compaction revealed by AFM, in agreement with the putative anti-repressor function of NikR. To validate this hypothesis, we quantified by RT–qPCR the transcript levels of the *ParsR lux* reporter constructs mutated in the principal Fur and NikR operators (fOPI and nOPI) and in the low-affinity fOPIII Fur operator, in different genetic backgrounds (Fig. 6b). In a wild-type background, deletion of fOPI resulted in de-repression of *ParsR,* while a stronger de-repression of the promoter was observed in the Δ*fur* background or when the fOPIII operator was deleted. On the contrary, mutagenesis of the

proximal NikR binding site (ATA→GGG, nOPI*) determined a substantial downregulation of *Pars*. When the latter construct was analysed in a Δ*fur* genetic background, the transcript levels increased more than 10-fold, exceeding the levels observed in the case of fOPI deletion. Thus, the strong downregulation observed after nOPI disruption is a consequence of Fur hyper-repression rather than loss of NikR activation. Finally, when the nOPI* mutation was combined with a deletion of the low affinity fOPIII Fur operator, Fur hyper-repression was relieved, partially reproducing the results obtained for nOPI* in the Δ*fur* strain. Overall, these data demonstrate that fOPIII-mediated promoter compaction is a key element for the repression of *arsR* transcription and that the anti-repressive effect of NikR arises from the antagonistic effect on Fur binding to fOPII and fOPIII. These data also show that the three Fur operators synergistically contribute to *ParsR* repression, since deletion of either fOPI, fOPII or fOPIII fails to de-repress *ParsR* at the same levels observed in the Δ*fur* knockout strain. This supports the evidence of a repressive holo-Fur-dependent DNA compaction of the *arsR* promoter, which can be unwrapped by holo-NikR binding.

Discussion

Complex promoter architectures, allowing binding of multiple regulators to different operators, provide layers of integration for coordinated transcriptional responses to diverse environmental stimuli. Although to date, relatively few examples have been experimentally investigated in mechanistic detail, DNA looping or bending was frequently shown to be a common hallmark. The
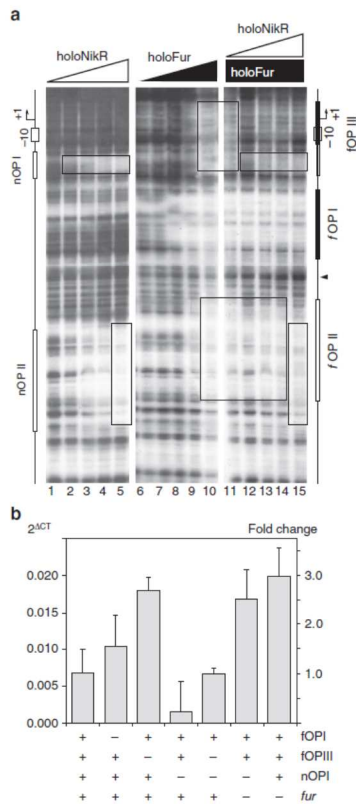
36

Figure 6 | NikR impairs Fur binding to fOPII and fOPIII. (a) Competitive footprinting experiment. Lanes 1–5: protection pattern with increasing holo-NikR concentration (0, 4, 8, 16 and 32 nM NikR tetramer, respectively). Lanes 6–10: protection pattern with increasing holo-Fur concentration (0, 4, 8, 17 and 35 nM Fur tetramer, respectively). Lanes 11–15: protection pattern with increasing holo-NikR concentration (as in lanes 1–5) in the presence of 70 nM Fur tetramer. A schematic map of the promoter region is depicted on the right side of the gels. Dashed boxes outline the competitive binding to the distal operator fOPII and impairment of Fur binding to fOPIII upon NikR binding to nOPI. **(b)** Functional analysis of the low-affinity holo-Fur operator (fOPIII) and of the NikR anti-repression element (nOPI). Bars represent the mRNA levels of the P*arsR-lux* reporter fusion assayed by RT–qPCR in different genetic backgrounds: wild-type, ΔfOPI, ΔfOPIII, nOPI*, nOPI*-ΔfOPIII, nOPI*-Δ*fur* and Δ*fur* mutants. Error marks indicate the standard deviation of two biological replicates, each analysed twice in independent RT–qPCR runs.

GalR-HU repressosome or the CAP-antagonized AraC-looping represent prototypical examples[33,34]. Several advantages have been associated with DNA bending, looping and compaction, including a higher local concentration of the repressor[3,35], fast switching between repressed and de-repressed states due to

prompt recapture of the regulator by the main operator[6], attenuation of stochastic fluctuations and transcriptional bursts[36], faster recognition of target sites[37] and even bistability[38].

Here, we provide the first evidence that a member of the Fur regulators family is capable of inducing different DNA compaction according to the metallation state of the protein. In particular, on iron withdrawal, Fur forms dimers that bind the operators in the upstream promoter region by condensing the intervening DNA, thus inducing *arsR* transcription under iron-limiting conditions. Conversely, in the presence of iron, promoter compaction is achieved through the formation of a nucleoprotein complex involving three holo-Fur tetramers bound to three distinct operators. This mechanism envisages sequential binding events of the repressor as captured by AFM (Fig. 7a). The operators appear to be cooperatively involved in the repression of the *arsR* promoter, much alike the three operators of the Lac operon[39]. The observation that single deletions of fOPI, fOPII and fOPIII fail to de-repress the promoter at the same levels observed in the Δ*fur*-knockout strain (Figs 5 and 6), strengthen this interpretation. Thus, although the Fur central operator fOPI does not overlap the core promoter elements as often observed for canonical repressors, the bidentate nature of the *arsR* promoter readily contributes to enhance repression[5]. Bidentate promoter architectures have been shown to increase the effective repressor concentration at the principal operator by binding the repressor to auxiliary operators and exploiting DNA looping[40]. Notably, our results indicate that this mechanism may be conserved in the Fur repressor family, since these regulators form higher order oligomers and bind multiple operators in many bacterial species (see Introduction).

A particularly interesting aspect of these findings is that different metal ions (Ni^{2+} and Fe^{2+}) appear to affect transcription positively or negatively by modulating DNA compaction, according to the metallation state of the two regulators (Fig. 7b). Although the precise DNA path within the Fur nucleoprotein complex cannot be resolved by AFM, thus precluding the possibility to discriminate between looping and wrapping, functionally similar mechanisms have been observed at several DNA looping-prone promoters, demonstrating both negative and positive control according to the presence of different effectors modulating DNA topology[2]. In particular, the anti-repressive effect of NikR observed on the Fur-dependent compaction of the P*arsR* promoter, functionally recalls the disruptive effect of CRP on AraC-mediated loop formation at the *ara* operon[33]. Thus, the specific and opposite transduction of cognate stimuli (specific metal ions or distinct sugars) appears to be similarly modulated by a balance of DNA condensation and decondensation mechanisms, mediated by different effectors. Interestingly, the presence of an antagonistic operator, promoting the disruption of the interaction between the main and auxiliary operators of the main regulator, seems to be a common theme in the architecture of these complex promoters (for example, CRP versus araI1 and araO2 in P*BAD*, CRP versus O1 and O3 in P*lac* and nOPI versus fOPI and fOPIII in P*arsR*) (Supplementary Fig. 5). This suggests promoter compaction and relaxation as an evolutionary conserved mechanism to integrate transcriptional responses at bacterial promoters.

Remarkably, this complex-promoter architecture, made of overlapping and adjacent Fur and NikR cis elements, is found at several metal-responsive promoters in *H. pylori*. For example, the architecture of the *fur* promoter itself structurally and functionally resembles that of the *arsR* promoter (Supplementary Fig. 5)[31]. Likewise, the divergent P*exbB*–P*nikR* promoter region encompasses three Fur operators, including a central element[14]. Notably, in both P*fur* and P*exbB*–P*nikR*, the NikR operators
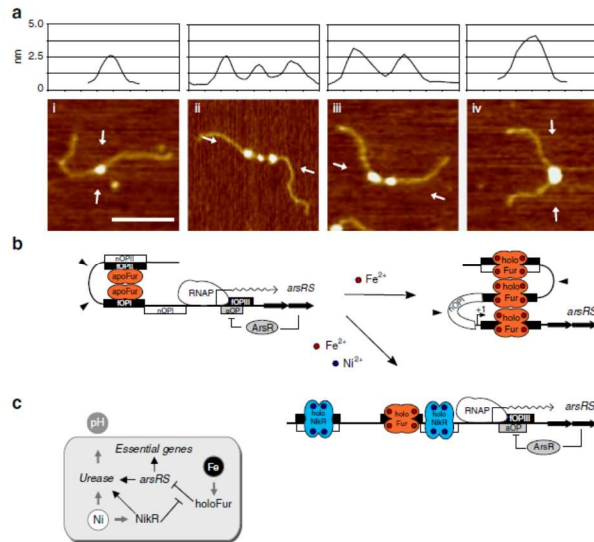
37

Figure 7 | ParsR regulation model. Scheme of ParsR regulation. (**a**) AFM images of different holo-Fur/ParsR pseudo-knotting intermediates. The evident shortening of the DNA fragment and the concomitant enlargement of the nucleo-protein complex are indicative of a significant DNA condensation of the arsR promoter region and Fur oligomerization. (**b**) Proposed FeOFF-NikRON model for ParsR transcription regulation. At low iron concentration, apo-Fur forms dimers that bind to the upstream operators fOPI and fOPII, looping the intervening DNA but leaving the promoter elements open for RNAP binding and transcription. At high iron concentration, holo-Fur forms tetramers and higher order oligomers that condense the promoter DNA by binding to the three operator sites fOPI, fOPII and fOPIII, thus occluding RNAP binding (FeOFF). In the presence of nickel, holo-NikR binds to the operators nOPI and nOPII preventing Fur binding and promoter condensation, a condition that favours RNAP binding and arsR transcription (NikRON). An additional layer of control is introduced by the previously reported feedback regulation mechanism of arsR transcription. (**c**) Coherence of metal-dependent arsRS regulation with H. pylori acid acclimation needs: NikR-dependent antirepression of ParsR is possible only when the intracellular nickel levels are sufficiently high to cofactor the urease nickel-enzyme.

match the positions mapped on the ParsR promoter, with a distal NikR element overlapping the upstream auxiliary Fur operator and a second proximal NikR element located between the central and the downstream auxiliary Fur operators (Supplementary Fig. 5). These similarities suggest that promoter compaction and anti-repression mechanisms may be adopted in the regulation of other operons where an integrated response to iron and nickel is required.

The tight transcriptional integration between these two metal ions is not surprising, since they may compete for the same uptake and storage proteins, activate similar redox detoxifications systems and, in some cases, participate together as cofactors of key metallo-enzymes (for example, Ni–Fe hydrogenase)[41]. In this respect, our results contribute to unify acid-acclimation and metal-dependent responses in a mechanistically and physiologically coherent model. Specifically, the acid-inducible and ArsR-dependent expression of the H. pylori urease cistrons is supported only when the intracellular Ni^{2+} levels are sufficiently high to cofactor NikR and the urease holo-enzyme (NikRON) and iron levels are not too high to cause redox toxicity (Fig. 7c). At low nickel concentration, not only is the expression of urease not useful, but also other vital functions dependent on the essential gene targets of ArsR need to be downregulated since the growth in the acid gastric niche is possible only under the pH-buffering conditions provided by urease. Similarly, if the

intracellular concentration of iron is too high, arsR transcription, and thereby the expression of essential regulatory targets and ultimately growth, will be downregulated even in the presence of nickel (FeOFF), to avoid redox stress, consistent with the microaerophilic metabolism of H. pylori and the involvement of Fur in redox regulation[11,42]. Finally, ParsR is also controlled through the apparently negative auto-regulation by ArsR[26], introducing an additional layer of feedback regulation in ArsR homeostasis.

This signal integration logic well fits the pathobiontic nature of H. pylori, balancing metabolic needs and stealth behaviour to avoid host responses and counter acidic as well as oxidative stresses.

In conclusion, our results provide for the first time evidence of a metal-dependent mechanism of DNA compaction mediated by a member of the widespread Fur family of metallo-regulators (Fig. 7b). This mechanism feeds directly into the control of H. pylori acid acclimation and growth, through short-range DNA interactions of the arsR promoter, antagonized by NikR. Together with DPS, a nucleoid-associated protein that mediates the pH-dependent DNA condensation in H. pylori[43], Fur provides the capability to condense DNA in a metal-dependent fashion, a feature that may be also relevant for the formation of H. pylori coccoid forms, especially in the late stationary phase, when Fur concentration has been reported to increase[19].

38

More in general, we notice that together with the DNA-shaping features reported in this study, many Fur orthologues appear to recapitulate features characteristic of NAPs and global regulators such as elevated number of intracellular copies, the formation of higher order multimers, promiscuous binding specificities, including DNA shape readout and minor groove readout mechanisms[12,44], as well as elevated numbers of genomic binding sites, even at 'orphan' positions, which map distantly from TSSs[19,45,46].

If transcriptional regulators evolved from nucleoid-associated proteins[47], it is striking to notice that Fur proteins are conserved also in bacteria that have undergone reductive evolution, finally encoding only few classical transcription factors, and a reduced cohort of nucleoid-associated proteins (for example, *Mycoplasma*[48], *Bacteroides*[49], and so on). Therefore, it is not unrealistic to hypothesize that many Fur orthologues may play the double role of specific metallo-regulators as well as structural mediators of the nucleoid organization through DNA looping or wrapping interactions.

Methods

Bacterial strains and culture conditions. *H. pylori* strains (Supplementary Table 1), were revitalized from glycerol stocks on Brucella broth agar plates added with 5% fetal calf serum and 0.2% cyclohexamide and Dent's antibiotic supplement under microaerophilic conditions (Oxoid) for 2 days. After re-streaking on fresh plates, bacteria were cultured in a 9% CO_2–91% air atmosphere at 37 °C and 95% humidity in a water-jacketed incubator (Thermo Forma Scientific). Liquid cultures were grown in modified Brucella broth medium supplemented with 5% fetal calf serum, 0.2% cyclohexamide and Dent's antibiotic supplement in glass flasks or 25 cm³ sterile plastic flasks with vented cap (Corning).

Primer extension analysis. Primer extension analysis on the native *ParsR* promoter was performed using oligo 166 pe3 (Supplementary Table 2), as previously described in ref. 50.

ParsR-lux reporter strains. Bioluminescent *ParsR* reporter strains were generated by natural transformation of a G27 *lux* acceptor strain[30]. In particular, the promoterless *luxCDABE* reporter was put under the control of the wild-type or mutant forms of the *arsR* promoter by double homologous recombination following transformation with 5 µg of a pVCC suicide vector (Supplementary Table 3); positive clones were selected on Brucella broth agar plates supplemented with chloramphenicol at 30 µg ml⁻¹. The *ParsR* wild-type promoter was amplified from genomic DNA by PCR using oligonucleotides 166 pe3/166Alida (Supplementary Table 2). The amplicon was cloned into a pGEMT-Easy TA-cloning vector (Promega). From this plasmid, the promoter sequence was excised with NcoI/NdeI digestion, made blunt-ended with Klenow fragment and ligated to the blunt-ended BamHI site of pVCC (Supplementary Table 3). The mutant promoters were obtained as synthetic genes from GENEWIZ (Supplementary Table 4), subcloned into the BamHI site of pVCC and validated by sequencing. The constructs were used to transform the G27 *lux* acceptor strain (Supplementary Table 1). For bioluminescence, 10 ml of pre-heated Brucella broth medium were inoculated with an overnight culture of the desired strain (starting D_{600} 0.07) and grown until early exponential phase. The culture was divided into four 1-ml aliquots in a 24-well tissue culture plate (Corning) and treated for 30 min with 1 mM $(NH_4)_2Fe(SO_4)_2$, 1 mM $NiSO_4$, or 150 µM 2-2 dipyridyl. Luminescence emission was monitored every 20 min with a EnSpire Multiplate reader (PerkinElmer). For transcriptional analysis with RT–qPCR, a 20 ml culture obtained as described was divided into four 5 ml aliquots and treated with the same metals or chelators before RNA extraction, cDNA synthesis with the oligo luxC3, and qPCR with primers LuxRT FW/RV (Supplementary Table 2), all according to ref. 42.

DNAse I footprinting. NikR and Fur recombinant proteins were purified as previously described[27,50]. For probe preparation, plasmids carrying either the wild-type or the mutant *ParsR* promoter (Supplementary Table 3) were linearized with NcoI or BamHI, 5′ end labelled with [γ-³²P]-ATP by T4 polynucleotide kinase and gel purified after a second cut at the 3′ end; 15 fmol of labelled probe were used for each footprinting reaction. The footprinting assays with Fur alone were performed in 1X Fur Footprinting Buffer (FPB) according to ref. 42, incubating different amounts of protein for 20 min at room temperature with 300 ng of nonspecific competitor salmon sperm DNA, 150 µM $(NH_4)_2Fe(SO_4)_2$ or 150 µM 2-2 dipyridyl and 15 fmol of labelled DNA in a final volume of 50 µl. Footprinting assays with NikR were performed similarly, in 1X NikR FPB according to ref. 27. NikR was pre-equilibrated in 1X NikR FPB overnight at 4 °C, in a final volume of 10 µl.

Footprinting assays performed with both Fur and NikR were made in 1X Competitive FPB (20 mM HEPES pH 7.85; 50 mM KCl; 0.02% Igepal; 0.4 dithiothreitol (DTT), 10% glycerol, containing 300 ng of sonicated salmon sperm DNA, 150 µM of $(NH_4)_2Fe(SO_4)_2$ or 150 µM 2-2 dipyridyl and 15 fmol of labelled DNA probe. Fur was pre-equilibrated in 1X Fur FPB with 5 mM DTT for 15 min before addition to the mix. After 10 min of probe incubation with Fur at room temperature, NikR and 150 µM $NiSO_4$ were added, and the reaction was incubated for additional 10 min before DNA digestion. The partial digestion of the labelled probes was carried out in the presence of 10 mM $CaCl_2$ and 5 mM $MgCl_2$, varying DNase I concentration (0.05–0.3 U; Novagen) and incubation times (60–75 s), to reach comparable digestion ladders in sequencing gels.

Sample preparation for AFM imaging. The five globular proteins used to obtain the calibration curve relating AFM volume and molecular weight were: *Equus caballus* myoglobin (17 kDa), Bovine pancreas DNase I (30 kDa), Bovine serum albumin (67 kDa), Bovine liver catalase (250 kDa) and *Escherichia coli* RNA polymerase-σ[70] (458 kDa; Supplementary Fig. 1). Apo-Fur and holo-Fur were prepared by incubating the protein with 150 µM of 2,2′-dipyridyl or 150 µM $(NH_4)_2Fe(SO_4)_2 \cdot 6H_2O$, respectively, in binding buffer (25 mM sodium phosphate buffer pH 8, 70 mM NaCl, 15 mM KCl, 0.1 mM DTT) at room temperature for 15 min. To avoid subunits dissociation upon deposition, the protein was cross-linked with 10 mM glutaraldehyde for 2 min. The crosslinking reaction was quenched with 1 M Tris-HCl pH 8 (final concentration of 60 mM). Each protein was diluted in deposition buffer to a final concentration of 5–50 nM and deposited onto freshly cleaved mica as described above.

The 818 bp-long DNA template harbouring the *ParsR* promoter was obtained by PCR from plasmid pGEM-*ParsR* using Taq DNA polymerase in standard reaction conditions. pGEM-*ParsR* was constructed by cloning the *ParsR* promoter region (from position −203 to +61 with respect to TSS) of *H. pylori* G27 into the poly-linker of plasmid pGEM-T easy (Promega; Supplementary Table 3). The DNA fragment was gel purified using an Elutrap apparatus (Schleicher & Schuell, Keene NH), phenol/chloroform extracted, ethanol precipitated and resuspended in 5 mM Tris-HCl pH 7.4. The DNA concentration was determined by absorbance at 260 nm.

The 1,129 bp-long DNA template used in experiments shown in Supplementary Fig. 3 was obtained by PCR using primers *ParsR*_For and *ParsR*_Rev (Supplementary Table 2) and plasmid pGEM-*ParsR2* as template (Supplementary Table 3). pGEM-*ParsR2* was obtained from pGEM-*ParsR* in two steps. First, a BamHI restriction site was inserted between the fOPI and fOPII sites by mutagenic PCR using primers ParsRmut_For and ParsRmut_Rev (Supplementary Table 2). Next, a 315 bp DNA insert obtained by PCR from pET28b plasmid using primers ParsRins_For and ParsRins_Rev (Supplementary Table 2) was cloned into the created BamH1 restriction site. The DNA fragment was purified as described above.

Complexes assembly for AFM imaging. Fur–DNA complexes were assembled in 1X Fur footprinting buffer containing either 150 µM 2′-dipyridyl (apoFur) or 150 µM $(NH_4)_2Fe(SO_4)_2 \cdot 6H_2O$ (holo-Fur). The 10 µl reaction containing 9 nM DNA and 380 nM Fur dimers was incubated for 15 min at 25 °C. Afterwards, glutaraldehyde at a final concentration of 10 mM was added to the reactions, followed by an incubation of 2 min at room temperature. The crosslinking of the Fur-binding reaction with glutaraldehyde was introduced because Fur oligomers had the tendency to disrupt upon deposition onto mica (Supplementary Fig. 2). The crosslinking reaction was quenched with 1 M Tris-HCl pH 8 (final concentration 60 mM). Two microlitres of the reaction were diluted in 20 µl of deposition buffer (4 mM HEPES pH 7.4, 10 mM NaCl, 2 mM $MgCl_2$) and immediately deposited onto freshly cleaved mica. After 3 min, the mica disk was rinsed with milliQ water and dried with a gentle stream of nitrogen. AFM analysis of the binding of NikR to the *ParsR* promoter was more straightforward because holo-NikR forms stable tetramers, which are not disrupted upon deposition onto mica and do not form oligomers of high molecular mass. NikR–DNA complexes were assembled in 1X NikR FPB (20 mM HEPES pH 7.4, 50 mM KCl, 1 mM $NiSO_4$, 0.1 mM DTT). The 10 µl reaction containing 10 nM DNA and 640 nM NikR tetramers was incubated for 15 min at 25 °C. The reaction was diluted 1:10 in deposition buffer and deposited onto freshly cleaved mica for 3 min. Afterwards, the mica disk was rinsed with milliQ water and dried with nitrogen. AFM imaging was carried out with tapping mode in air with a Nanoscope IIIA (Digital Instruments, Santa Barbara, CA, USA) microscope equipped with a 12 µm scanner (E scanner) and commercial silicon cantilevers (MikroMasch, Tallinn, Estonia). Square images of 512 × 512 pixels were collected with a scan size of 1 µm at a scan rate of two lines per second.

AFM image analysis. Images were analysed using locally written Matlab scripts and Gwyddion software (v. 2.37). DNA contour length measurements were performed by manually tracing the DNA contour from one end to the other. The digitized DNA trace served as an outline to identify the subset of pixels with higher intensity of the DNA backbone. Images were skeletonized with the *bimorph* built-in function of Matlab to generate eight connected chaincode of unit thickness and the DNA contour length was determined by (n_e, n_o)-characterization using the

following contour length estimator: PAGE *Arabic 21 $L_{DNA} = (0.963 \ n_e + 1.362 \ n_o) \times S/W$, where: n_e and n_o are the number of even- and odd-chain pixel, respectively, S is the image scan size (1,000 nm), W is the image width (512 pixels; ref. 51). Because the DNA path in proximity of the protein cannot be seen, the DNA trace was made to pass through the centre of the protein. Short distances between Fur oligomers bound to the different operators were measured with the straight line measuring tool of the Nanoscope software. The position of Fur oligomers or NikR tetramers bound along the DNA template was selected with the mouse by clicking in the centre of each globular feature.

To assess the stoichiometry of these oligomers, we constructed a molecular mass–volume calibration curve using a set of globular proteins of known molecular mass (Supplementary Fig. 1). Protein volume analysis of molecular weight markers, apo-Fur and holo-Fur in the absence of DNA were measured using the thresholding algorithm of the Gwyddion particle analysis procedure. Volume of Fur oligomeric states and NikR tetramers bound to the different operator sites were measured by single grain analysis using Matlab and ad hoc scripts. After defining the particle boundaries with the free hand tool, the mean height of the boundary pixels was determined and used as reference background. The volume of the particle was then computed by multiplying the area of the particle boundary by the average pixel height, relative to the reference background, of the particle.

Notice that for small proteins, the DNA contributes significantly to the volume of the complex and, therefore, it must be taken into account when inferring its molecular mass. A small DNA compaction is generally due to the different path that the DNA can take upon deposition. Namely, if the complex sticks to the surface in an orientation such that DNA has to detach from the surface to overcome the protein, its DNA contour length will be reduced by a few nanometers depending on the size of the protein. As the volume of the complexes increases, the uncertainty of the volume measurements becomes larger. This is, in part, due to the broadening effect of the AFM tip, which is larger for bigger objects and in part due to the fact that the density of the complex oligomeric nucleo-protein aggregates may be lower than that of the globular proteins used as standards.

References

1. Dorman, C. J. Genome architecture and global gene regulation in bacteria: making progress towards a unified model? *Nat. Rev. Microbiol.* **11**, 349–355 (2013).
2. Matthews, K. S. DNA looping. *Microbiol. Rev.* **56**, 123–136 (1992).
3. Schleif, R. DNA looping. *Annu. Rev. Biochem.* **61**, 199–223 (1992).
4. Hochschild, A., Douhan, J. & Ptashne, M. How lambda repressor and lambda Cro distinguish between OR1 and OR3. *Cell* **47**, 807–816 (1986).
5. Becker, N. A., Greiner, A. M., Peters, J. P. & Maher, L. J. Bacterial promoter repression by DNA looping without protein-protein binding competition. *Nucleic Acids Res.* **42**, 5495–5504 (2014).
6. Cournac, A. & Plumbridge, J. DNA looping in prokaryotes: experimental and theoretical approaches. *J. Bacteriol.* **195**, 1109–1119 (2013).
7. Dunn, T. M., Hahn, S., Ogden, S. & Schleif, R. F. An operator at -280 base pairs that is required for repression of araBAD operon promoter: addition of DNA helical turns between the operator and promoter cyclically hinders repression. *Proc. Natl Acad. Sci. USA* **81**, 5017–5020 (1984).
8. Lyubchenko, Y. L., Shlyakhtenko, L. S., Aki, T. & Adhya, S. Atomic force microscopic demonstration of DNA looping by GalR and HU. *Nucleic Acids Res.* **25**, 873–876 (1997).
9. Browning, D. F., Grainger, D. C. & Busby, S. J. Effects of nucleoid-associated proteins on bacterial chromosome structure and gene expression. *Curr. Opin. Microbiol.* **13**, 773–780 (2010).
10. Troxell, B. & Hassan, H. M. Transcriptional regulation by Ferric Uptake Regulator (Fur) in pathogenic bacteria. *Front. Cell. Infect. Microbiol.* **3**, 59 (2013).
11. Fillat, M. F. The FUR (ferric uptake regulator) superfamily: diversity and versatility of key transcriptional regulators. *Arch. Biochem. Biophys.* **546**, 41–52 (2014).
12. Agriesti, F. *et al.* FeON-FeOFF: the Helicobacter pylori Fur regulator commutates iron-responsive transcription by discriminative readout of opposed DNA grooves. *Nucleic Acids Res.* **42**, 3138–3151 (2014).
13. D'Autréaux, B. *et al.* Reversible redox- and zinc-dependent dimerization of the *Escherichia coli* fur protein. *Biochemistry* **46**, 1329–1342 (2007).
14. Delany, I. *et al.* In vitro analysis of protein-operator interactions of the NikR and fur metal-responsive regulators of coregulated genes in *Helicobacter pylori*. *J. Bacteriol.* **187**, 7703–7715 (2005).
15. de Lorenzo, V., Giovannini, F., Herrero, M. & Neilands, J. B. Metal ion regulation of gene expression. Fur repressor-operator interaction at the promoter region of the aerobactin system of pColV-K30. *J. Mol. Biol.* **203**, 875–884 (1988).
16. Friedman, Y. E. & O'Brian, M. R. A novel DNA-binding site for the ferric uptake regulator (Fur) protein from Bradyrhizobium japonicum. *J. Biol. Chem.* **278**, 38395–38401 (2003).
17. Le Cam, E., Frechon, D., Barray, M., Fourcade, A. & Delain, E. Observation of binding and polymerization of Fur repressor onto operator-containing DNA with electron and atomic force microscopes. *Proc. Natl Acad. Sci. USA* **91**, 11816–11820 (1994).
18. Pallarés, M. C. *et al.* Sequential binding of FurA from Anabaena sp. PCC 7120 to iron boxes: exploring regulation at the nanoscale. *Biochim. Biophys. Acta* **1844**, 623–631 (2014).
19. Danielli, A. *et al.* In vivo dissection of the *Helicobacter pylori* Fur regulatory circuit by genome-wide location analysis. *J. Bacteriol.* **188**, 4654–4662 (2006).
20. Gancz, H., Censini, S. & Merrell, D. S. Iron and pH homeostasis intersect at the level of Fur regulation in the gastric pathogen *Helicobacter pylori*. *Infect. Immun.* **74**, 602–614 (2006).
21. Pflock, M., Kennard, S., Finsterer, N. & Beier, D. Acid-responsive gene regulation in the human pathogen *Helicobacter pylori*. *J. Biotechnol.* **126**, 52–60 (2006).
22. Pflock, M., Kennard, S., Delany, I., Scarlato, V. & Beier, D. Acid-induced activation of the urease promoters is mediated directly by the ArsRS two-component system of *Helicobacter pylori*. *Infect. Immun.* **73**, 6437–6445 (2005).
23. Valenzuela, M., Albar, J. P., Paradela, A. & Toledo, H. *Helicobacter pylori* exhibits a fur-dependent acid tolerance response. *Helicobacter* **16**, 189–199 (2011).
24. van Vliet, A. H. M., Ernst, F. D. & Kusters, J. G. NikR-mediated regulation of *Helicobacter pylori* acid adaptation. *Trends Microbiol.* **12**, 489–494 (2004).
25. Danielli, A., Amore, G. & Scarlato, V. Built shallow to maintain homeostasis and persistent infection: insight into the transcriptional regulatory network of the gastric human pathogen *Helicobacter pylori*. *PLoS Pathog.* **6**, e1000938 (2010).
26. Dietz, P., Gerlach, G. & Beier, D. Identification of target genes regulated by the two-component system HP166-HP165 of *Helicobacter pylori*. *J. Bacteriol.* **184**, 350–362 (2002).
27. Zambelli, B. *et al.* High-affinity Ni2+ binding selectively promotes binding of *Helicobacter pylori* NikR to its target urease promoter. *J. Mol. Biol.* **383**, 1129–1143 (2008).
28. Stoof, J., Kuipers, E. J. & van Vliet, A. H. M. Characterization of NikR-responsive promoters of urease and metal transport genes of *Helicobacter mustelae*. *Biometals* **23**, 145–159 (2010).
29. Cellai, S. *et al.* Upstream promoter sequences and alphaCTD mediate stable DNA wrapping within the RNA polymerase-promoter open complex. *EMBO Rep.* **8**, 271–278 (2007).
30. Vannini, A. *et al.* A convenient and robust in vivo reporter system to monitor gene expression in the human pathogen *Helicobacter pylori*. *Appl. Environ. Microbiol.* **78**, 6524–6533 (2012).
31. Delany, I., Spohn, G., Rappuoli, R. & Scarlato, V. An anti-repression Fur operator upstream of the promoter is required for iron-mediated transcriptional autoregulation in *Helicobacter pylori*. *Mol. Microbiol.* **50**, 1329–1338 (2003).
32. Brown, N. L., Stoyanov, J. V., Kidd, S. P. & Hobman, J. L. The MerR family of transcriptional regulators. *FEMS Microbiol. Rev.* **27**, 145–163 (2003).
33. Lobell, R. B. & Schleif, R. F. AraC-DNA looping: orientation and distance-dependent loop breaking by the cyclic AMP receptor protein. *J. Mol. Biol.* **218**, 45–54 (1991).
34. Semsey, S., Tolstorukov, M. Y., Virnik, K., Zhurkin, V. B. & Adhya, S. DNA trajectory in the Gal repressosome. *Genes Dev.* **18**, 1898–1907 (2004).
35. Oehler, S. & Müller-Hill, B. High local concentration: a fundamental strategy of life. *J. Mol. Biol.* **395**, 242–253 (2010).
36. Vilar, J. M. G. & Saiz, L. DNA looping in gene regulation: from the assembly of macromolecular complexes to the control of transcriptional noise. *Curr. Opin. Genet. Dev.* **15**, 136–144 (2005).
37. Li, G.-W., Berg, O. G. & Elf, J. Effects of macromolecular crowding and DNA looping on gene regulation kinetics. *Nat. Phys.* **5**, 294–297 (2009).
38. Ozbudak, E. M., Thattai, M., Lim, H. N., Shraiman, B. I. & Van Oudenaarden, A. Multistability in the lactose utilization network of *Escherichia coli*. *Nature* **427**, 737–740 (2004).
39. Oehler, S., Eismann, E. R., Krämer, H. & Müller-Hill, B. The three operators of the lac operon cooperate in repression. *EMBO J.* **9**, 973–979 (1990).
40. Becker, N. A., Peters, J. P., Lionberger, T. A. & Maher, L. J. Mechanism of promoter repression by Lac repressor–DNA loops. *Nucleic Acids Res.* **41**, 156–166 (2013).
41. Danielli, A. & Scarlato, V. Regulatory circuits in *Helicobacter pylori*: network motifs and regulators involved in metal-dependent responses. *FEMS Microbiol. Rev.* **34**, 738–752 (2010).
42. Pelliciari, S., Vannini, A., Roncarati, D. & Danielli, A. The allosteric behavior of Fur mediates oxidative stress signal transduction in *Helicobacter pylori*. *Front. Microbiol.* **6**, 840 (2015).
43. Ceci, P., Mangiarotti, L., Rivetti, C. & Chiancone, E. The neutrophil-activating Dps protein of *Helicobacter pylori*, HP-NAP, adopts a mechanism different

from *Escherichia coli* Dps to bind and condense DNA. *Nucleic Acids Res.* 35, 2247–2256 (2007).

44. Deng, Z. *et al.* Mechanistic insights into metal ion activation and operator recognition by the ferric uptake regulator. *Nat. Commun.* 6, 7642 (2015).

45. Butcher, B. G. *et al.* Characterization of the Fur Regulon in *Pseudomonas syringae* pv. tomato DC3000. *J. Bacteriol.* 193, 4598–4611 (2011).

46. Butcher, J., Sarvan, S., Brunzelle, J. S., Couture, J.-F. & Stintzi, A. Structure and regulon of Campylobacter jejuni ferric uptake regulator Fur define apo-Fur regulation. *Proc. Natl Acad. Sci. USA* 109, 10047–10052 (2012).

47. Visweswariah, S. S. & Busby, S. J. W. Evolution of bacterial transcription factors: how proteins take on new tasks, but do not always stop doing the old ones. *Trends Microbiol.* 23, 463–467 (2015).

48. Güell, M. *et al.* Transcriptome complexity in a genome-reduced bacterium. *Science* 326, 1268–1271 (2009).

49. Robertson, K. P., Smith, C. J., Gough, A. M. & Rocha, E. R. Characterization of Bacteroides fragilis hemolysins and regulation and synergistic interactions of HlyA and HlyB. *Infect. Immun.* 74, 2304–2316 (2006).

50. Danielli, A. *et al.* Growth phase and metal-dependent transcriptional regulation of the fecA genes in *Helicobacter pylori*. *J. Bacteriol.* 191, 3717–3725 (2009).

51. Rivetti, C. A simple and optimized length estimator for digitized DNA contours. *Cytometry A* 75, 854–861 (2009).

Acknowledgements

Author contributions

D.R., S.P., A.V., L.V. and A.D. performed the molecular and *in vivo* experiments; N.D., S.M. and C.R. carried out the AFM analysis; L.M. and B.Z. provided purified NikR protein; N.D., C.R. and A.D. conceived the experiments with the support of all the authors. C.R. and A.D. wrote the manuscript and provided funding or resources.

Additional information

41

Combining Atomic force and fluorescence microscopies to investigate the bacterial nucleoid morphology

Introduction

Escherichia coli is characterized by two double-layer phospholipid membranes to accomplish proper isolation and functional exchange with the environment. Between the two membranes there is a saccharide polymer called murein or sacculus which maintains the shape of the bacterium and resists to the osmotic pressure of the cell. Within the bacterium, the environment is extremely crowded, being mainly composed by cytosol and nucleoid.

All these elements contribute to define the shape of a bacterium cell.

Because isolated peptidoglycan sacculi retain the shape of intact cells [1], the cell wall was thought to be inherently rigid. However, by means of atomic force microscopy the mechanical properties of isolated and hydrated *E. coli* sacculi were assessed, revealing their flexibility and elasticity [2]. These experiments suggest that in living cells the bacterial cell wall is not a 'hard shell' but rather a structure that retains flexibility. Therefore, it is assumed that the sacculus confers and preserves a defined shape and size of the cell, aided by the dynamics and topology of its biosynthetic processes [3]. Bacteria can use cytoskeletal elements to position proteins involved in peptidoglycan (PG) synthesis and hydrolysis in large, intricately protein complexes, for example in *H. pylori* PG hydrolases (Csd1, Csd2, Csd3, Csd4 and Csd6) dictates the helical shape morphology [3]. The actin-like cytoskeletal protein MreB influences bacterial morphogenesis by coordinating cell wall biosynthesis spatio-temporally. Although directing PG insertion during elongation appears to be the main role of MreB, also chromosome segregation, RNA polymerase binding and topoisomerase IV activation are process in which MreB is involved [4,5].

In addition to the pivot role of MreB, the cross talk between sacculus and the nucleoid is of primary importance for cell division. Although cell division is a simple process, the

division site must be chosen carefully. For instance, division at the pole would produce a non-viable anucleate 'mini-cell'. Conversely, division through the nucleoid would produce at least one non-viable cell. In *E. coli* the division site is placed precisely at mid-cell thanks to the combined action of two negative regulatory systems [6] [7]. In the first one, the Min system prevents division close to the cell poles, by inhibiting Z-ring assembly, whereas in the nucleoid occlusion system the nucleoid acts as a cell cycle 'checkpoint', preventing cell division until the replicated sister chromosomes have been segregated. Therefore, besides acting as a 'template' for specific regulatory proteins, the overall organization and activity of the nucleoid may also play a more general role in regulating division [7]. It is interesting to note that since the *ter* locus appears to leave mid-cell just prior to constriction, this process might also communicate the completion of chromosome segregation to permit cell division [8].

The beginning of replication, such as the separation of the sister chromatid, also has a spatial length control: it seems that the cell can sense its size and decide when it is large enough to start the replication process [9].

The picture that emerges indicates that cell-size control and cell-cycle control are coupled [10]. Zaritsky pointed out that the bacterial width is related to the level of nucleoid complexity, expressed as the amount of DNA in genome equivalents that is associated with chromosome terminus.

Since the morphology of *E.coli* is dependent of the medium in which is cultured [11] I will briefly describe its physiology in Luria-Bertani broth [12] . The recipe for Luria-Bertani broth is as follows. Combine 10 g of tryptone, 5 g of yeast extract, 10 g of NaCl, and 1 liter of distilled water; adjust the pH to 7.0 with 1 N NaOH; and autoclave the mixture for 25 min at 120°C. The tryptone used is a pancreatic digest of casein from cow's milk, and the yeast extract used is an autodigest of *Saccharomyces cerevisiae*. The carbon sources for *E. coli* in Luria-Bertani broth are catabolizable amino acids, not sugars.

LB broth supports *E. coli* growth to an optical density at 600 nm (OD_{600}) of 7 and is limited by the availability of utilizable carbon sources.

The great deal of work on *E. coli* physiology has been carried out with cultures in steady-state growth, often called exponential phase [12]. By definition, during steady-state growth, all intrinsic parameters of the cells such as population averages, mean volume, density and macromolecular composition of the cells remain constants. On the contrary, all extrinsic parameters such as the optical density of the culture, the number of cells per milliliter, the amount of protein per milliliter, the amount of RNA per milliliter and the amount of DNA per milliliter, increase exponentially with precisely the same doubling time [12]. The composition, pH and temperature of the medium all remain constant within the cells detection limits. Cultures in steady state exhibit balanced exponential growth.

Steady-state growth stops at an OD600 of 0.3 in Luria-Bertani broth [12]. At this OD value the average cell mass begin to decrease, indicating that the growth rate decreases and the steady-state growth ends. Interestingly, the intracellular concentration of σ^S increases in Luria-Bertani broth when the OD_{600} reaches about 0.5 [13].

The genomic content of *E coli* strain MG 1655 vary along the growth curve. In rich medium doubling times of *E. coli* is 20 minutes although the time required to replicate and segregate the chromosome is at least 60–90 min. In rapidly growing cells a way to overcome temporal limitation is to initiate a new replication cycle before the previous replication round is completed. This leads to a high genomic content in exponential phase with respect to the stationary phase [14]. In exponential phase it has been reported the presence of 8-16 chromosome equivalent per cell [15,16].

On the other hand, after 20 hours in stationary phase, cells have been reported to be a mixture of cells containing 1 or 2 chromosomes in minimal medium M9 [17] or, a mixture of cells containing a prevalence of 4 chromosomes in LB (plus 0,2%glucose) [17] and after one more day in stationary phase cells contain only one chromosome [17]. In addition, it has to

be pointed out that not only the number of chromosome equivalent but also the set of NAP associated with DNA is phase specific (as described in the NAP conclusion Chapter).

These experimental evidences suggest that the topology of *E. coli* cells is ascribable to the intrinsic mechanical properties of PG and to the number and level of compactness of the chromosomes, both depending on the phase of growth.

During my PhD thesis I have developed a combined (hybrid) Atomic Force Microscopy - Fluorescence Microscopy procedure (AFM-FM). The combined AFM-FM approach can have clear advantages; by means of AFM highly resolved topology of the cells is collectable whereas by FM is possible determine the precise position and organization of the nucleoid inside the cell. By overlapping AFM and FM images of the same cell it is possible to correlate the topology of the *E. coli* cells, the structural transition of the nucleoid and how such transitions can specifically influence the global morphology of the cell.

Result and Discussion

AFM investigation of *E. coli* cells morphology

Atomic force and fluorescence microscopies are very different technique. AFM displays high spatial resolution but it is characterized by long time of image acquisition, on the other hand, fluorescence microscopy is a very fast technique able to imaging a high number of bacteria cell in short time.

Due to the time consuming nature of AFM I have started with optimization of bacterial cell deposition for AFM imaging employing different procedures to prepare the cellular samples.

It's important to prepare a sample with a high cell density in order to collect the maximum number of bacteria cell in one single AFM image (AFM Park XE 100 AFM I've used is able to take 40x40 μm images with a resolution of 2048 pixel in one hour).

I have employed poly L-ornithine coated glass in order to improve the bacterial cells adhesion onto the support (Figure 1).
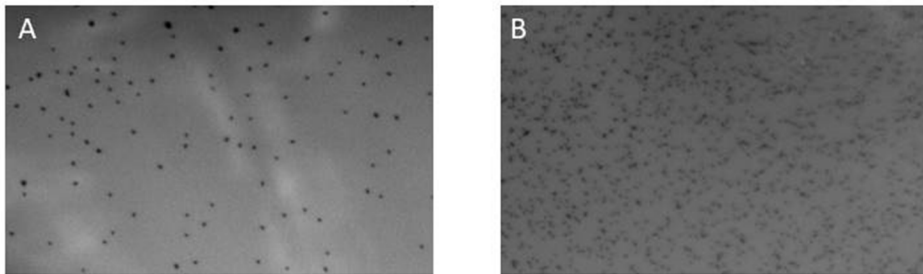
Figure 1 Optical images of deposition of *E.coli* deposited on glass(A) and on Poly L- poly L-ornithine functionalized glass(B).

The cell suspension was incubated for few minutes onto glass and finally dried prior to perform the AFM analysis. Drying of the cellular samples was carried out using a gentle nitrogen flow. It has been reported that nitrogen drying changes the surface of bacterial membrane, most likely because of the mechanical stress, although no patterns are generated *de novo* [18]. For this reason, drying of deposited cells was also performed at room temperature (RT) by solvent evaporation in order to avoid any possible morphological perturbations of the cells.

Sample fixation by means of formaldehyde or glutaraldehyde crosslinking is a method widely used in microscopy, although, only one work by Chao and Zhang, extensively analyzes the effects of different fixation methods on bacterial morphology [19] and, according to the authors, glutaraldehyde fixation preserves the tridimensional structures of the cells. For this reason I employed glutaraldehyde as crosslinking reagent for *E. coli* fixation.

The AFM characterization of the cells was carried on *E. coli* cells harvested at $OD_{600=}0,2$ and $OD_{600}=6$, representative of the exponential and stationary phase of growth, respectively.

To quantitatively evaluate the effect of the fixation methods on bacterial morphology, the width/height ratio (*W/H*) was used as an index reflecting the preservation of bacterial cell as analyzed by Chao and Zhang. For intact rod-shaped bacteria, the *W/H* ratio is close to 1 [19]. Glutaraldehyde fixation of exponential cells leads to higher and narrow cell with a volume of 1.11 ±0.07 μm^3 (Table1). The sample preparation can lead to cell edge artifact as can be observed in Figure 1 and Figure 2. These artifacts could mean a shrinkage of the cell's interior due to cytosol jellification induced by the fixative agent.

RT drying leads to the wider and lowest exponential cells with a high W/H ratio but the volume is in line with the cross-linked sample (Table1) . These data indicates that drying by solvent evaporation causes a general relaxation of cell morphology on the solid surface support (Figure 2 and Figure3).

Nitrogen drying of cells in exponential growth, determines an intermediate value of W/H ratio (Table1) and still the volume value is in line with the fixated/dried RT sample. As it can be seen from the zoomed images, the cells show wrinkles and reentrant on the surface (Figure 3). Wrinkles and reentrant could be due to fast dehydration upon the passage of the meniscus.

Table 1

| Exponential	H (µm)	W (µm)	W/H	V (µm3)
Air evaporation	0,24±0,02	1,58±0,08	6,4±0,54	0,99±0,17
glut	0,41±0,02	1,19±0,12	3,00±0,3	1,11±0,07
nitrogen	0,29±0,04	1,52±0,06	5,2±0,74	1,07±0,25
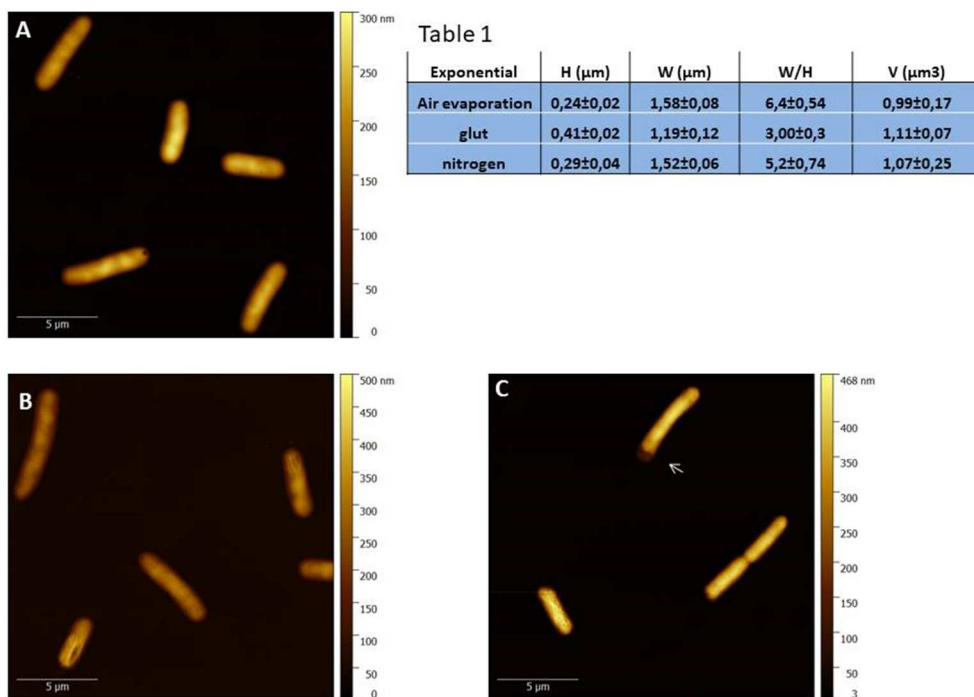
Figure 2. AFM scans at 20µm of *E. coli* cells. A) dried by RT evaporation; B) dried by nitrogen flow and C) fixed with 2.5% glutaraldehyde (arrow indicating an edge artifact).
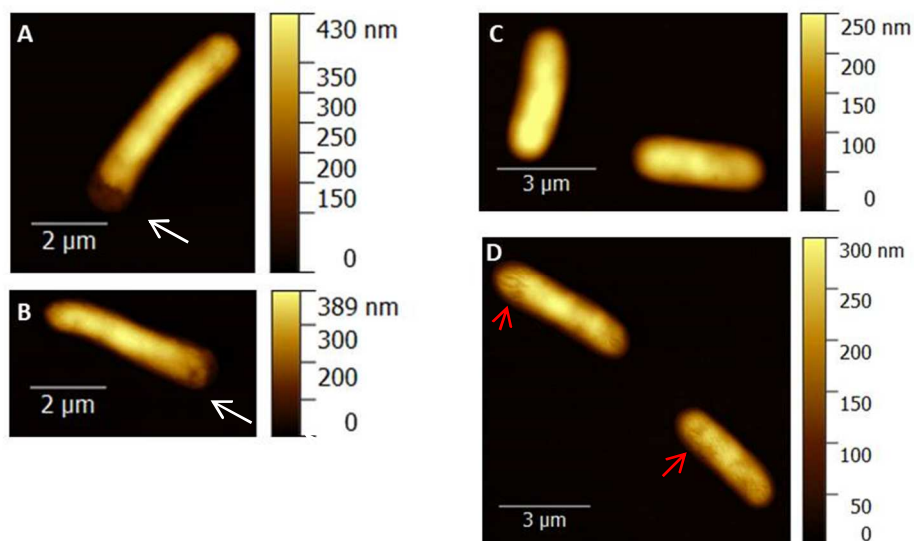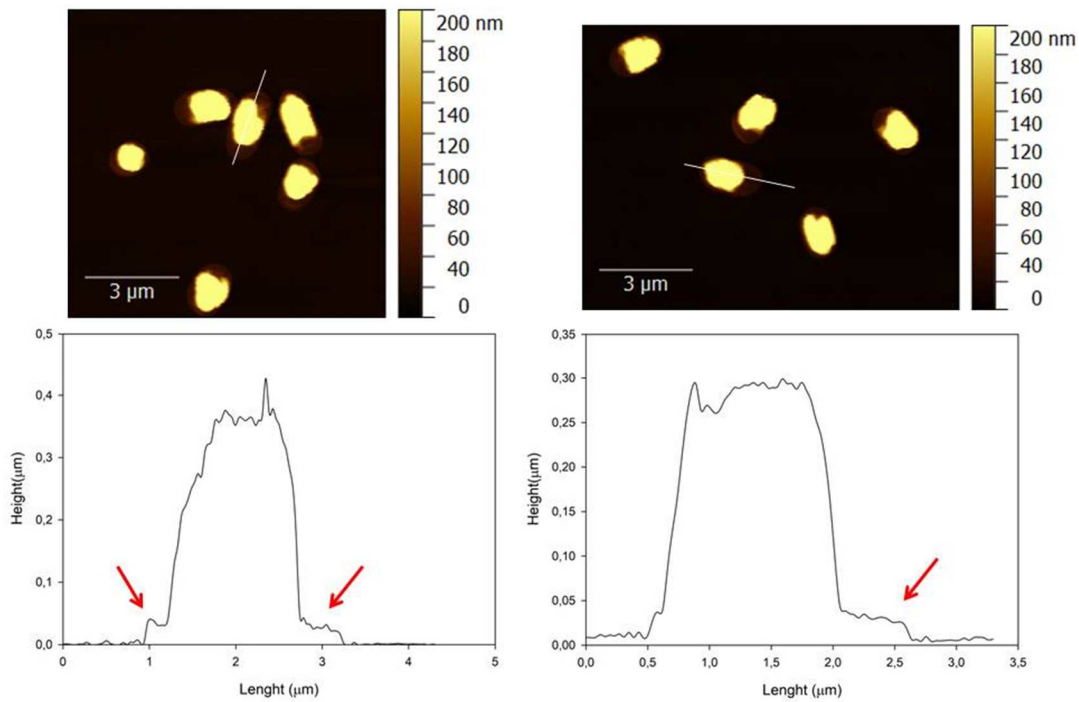

Figure 3. Representative images magnification of different cells. A-B) fixed with 2.5% glutaraldehyde (white arrow indicating an edge artifact).; C)) dried by RT evaporation D) dried by nitrogen flow (red arrow indicating surface wrinkle).

Cells in stationary phase showed the highest degree of morphological differences due to different types of sample preparation (Table 2).

RT drying by solvent evaporation reveals an homogenous behavior of the bacterial population (Figure 3) in which a compact structure appears in the center of the cell, surrounded by a flat region with a height of about 50 nm, most probably composed by peptidoglycan and plasma membrane (Figure 4).

In contrast both preparations with glutaraldehyde and nitrogen drying show a blob on the side of the cell (Figure 4) from which, in the nitrogen-dried sample, a central ridge forms. The fact that some fixed cells show a more uniform cell morphology (white arrows) makes me hypothesize that the fixing of cells in stationary phase with the protocol used for cells in exponential growth, is not sufficient to carry out a complete fixing of the bacterial structures, perhaps due to the marked biological rearrangements following the entry into the stationary phase.

Nitrogen drying determines an intermediate value of the W/H ratio for exponential cells while a central ridge appears in stationary phase cells (Figures 4B and 6). These cells show only a slight increase in width but show a much smaller volume than that measured in cells dried at RT or cross-linked. These observations suggested that nitrogen drying can impact on the cell morphology. However, such topological perturbation can be representative of an internal structures of the cells. As it can been seen in Figure 6, nitrogen drying can reveal dividing cells, not detected with the other preparation methods.
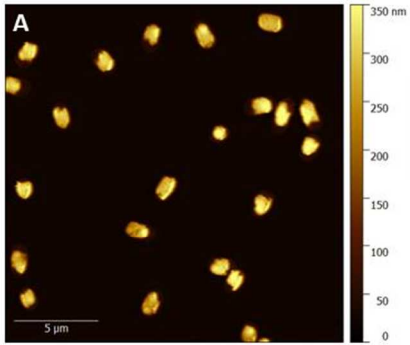
Table 2

Stazionary	H (μm)	W (μm)	W/H	V (μm3)
Air evaporation	0,28±0,04	1,17±0,06	4,12±0,52	0,33±0,05
Glut	0,36±0,02	1,10±0,09	3,00±0,3	0,29±0,06
nitrogen	0,28±0,03	1,2±0,05	4,4±0,35	0,25±0,06
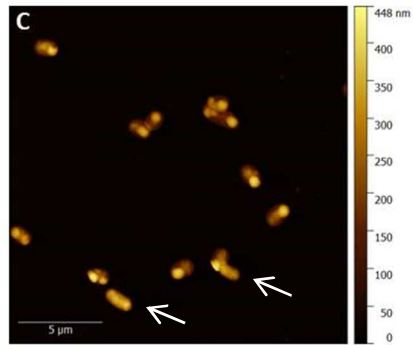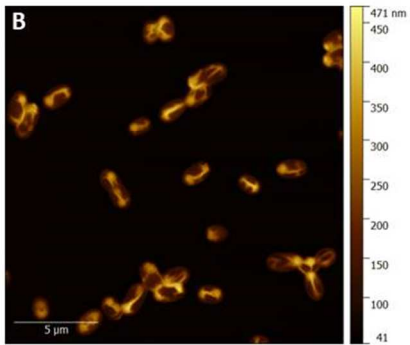
Figure 4. AFM scans at 20μm of *E. coli* cells. A) dried by RT evaporation; B) dried by nitrogen flow and C) fixed with 2.5% glutaraldehyde (arrow indicating a complete fixed cell).

Figure 5. Representative AFM images magnification of stationary phase cells after RT evaporation drying (top).Extracted profile from two cells displaying a flat structure of 50 nm height on the cellular ends (red arrow)
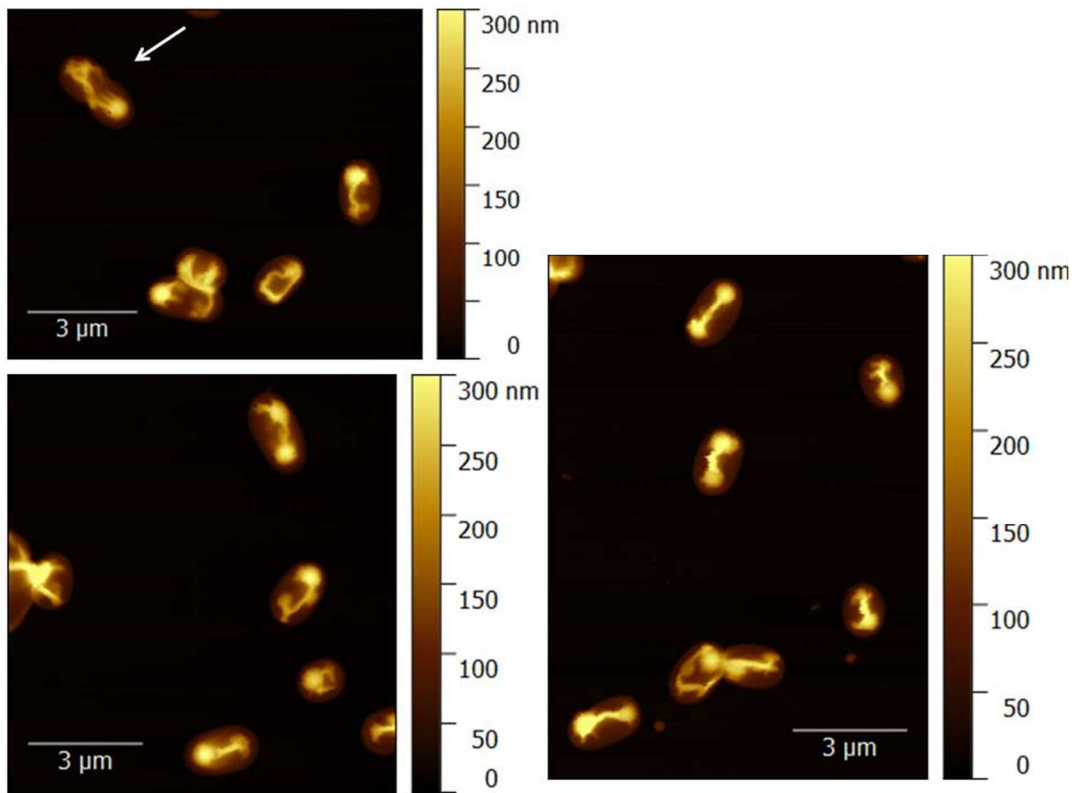
Figure 6. Representative AFM images magnification of stationary phase cells after nitrogen drying. It can see the majority of cells exhibits a central crest and morphological characteristics absent in other preparations (white arrow).

Because the preparation of cells in stationary phase often leads to samples characterized by abundant extracellular matrix difficult to image by AFM, I focused my attention on cells harvested at OD_{600}=3 (early stationary phase of growth) to better understand whether the different cellular morphologies observed after nitrogen drying were artifacts or representative features of a particular morphological state.

AFM-FM analysis of cells in exponential growth

To evaluate whether the formation of the ridges is due to an artifact caused by the drying or due to a particular arrangements of the bacteria internal components, I developed and employed a combined AFM-FM approach. The first candidate that can determine these morphological behaviors is the nucleoid.

Through the analysis of hybrid images, I tried to verify whether if the central ridge correspond to the nucleoid fluorescence signal..

AFM and fluorescence images were collected on both exponential and stationary phase cells. The AFM-FM analysis were performed on cross-linked and uncross-linked cell preparations and after RT drying by means of a nitrogen flow and solvent evaporation . Images collected on cells dried by water evaporation were characterized by a smooth surface (roughness 0,56 ± 0,15nm) without any particular complex morphology, in line with the cell morphology previously described (Figures 7, 8 and 9). Fluorescence images reveal the presence of numerous structures (Figure 7B) in line with literature reports showing a complex nucleoid organization in a rapidly growing state. Three cells of different lengths (Figure 10, 11) were characterized by a particular nucleoid organization, very similar to that shown in reference 98. These three cells may be in a different phase of growth. The smaller cell shows a bilobate nucleoid structure, whereas the central cell appears longer and the nucleoid seems more extended, as if it is in the segregation phase. Finally, the third cell has two fully separate nucleoids and shows a furrow that divides the cell into two compartments (Figure 10, 11).

In this image there is no correlation between surface topography and underlying location of the nucleoid (Figure 11).
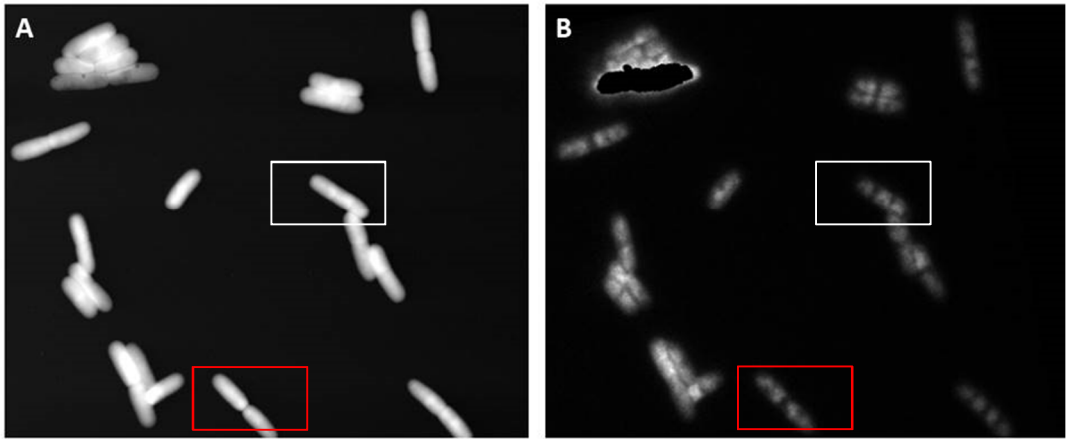
Figure7. AFM (A) and FM(B) images of the same area after evaporation of excess solution at RT (OD_{600}=0,25).
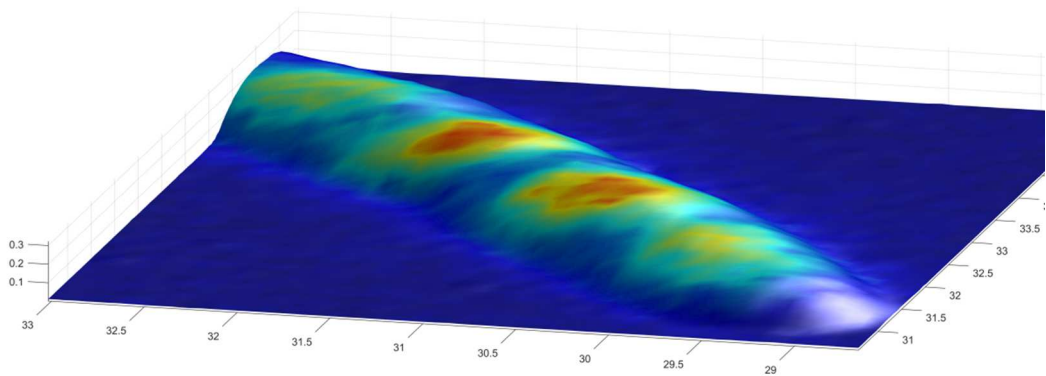
Figure 8. Overlay of the FM on the tridimensional AFM image (withe box in figure 7). As it can be seen the region with the high fluorescence (red) is characterized by uniform bacterial morphology. The values on Cartesian axes are expressed in micrometers .
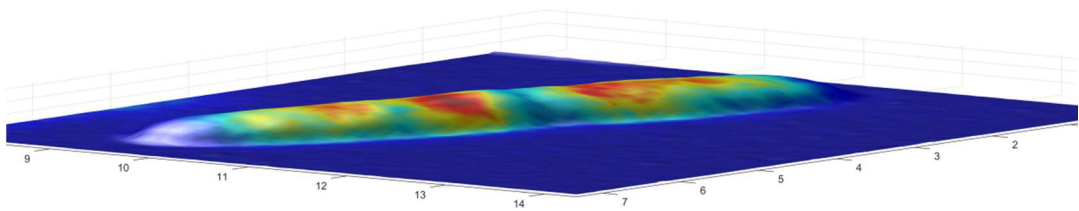
Figure 9. Overlay of the FM on the tridimensional AFM image (of the red box in figure 7). The region with the high fluorescence signal (red) is characterized by uniform bacterial topography. The values on Cartesian axes are expressed in micrometers.

54
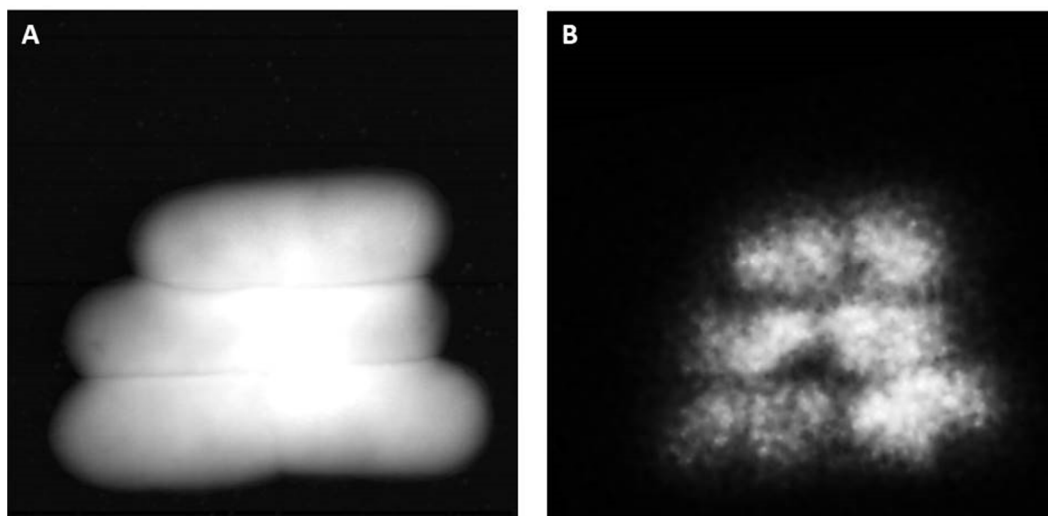
Figure 10. AFM (A) and FM(B) images of the same area depicting three different cells (OD$_{600}$=0,25) after evaporation of excess solution at RT.
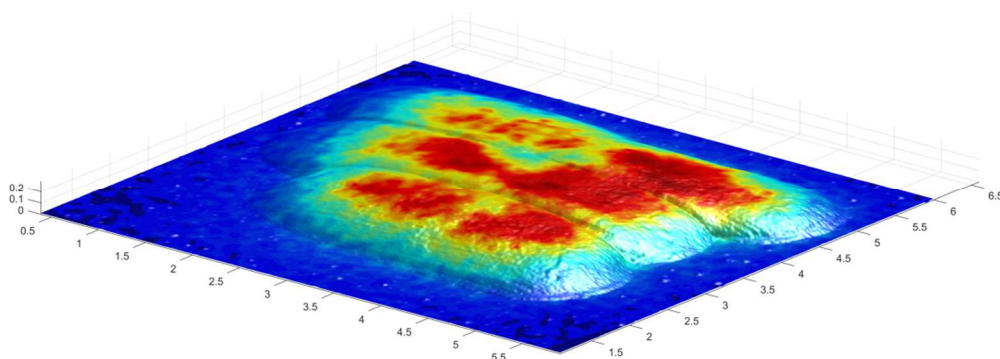
Figure 11 Overlay of the FM on the tridimensional AFM image of three cell in different time of chromosome segregation in exponential phase and dried by evaporation at RT. The values on Cartesian axes are expressed in micrometers.

Images collected of the cross-linked sample shows end defects and a wrinkled appearance (Figure 12-16); roughness analysis reveals an increase in roughness compared to RT drying at a value of 1.49 ± 0.19 nm.

In addition, fluorescence images are characterized by a strong signal at the edges (12B, 14B) whereas other cells do not emit as strongly (Figure 12B, 14B). These forms could be caused by the chemical fixation or by autofluorescence of glutaraldehyde after reacting with the proteins .
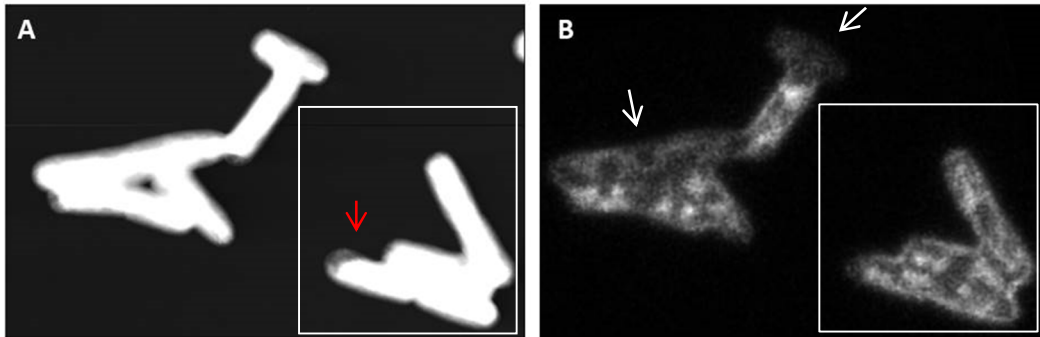
Figure 12. AFM (A) and FM(B) images of the same area of cell fixed with glutaraldehyde (OD_{600}=0,25). Fixation leads to edge artifact as indicated by the red arrow. FM image display defects such as edge fluorescence and difficult to stain cell (white arrow).
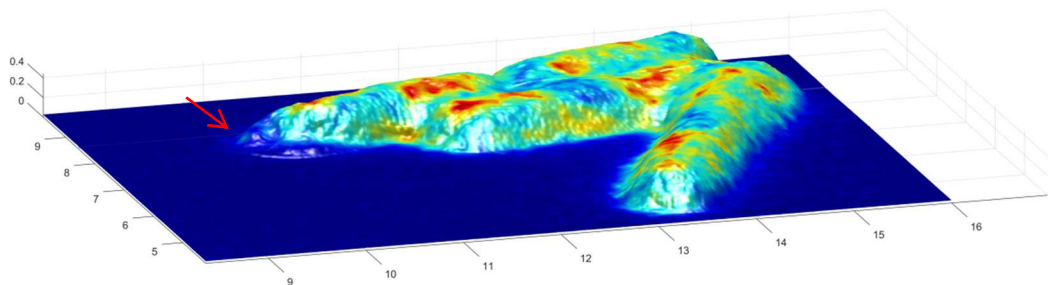
Figure 13. Overlay of the FM on the tridimensional AFM image (of the white box in figure 12). The surface is quite wrinkled and display edge artifact of fixation (red arrow). The values on Cartesian axes are expressed in micrometers.
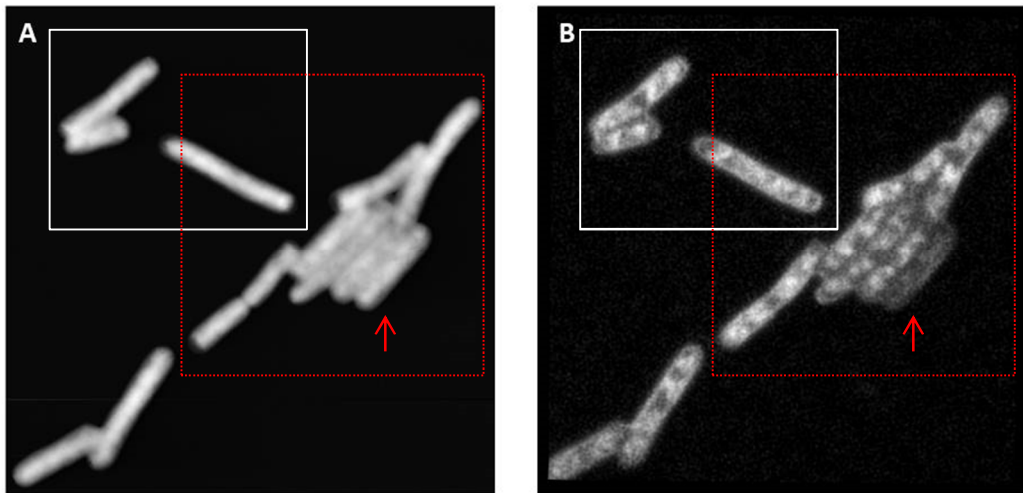
Figure 14. Second experiment of cell fixed with glutaraldehyde (OD_{600}=0,25). Also in this experiment FM image display defects such as edge fluorescence and difficult to stain cell (red arrow).
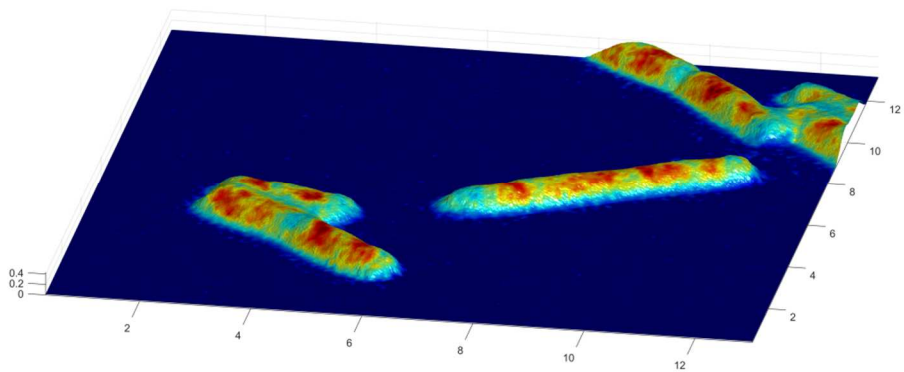
Figure 15 Overlay of the FM on the tridimensional AFM image (of the white box in figure 14). The surface is quite wrinkled and display edge artifact of fixation (red arrow). The values on Cartesian axes are expressed in micrometers.
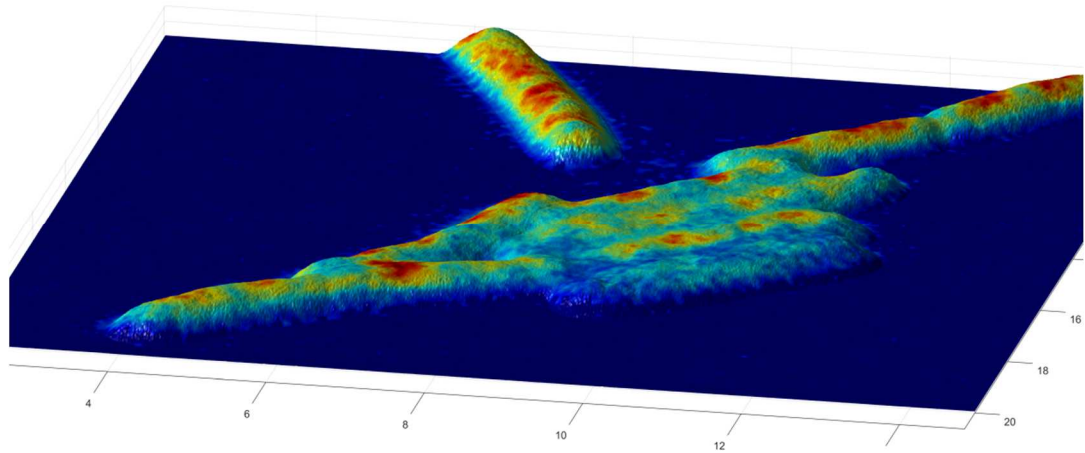
Figure 16 Overlay of the FM on the tridimensional AFM image (of the white box in figure 14). The surface is quite wrinkled and display edge artifact of fixation (red arrow).

Cells dried with a nitrogen flux show the largest roughness value: 2.33±0.4. Fluorescence images resemble the RT water evaporation situation with good image quality (17B, 19B). In some cells the nucleoid is positioned in a reentrant of about 50nm (Figure 18,20). This reentrant could be a reflection of the phase separation between the nucleoid and cytosol [20] that could be enhanced by this particular sample preparation.
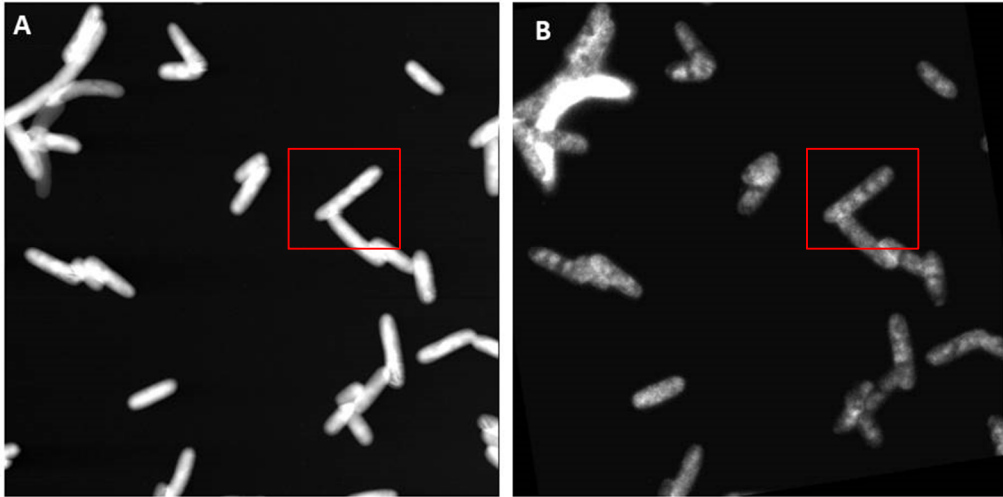
Figure 17. AFM (A) and FM(B) images of the same area of nitrogen dried cell (OD_{600}=0,25). The FM image resemble the evaporation sample and multiple nucleoid structure can clearly be seen.
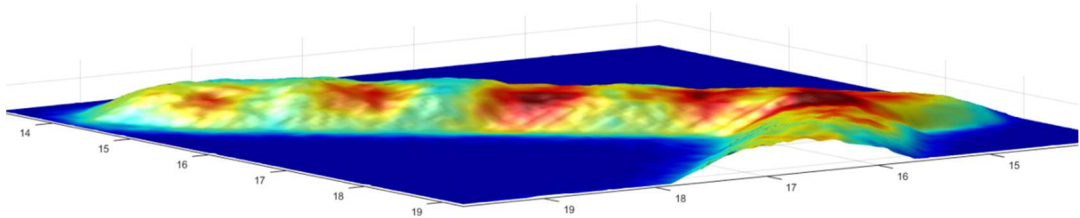
Figure 18. Overlay of the FM on the tridimensional AFM image (of the red box in figure 17). The surface characterized by surface hollows corresponding to area of maximal fluorescence intensity. The values on Cartesian axes are expressed in micrometers.
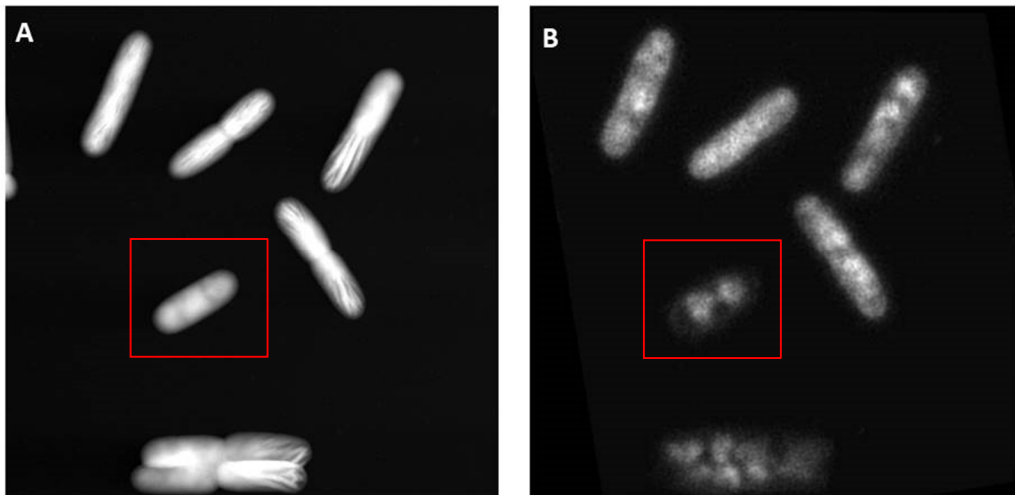
Figure 19. Second experiment of nitrogen dried cells (OD_{600}=0,25). AFM (A) and FM(B) images of the same area.
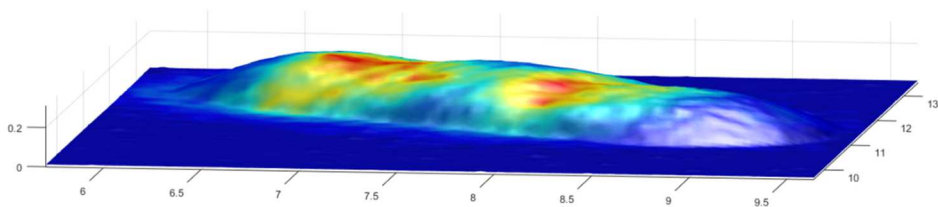
Figure 20. Overlay of the FM on the tridimensional AFM image (of the red box in figure 19). The surface characterized by surface hollows corresponding to area of maximal fluorescence intensity. The values on Cartesian axes are expressed in micrometers.

AFM-FM analysis of Early-Stationary phase cell

The nitrogen-dried sample shows the formation of central ridges with a swelling at the extremities (Figure 21-23). The ridges show a good co-localization with the fluorescence signal, thus confirming the hypothesis that they could reflect the shape of the nucleoid (Figure 22,23).

The cross-linked cells and cells dried by water evaporation (Figure 24-28), did not show any particular structure with respect to the cells harvested at optical density (600nm) of 6. In contrast to nitrogen dried sample, FM images of fixed samples display a uniform diffusion of the signal, while the fluorescence signal of RT evaporated sample reach the highest value in a region positioned at mid-cell (Figure 27,28).

The ridges couldn't be the actual morphology of the nucleoid, since the RT evaporated sample nor the crosslink sample displays a fluorescent signal similar to the nitrogen dry . Thus the ridge could reflect a softer morphological state which can be remodeled by the effect of the drying meniscus or being an artifact of nitrogen drying.
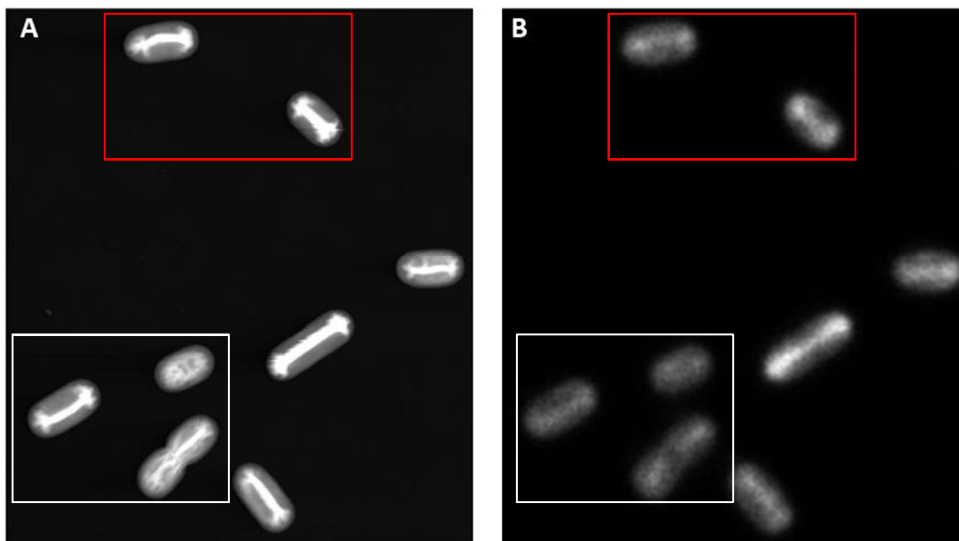
Figure 21. AFM (A) and FM(B) images of the same area of nitrogen dried cell (OD_{600}=3). There is quite similarity between the ridge shape of bacterial cell and the specific signal in the FM image .
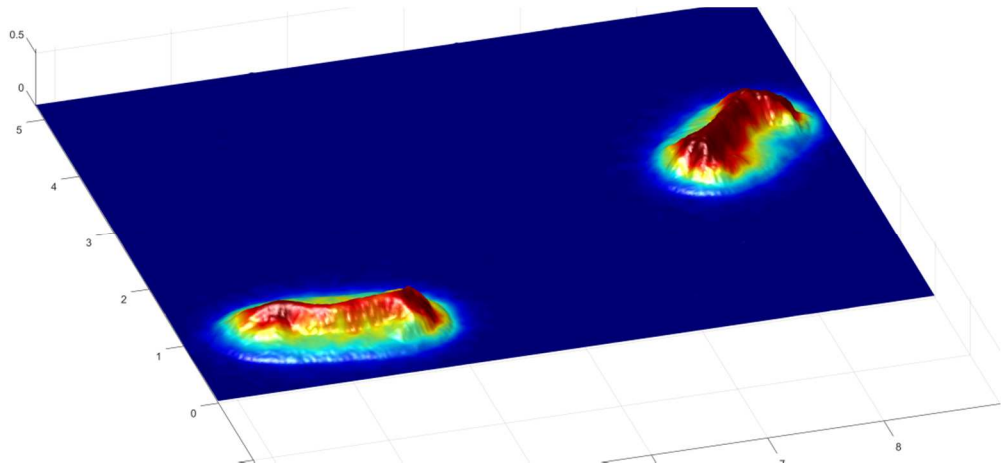
Figure 22. Overlay of the FM on the tridimensional AFM image (of the red box in figure 21).In this image it can be appreciate the overlay between the FM signal and the ridge profile. The values on Cartesian axes are expressed in micrometers.
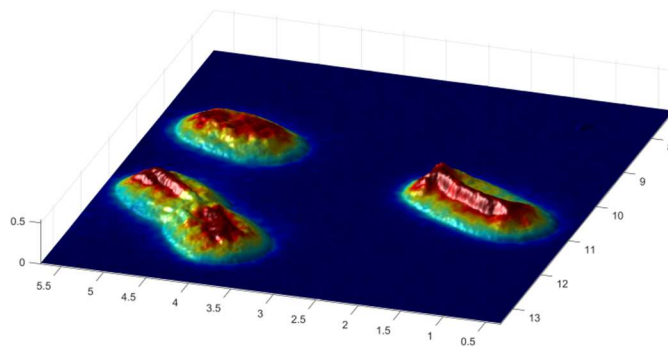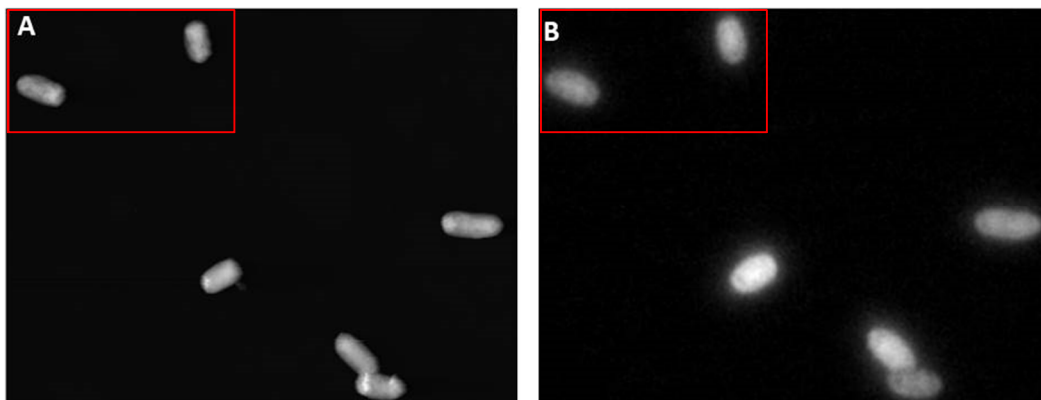

Figure 23. Overlay of the FM on the tridimensional AFM image (of the white box in figure 21). Also in this figure it can be appreciate the overlay between the FM signal and the ridge profile. The values on Cartesian axes are expressed in micrometers.

Figure 24. AFM (A) and FM(B) images of the same area of fixed cell (OD_{600}=3). There is quite similarity between the morphology of bacterial cells and the shape of the FM image but no structure can be identified.
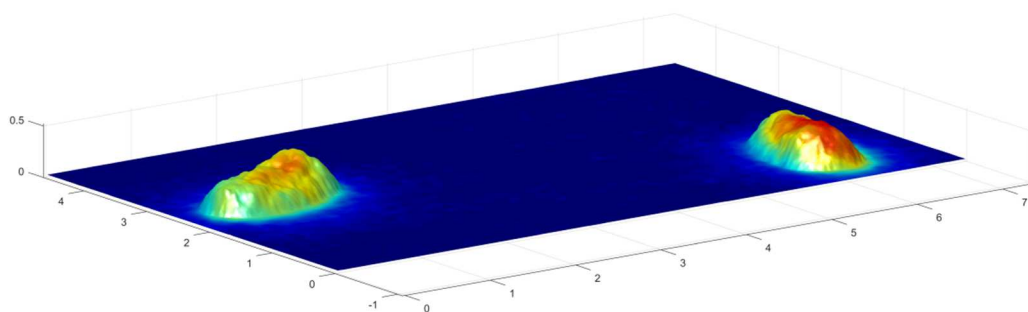

Figure 25. Overlay of the FM on the tridimensional AFM image (of the red box in figure 24). The values on Cartesian axes are expressed in micrometers.
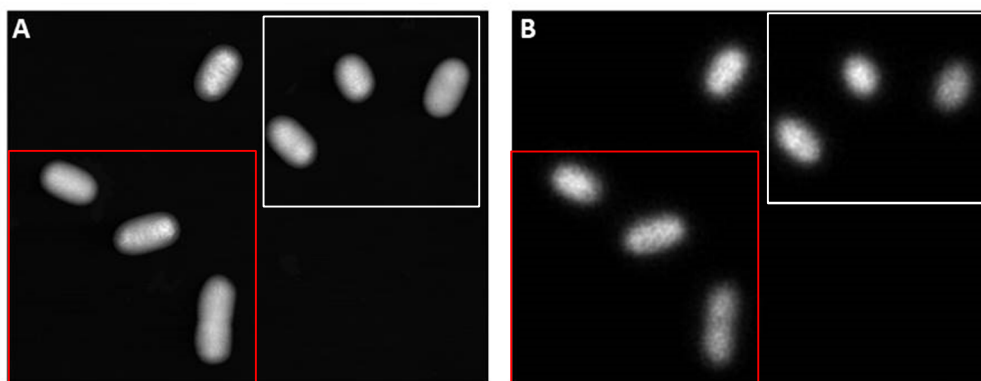

Figure 26. AFM (A) and FM(B) images of the same area of cell dried by RT evaporation (OD_{600}=3).
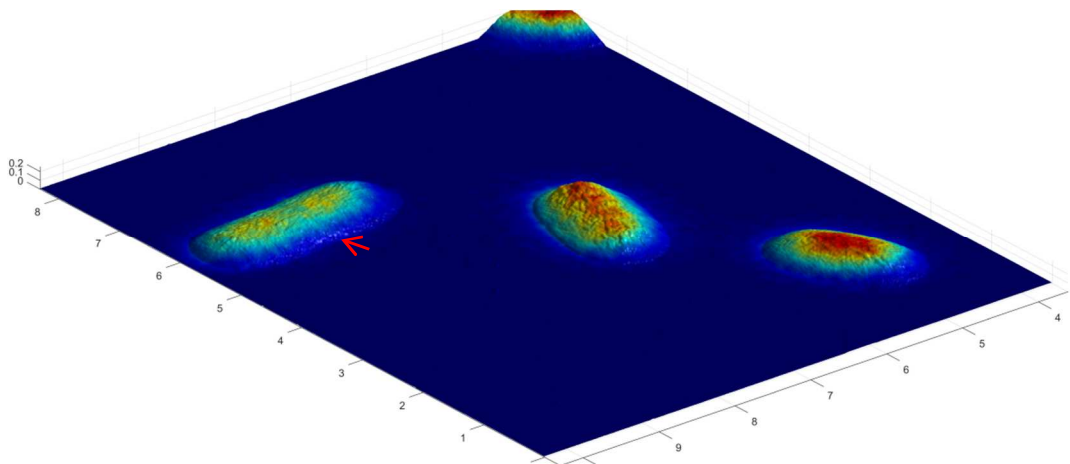
63

Figure 27. Overlay of the FM on the tridimensional AFM image (of the red box in figure 26). Displaying the FM images in jet colormap, it can be seen that the fluorescence reach the high value in a compact region positioned at midcell. AFM image display a septum like structure (red arrow) but it isn't defined like the one identified in Figure21. The values on Cartesian axes are expressed in micrometers.
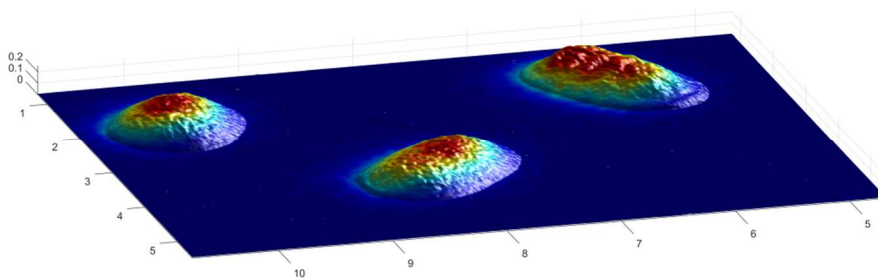

Figure 28. Overlay of the FM on the tridimensional AFM image (of the white box in figure 26). Displaying the FM images in jet colormap, it can be seen that the fluorescence reach the high value in a compact region positioned at midcell. The values on Cartesian axes are expressed in micrometers.

64

DAPI perturbation

I have used the disturbing effect of DAPI to assess whether the strength of the drying meniscus has sufficient force to induce ridge formation or whether it reflects a more softer state of the cell. In literature it is reported that DAPI is capable of causing an expansion of the nucleoid in living cells [21].

Therefore, if nitrogen drying is the only factor responsible of ridges formation there will be the appearance of crests even exposing the cells to DAPI for a prolonged period. On the contrary, if cells characterized by central ridges are not formed, it will mean that the meniscus does not have sufficient strength to cause ridge formation by itself .

Incubating cells collected at OD_{600} of 3 with 20 μg/ml of DAPI, the overall morphology reflect the cell discussed above (figure 29-32). This set of recorded images also shows a strong co-localization of the ridge with the DAPI signals (Figure 30, 32). It was also possible to observe cells with a particular morphology . Figure 31 and 32 show two cells in which the fluorescence signal has a gap in the center where the topography shows a depression that could be the cell division septum (white arrow). After 30 minutes incubation with DAPI it was possible to observe the disappearance of the ridges (Figure 33, 34), suggesting that the ridges are not an artifact of the nitrogen drying procedure . Therefore, the ridges observed after nitrogen drying represent the footprint of the nucleoid structure when the cell is deflated by the nitrogen flow.
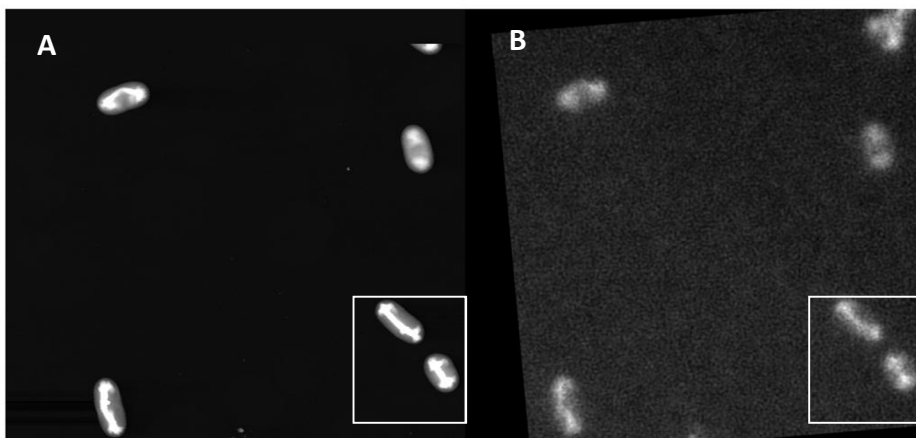
Figure 29. AFM (A) and FM(B) images of the same area of nitrogen dried cell (OD_{600}=3) after 2 minutes of incubation with DAPI (20µg/mL).
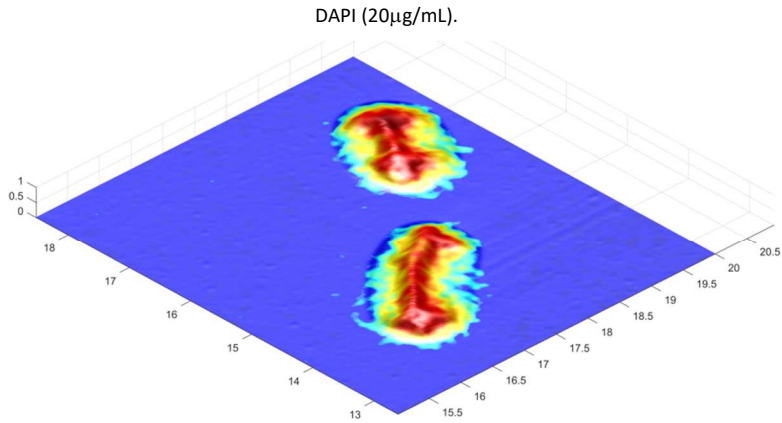

Figure 30. Overlay of the FM on the tridimensional AFM image (of the white box in figure 29).In this image it can be appreciate the overlay between the FM signal and the ridge profile. The values on Cartesian axes are expressed in micrometers.
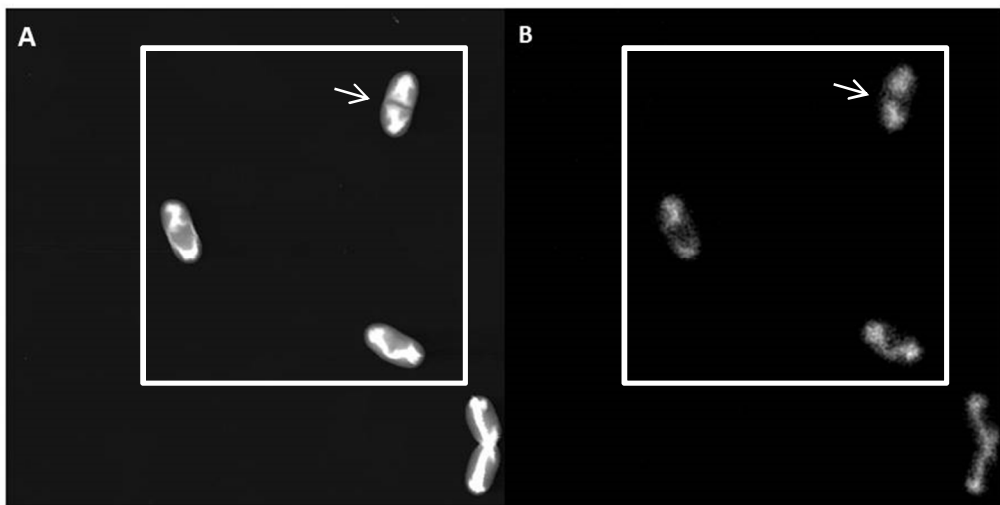

Figure 31. AFM (A) and FM(B) images of a second area area of nitrogen dried cell (OD_{600}=3) after 2 minutes of incubation with DAPI (20 µg/mL). the white arrow is indicating the central depression.
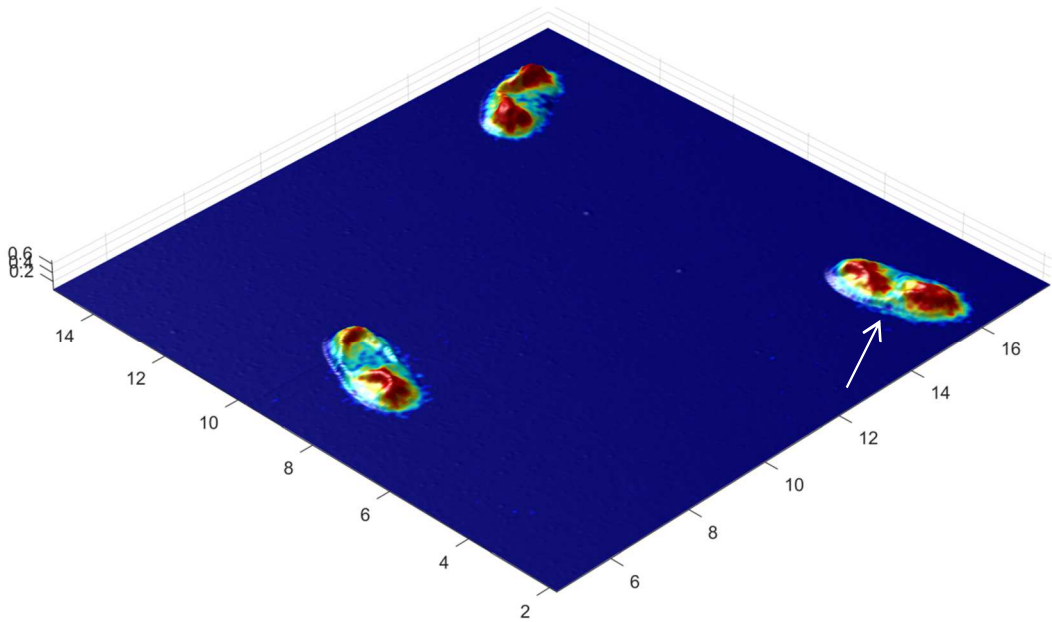
Figure 32 Overlay of the FM on the tridimensional AFM image (of the white box in figure 31). The values on Cartesian axes are expressed in micrometers.

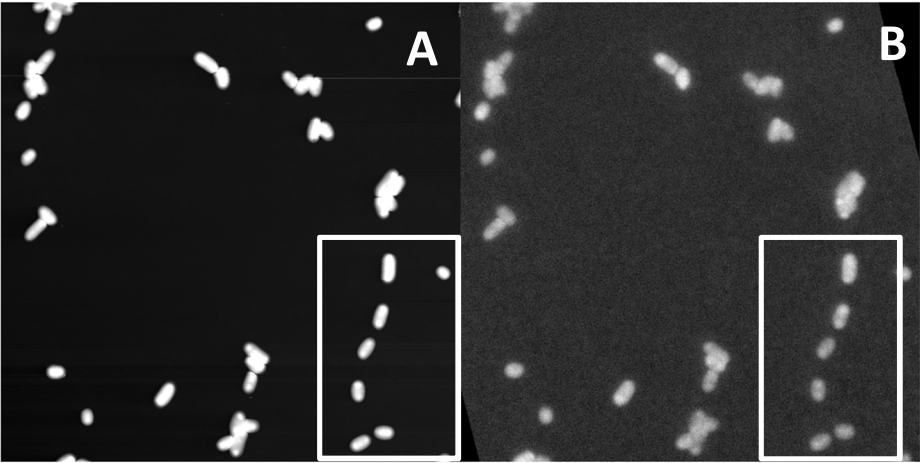**Figure 33.** AFM (A) and FM(B) images of the same area of nitrogen dried cell (OD_{600}=3) after 30 minutes of incubation with DAPI (20μg/mL) leading to ridge disappearance. AFM image has a resolution of 39nm /pixel.
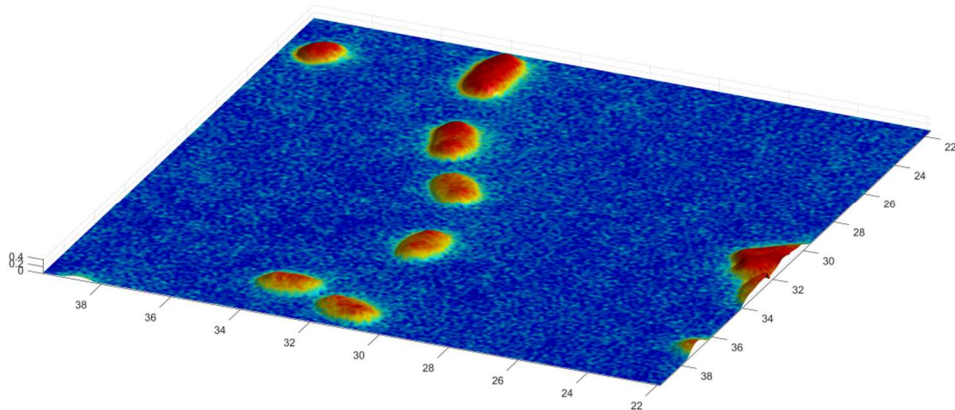
Figure 34. Overlay of the FM on the tridimensional AFM image (of the white box in figure 33) with no meniscus-induced ridge formation. The values on Cartesian axes are expressed in micrometers.

Conclusion

Through the development of the AFM FM coupled approach, it has been possible to link the topographic structure of the cell with the organization of the inner nucleoid without subjecting the cells to invasive lysis procedures.

Significant and reproducible differences in nucleoid organization have been found in relation to the different stages of the bacterial growth.

This organization is also reflected in the morphology of the bacterium. In the exponential phase, the larger amount of genomic material detected by fluorescence prevents the cell from being extensively deformed when subjected to the nitrogen drying procedure. In fact, with this preparation method, small superficial depressions are found where the fluorescence signal indicates the presence of genetic material.

On the contrary, in the stationary phase, the soft nature of the genome and the lower amount of genomic material per cell, makes the cells to undertake a marked morphological change after drying with nitrogen flow, resulting in the formation of ridges. This morphology does not only depend on the drying procedure but reflects the physiological state of the nucleoid. In fact, by altering the nucleoid organization with DAPI, it possible to avoid the formation of ridges.

Materials and Methods

Growth Conditions and sample preparation

I used *Escherichia coli* K12 MG1655 since is the most studied *E.coli* strain. The cultures started with an overnight inoculum, from steb, in LB liquid(10 g of tryptone, 5 g of yeast extract, 10 g of NaCl, and 1 liter of distilled water; adjust the pH to 7.0 with 1 N NaOH). In the morning the liquid culture is diluted 1000 times for an initial OD of the new growth of 0,006.

For the exponential phase, a volume of 30 mL of cells was collected at an OD600 of 0.25 mL; for the early stationary phase, 2 mL of cells were collected at an OD600 3 and for the

stationary, 1 mL was collected at an OD600 of 7. Cells were washed 3 times with 2 mL of Phosphate Saline Buffer (PBS) and collected at 13K rpm for 1 minute, then re-suspended in 2 mL of PBS.

For crosslinking gluteraldehyde is added to a final concentration of 2.5% and the reaction is left in stirring for 1 H. At the end, cells were washed 2 times with PBS 1X before the staining phase. For cell staining 100 μl of washed cells were incubated with 10μg/mL of DAPI (4',6-diamidino-2-phenylindole) for 5 minutes.

In the case of nucleoid perturbation, they are incubated with 20 μg/mL of DAPI for 5 minutes and 30 minutes. The perturbation was conducted in three independent experiments.

After incubation, the cell volume was carried to 1 mL with PBS 1X and washed twice with PBS 1Xpellets after the last centrifuge is re-suspended in 50μL of PBS 1X.

Microscopy

For AFM-FM microscopy, the cells are deposited on the object cover slide. the slide is functionalized with 50μL of Poly L-Orithine 0,01%(Sigma) for 1 minute. Poly L-Orithine drop is dried with a gentle flow of nitrogen.

A volume of 25 μL of bacteria is deposited on the functionalized slide for 30 seconds, and successively the excess solution is washed with milliQ water. depending on the preparation procedure, the sample is left to dry by evaporation at RT or dried with a gently nitrogen stream (also the fixed sample is dried with nitrogen stream).

Nitrogen drying is carried out meticulously by tilting the slide at about 45 ° downward and nitrogen flow is directed in one direction on the residual drop of the slide. The drop is carefully swept through the formation of the meniscus.

The position with greater opacity is marked in such a way as to generate references to find the cells with the two microscopes**.**

Fluorescence microscopy is carried out with a Nikon Eclipse E600 equipped with a 100X immersion oil lens and with a mercury lamp.

The image of the cells is first recorded in bright-field and then the image of the same optic field is recorded with a DAPI specific filter and an exposition time of 400 to 600 ms.

AFM microscopy is carried out through an AFM Park XE-100 integrated with a 60X optical camera with which the AFM scan can be centered in an area previously collected through the Nikon Eclipse microscope.

A NCHR tip with a nominal tip radius of less than 10 nm has been used for experiments and AFM intermittent mode was choose**.

Image processing

Brightfield and fluorescence images are processed through the Cell Profiler program.

The images are imported through the' LoadSingleImage' function and then cropped in the area with the cells recorded under the AFM microscope.

The images are then converted to 8bit using the RGB channel summing method.

To even out the lighting, an illumination function is calculated (using the Regular option) that is used to correct uneven illumination/lighting/shading or to reduce uneven background in images, through a polynomial fitting that is applied by division to the image.

The brightfield image of bacteria is mathematically inverted (via the' ImageMath' module) if the pixels inside the bacterial cells have lower background values (this procedure is necessary for the subsequent MatLab analysis to record AFM and fluorescence images together). For fluorescence images, after correction with the lighting function, a Global Tresholding module is applied using the three class Otsu method (background) to identify a threshold value to be subtracted from the image. This process removes the background signal.

Subsequently the operation of subtracting the threshold value the image is scaled (module 'rescaleImage').

The image is then exported as a Tif file and is ready for image registration.

AFM image processing

The AFM image is instead processed using the Gwyddion software.

The first procedure to be performed on an AFM image is flatten, which levels the image. For all the images, I have made a flatten per line using the median method. Once the minimum value has been leveled , it is reduced to zero and the image is exported in Gwiddion format.

For the analysis of width and height parameters, I used the profile extraction Toolkit, which was then analyzed via Sigmaplot software.

The roughness value was extracted from images with the same spatial resolution by drawing a 1 pixel thick line long 1μm for 10 cell of each sample, along the longitudinal axis of the cells and using a cut-off of 0.2 and an exact type of interpolation of the values.

MATLAB Image registration

In order to obtain a three-dimensional image with actual topography data, on which to plot the fluorescence image, it is necessary to rescale and align the fluorescence image with the size of the AFM image.

The bright-field image and AFM image were used to calculate the geometric transformation function.

AFM parameters were imported into MATLAB using the script 'readgwyddionchannel'. developed by Lennart Fricke.

Through this script a structure containing information about the size of the image in pixels, in microns and a matrix with the height values of the sample was generated. To be able to proceed with image registration, it was necessary to convert the values of the height matrix into uint8.To register the image, I used the Imageregistration app integrated in the 2017 MATLAB realise only. Once the two images have been imported

into the application environment, you can choose the feature detection method to be used for alignment.

For all images, the Speeded-Up Robust Features (SURF) algorithm to find blob features has been used in both images (Figure 35).
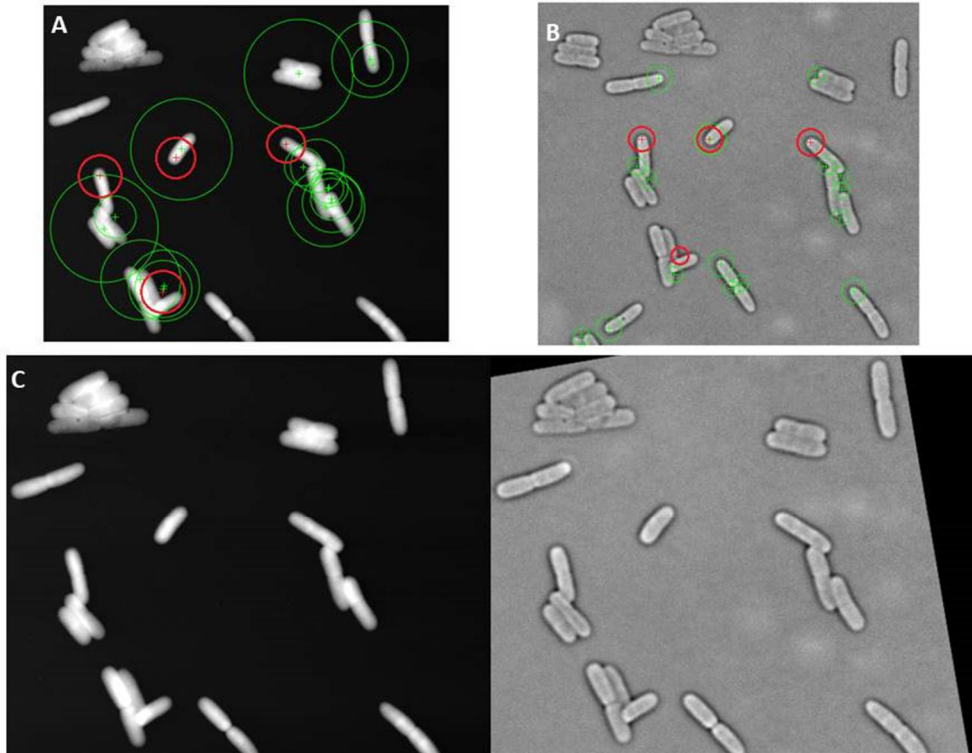

Figure 35. A-B) Best 20 feature recognized by the SURFF algorithm displayed as green circle. Among this feature the ones that are registered with the same geometrical transformation are displayed as red circle. Application of the estimated transformation, using only the red circle, to the bright-field mage

The application windows also has a check on the number of identified features and the goodness of alignment. By means of attempts it is possible to select the features that are present in both images and proceed to align them through a transformation for' similarity'. (this transformations include isotropic scaling, rotation, and translation operation).

It's possible to export the transformation function, the positions of the aligned features and the registered image.

To improve the image registration after the first step with the SURF algorithm, the registered image is imported back into the application and a second alignment is carried out through the multimodal intensity algorithm of the images, selecting the geometric option, which aligns the geometric centers (Figure 36).
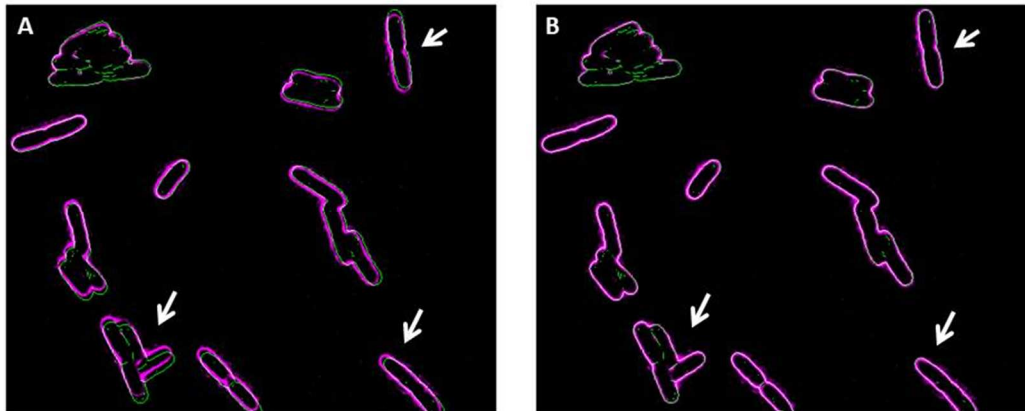

Figure 36. Example of the different degree of alignment between the edged image showed in figure 35 (AFM in green and bright-field in magenta) the use of the SURFF algorithm only (A) and the subsequent realignment process with the multimodal intensity algorithm (white arrow indicates region of alignment improvement of the images).

At this point the two transformations functions are applied to the fluorescence image.

The size of the matrix, containing the height values, is then converted from the number of pixels to the physical length (expressed for all three Cartesian axes in micrometers).

the AFM image is plotted with the surf function calling the registered fluorescence image as a colormap. For all the images the colormap jet was selected in order to better visualize the intensity variation .

MATLAB command for image visualization :
```
figure,surf(XAFM,YAFM,ZAFM,recoveredfluoimage,'EdgeColor','none','L
```

```
ineStyle','none','FaceColor','interp','EdgeLighting','none','FaceLi
ghting','gouraud');
```

MATLAB script for matrix pixel-real dimension conversion :

```
D = readgwychannel(fileAFM,0);

xreal = getfield(D, 'xreal');

yreal = getfield(D, 'yreal');

Xres=getfield(D,'xres');

Yres=getfield(D,'yres');

xrealmicron=xreal*1e6;

yrealmicron=yreal*1e6;

Dsurf=surf(D.data);

Xdata=Dsurf.XData;

Ydata=Dsurf.YData;

Zdata=Dsurf.ZData;

X = double(Xres);

Y = double(Yres);

Xreal=xrealmicron*Xdata./X;

Yreal=yrealmicron*Ydata./Y;

Zreal=Zdata*1000000;

figure,surf(Xreal,Yreal,Zreal,recfluo,'EdgeColor','none','LineStyle
','none','FaceColor','interp','EdgeLighting','none','FaceLighting',
'gouraud');
```

Bibliography

1. Weidel W, Pelzer H. Bagshaped Macromolecules—A New Outlook on Bacterial Cell Walls. In: *Advances in Enzymology and Related Areas of Molecular Biology*. John Wiley & Sons, Inc.; 1964:193-232. doi:10.1002/9780470122716.ch5.

2. Yao X, Jericho M, Pink D, Beveridge T. Thickness and Elasticity of Gram-Negative Murein Sacculi Measured by Atomic Force Microscopy Thickness and Elasticity of Gram-Negative Murein Sacculi Measured by Atomic Force Microscopy. 1999;181(22):6865-6875.

3. van Teeseling MCF, de Pedro MA, Cava F. Determinants of bacterial morphology: From fundamentals to possibilities for antimicrobial targeting. *Front Microbiol*. 2017;8(JUL):1-18. doi:10.3389/fmicb.2017.01264.

4. Madabhushi R, Marians KJ. Actin Homologue MreB Affects Chromosome Segregation by Regulating Topoisomerase IV in Escherichia coli. 2013;70(4):646-656. doi:10.1002/ana.22528.Toll-like.

5. Kruse T, Møeller-Jensen J, Løbner-Olesen A, Gerdes K. Dysfunctional MreB inhibits chromosome segregation in Escherichia coli. *EMBO J*. 2003;22(19):5283-5292. doi:10.1093/emboj/cdg504.

6. Wang JD, Levin PA. Metabolism, cell growth and the bacterial cell cycle. *Nat Rev Microbiol*. 2009;7(11):822-827. doi:10.1038/nrmicro2202.

7. Adams DW, Wu LJ, Errington J. Cell cycle regulation by the bacterial nucleoid. *Curr Opin Microbiol*. 2014;22:94-101. doi:10.1016/j.mib.2014.09.020.

8. Espéli O, Borne R, Dupaigne P, et al. A MatP-divisome interaction coordinates chromosome segregation with cell division in *E. coli*. *EMBO J*. 2012;31(14):3198-3211. doi:10.1038/emboj.2012.128.

9. Donachie WD, Blakely GW. Coupling the initiation of chromosome replication to cell size in Escherichia coli. *Curr Opin Microbiol*. 2003;6(2):146-150. doi:10.1016/S1369-5274(03)00026-2.

10. Zaritsky A. Cell-Shape Homeostasis in Escherichia coli Is Driven by Growth, Division, and Nucleoid Complexity. *Biophys J*. 2015;109(2):178-181. doi:10.1016/j.bpj.2015.06.026.

11. Brandi G, Fiorani M, Pierotti C, Albano a, Cattabeni F, Cantoni O. Morphological changes in Escherichia coli cells exposed to low or high concentrations of hydrogen peroxide. *Microbiol Immunol*. 1989;33(12):991-1000.

12. Sezonov G, Joseleau-Petit D, D'Ari R. Escherichia coli physiology in Luria-Bertani broth. *J Bacteriol*. 2007;189(23):8746-8749. doi:10.1128/JB.01368-07.

13. Lange R, Hengge-Aronis R. Identification of a central regulator of stationary phase gene

expression in Escherichia coli. *Molec Microbiol*. 1991;5(1):49-59.

14. Fossum S, Crooke E, Skarstad K. Organization of sister origins and replisomes during multifork DNA replication in Escherichia coli. *EMBO J*. 2007;26(21):4514-4522. doi:10.1038/sj.emboj.7601871.

15. Withers HL, Bernander R. Characterization of dnaC2 and dnaC28 mutants by flow cytometry. *J Bacteriol*. 1998;180(7):1624-1631.

16. Ferullo DJ, Cooper DL, Moore HR, Lovett ST. Cell cycle synchronization of E.coli using the stringent response, with fluorescence labelling assays for DNA content and replication. *Methods*. 2010;48(1):8-13. doi:10.1016/j.ymeth.2009.02.010.Cell.

17. Akerlund T, Nordstrom K, Bernander R. Analysis of cell size and DNA content in exponentially growing and stationary-phase batch cultures of Escherichia coli. *J Bacteriol*. 1995;177(23):6791-6797. doi:10.1128/JB.177.23.6791-6797.1995.

18. Greif D, Wesner D, Anselmetti D, Regtmeier J. High-Resolution Imaging of Dried and Living Single Bacterial Cell Surfaces: Artifact or Not? *Micros Today*. 2011;19(5):22-25. doi:10.1017/S1551929511000836.

19. Chao Y, Zhang T. Optimization of fixation methods for observation of bacterial cell morphology and surface ultrastructures by atomic force microscopy. *Appl Microbiol Biotechnol*. 2011;92(2):381-392. doi:10.1007/s00253-011-3551-5.

20. Valkenburg JAC, Woldringh CL. Phase separation between nucleoid and cytoplasm in Escherichia coli as defined by immersive refractometry. *J Bacteriol*. 1984;160(3):1151-1157.

21. Bakshi S, Choi H, Rangarajan N, Barns KJ, Bratton BP, Weisshaar JC. Nonperturbative imaging of nucleoid morphology in live bacterial cells during an antimicrobial peptide attack. *Appl Environ Microbiol*. 2014;80(16):4977-4986. doi:10.1128/AEM.00989-14.

Atomic Force and Fluorescence Microscopy investigation of *Lactobacillus rhamnosus* type I toxin

Introduction

The genetic information, in addition to being contained in the bacterial chromosome, can be also contained in plasmid, small circular DNA molecule capable to replicate independently. They do not accommodate any of the set of core genes needed by the cell for basic growth and multiplication, but rather carry genes that may be useful periodically to enable the cell to survive to particular environmental situations. Among the genes, usually encoded onto plasmids, there are those that confer resistance to antibiotics, to a number of toxic heavy metals and virulence determinants that permit invasion of and survival in animal systems and functions that enhance the capacity to repair DNA damage [1]. Despite their extrachromosomal status, bacterial plasmids are stably maintained in the bacterial population. The stable maintenance may be due to a high copy number of the elements in each bacterial cell. However, in low-copy-number plasmids, stable inheritance depends on the presence of systems that prevent the formation of plasmid-free progeny: a site-specific recombination systems, an active partition process and plasmid addiction systems [2].

The ParA/B systems are responsible for active partition process among bacteria and it consists of only two proteins, ParA and ParB, that drive the transport and equipartitioning of low-copy-number plasmid. ParA is an ATPase that dimerizes and binds plasmid DNA nonspecifically upon ATP binding. Multiple copies of ParB bind to a cis-acting DNA sequence named ParS and stimulate the ATPase activity of ParA upon interaction. Several mechanisms underlying the ParA/B-driven spatial patterns have been proposed however the exact mechanism is still unclear[3].

Independently of the processes that increase the probability of receiving a plasmid by a dividing cell, there are very special strategies adopted by plasmids preventing plasmid-free segregants from surviving.

The idea of an "addiction" mechanism leading to very efficient plasmid maintenance comes from Koyama [4]. He pointed out that if cells that lose an established plasmid die, the population would never contain viable cured cells.

Terms like killer system, killing-antikilling, post-segregational killing, toxin-antitoxin, poison-antidote, plasmid addiction system or programmed cell death are all used to describe the situation when the host cell is selectively killed if it has not received any copy of the plasmid. The molecular basis of such regulated killing mechanism requires the existence of at least two plasmid genes: one specifying a stable toxic agent and another coding for an unstable factor which prevents the lethal action of the toxin [5]. Currently, TA systems are assigned to five classes (I–V) according to their genetic structure and regulation. In type I and III TA modules the antitoxins are small noncoding RNAs, while the antitoxins of the other TA classes are small proteins [6].

Type I TA

Two examples for type I TA systems that were discovered in the 1980s and have been studied in great detail are located on plasmids, hok/Sok in *E. coli* and fst/RNAII in *E. faecalis*.

The first type I toxin-antitoxin module discovered was the Hok-Sok system of R1 plasmids through the characterization of a locus that stabilized various gram-negative bacteria plasmids [5].

This locus codes for three genes, hok ,sok and mok (figure1).

The Hok toxin is a 52 amino acids membrane protein whose overproduction kills bacteria by damaging the inner cell membrane. The damaged membrane leads to efflux of small molecules, in particular, ATP, conferring rapid cell death [7].

The *sok* gene (suppression of killing) codes for a 64 nucleotides (nt) antisense RNA complementary to the Hok mRNA leader region. Sok-RNA is an unstable molecule

constitutively expressed from a relatively strong promoter. On the contrary, Hok mRNA is very stable and is constitutively expressed from a relatively weak promoter [7].

The *mok* (modulation of killing) reading frame overlaps extensively with hok-RNA, and it is required for Hok translation (Figure 1): the ribosome translating Mok continues to the end of the *mok* reading frame, thereby exposing the *hok* translation initiation region and allowing a different ribosome to be loaded there [8].

The *hok* mRNA exists in two forms (Figure 1): the first one appear right after transcription and is denoted full-length *hok* mRNA. In this configuration the 5' and 3' end are paired and the Shine-Dalgarno sequence of *hok* (SD_{hok}) is sequestered by the *dcb* (downstream complementary box) and the antisense RNA recognition element in *hok* mRNA (*sokT*) is not accessible to antitoxin. Under this configuration the mRNA is translationally inactive and binds the antisense RNA very inefficiently. Since the mRNA is inert, it can accumulate inside the host cells without killing it, and simultaneously avoids inactivation due to the antisense RNA binding.

A second configuration of the *hok* mRNA is generated by slow 3' processing of the full-length mRNA (Figure 1). The 3' processing leads to removal of the 40 terminal nucleotides of the full-length mRNA , which disrupts the 5'-3' pairing triggering refolding of the mRNA 5'. The refolding of the 5' end of hok mRNA was accompanied by significant structural rearrangements in the translation initiation regions leading to a stem-loop structure formation with sokT on the apex. Sok RNA recognizes sokT via its 5' single-stranded region by a one-step binding mechanism. After the initial recognition reaction between the RNAs, they form a more extensive duplex [2]. Since the duplexes are rapidly cleaved by RNase III, antisense RNA binding confers irreversible mRNA inactivation and decay [9].
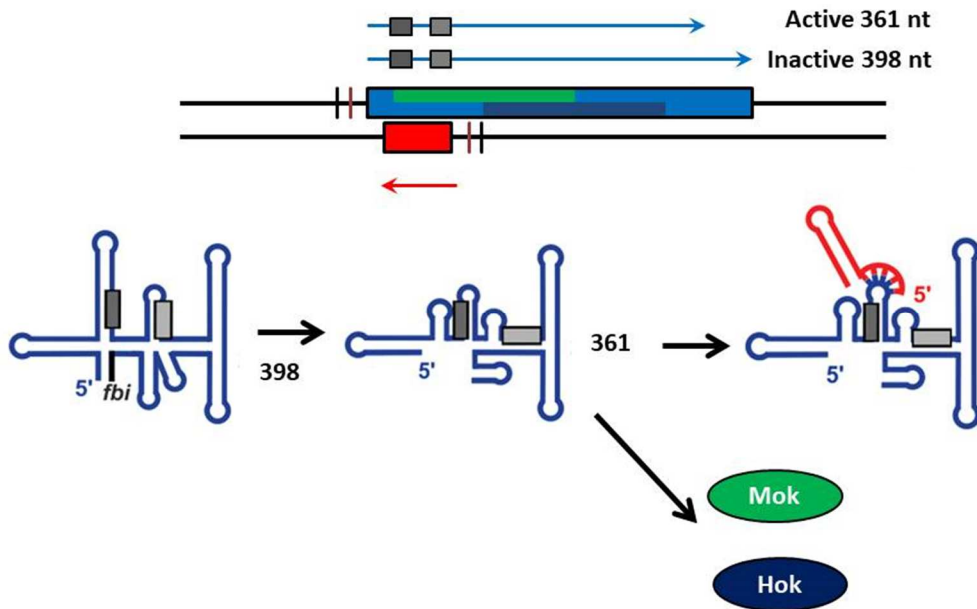
Figure 1. Schematic genetic organization of the Hok-Sok locus (top). Mok (green box) and Hok (dark blue box) are transcribed by the same promoter(-35 is the black line and the -10 is the dark red line). Sok RNA (Red box) is transcribed, from an *mok* internal promoter, in the opposite direction. The full length Moc-Hok RNA is folded in an inactive structure(bottom, blue structure). upon, partial degradation the RNA reorganize and exposes the antisense RNA recognition element on the top of the hairpin and the Hok SD (light gray box), leading to Mok and Hok toxin production(blue and green oval). In presence of the Sok RNA (red structure)the sokT region lead to assembly of the two RNAs molecule leading to duplex formation and degradation of the complex.

The *par* post-segregational killing locus present on *E. faecalis* plasmid pAD1 was the first Type I toxin-antitoxin system described in Gram-positive bacteria [10].

The *par* RNAs (RNA I$_{pAD1}$ and RNA II$_{pAD1}$) are convergently transcribed and share a bidirectional intrinsic terminator that comprises 35 bp (Figure 2), providing a region of complementarity at which the two RNAs can interact[11]. A second region of complementary is constituted by the presence of a pair of direct repeats, DRa and DRb. Both sequences are essential for proper regulation of Fst $_{pAD1}$ toxin translation [10].

In contrast to hok, RNA I $_{pAD1}$ does not appear to adopt alternate structures that control RNA interaction, degradation, and translation. RNA I $_{pAD1}$ possesses two structures, 5'-

stem-loop (SL) and 5'-Upstream helix (UH) impacting *par* $_{pAD1}$ function. 5'-SL is a stem-loop that is postulated to temporarily inhibit ribosome binding, sequestering the SD, until the terminator loop is transcribed [11].

The 5'-UH sequesters the 5' nucleotides from digestion by cellular RNases increasing its life time [10]. The binding of the two RNAs molecule is initially mediated by the terminator loops and then the pairing region is extended to the DRa and DRb repeats (Figure 2), sequestering the initiation codon, interfering with ribosome binding, and inhibiting translation of the toxic peptide Fst $_{pAD1}$ [12]. In contrast to hok/sok system, the interaction of the *par*$_{pAD1}$ RNAs leads to stabilization and accumulation of the RNA I$_{pAD1}$-RNA II$_{pAD1}$ complex. The lower stability of RNA II$_{pAD1}$ suggests that it is preferentially removed from the complex and degraded. However, clear evidence relative to this mechanism are still unknown [11].

Since *in vitro* results suggest that the complex does not spontaneously dissociate the RNA II$_{pAD1}$ removal must be active, and could involve RNA helicase and/or targeted RNase action [11].
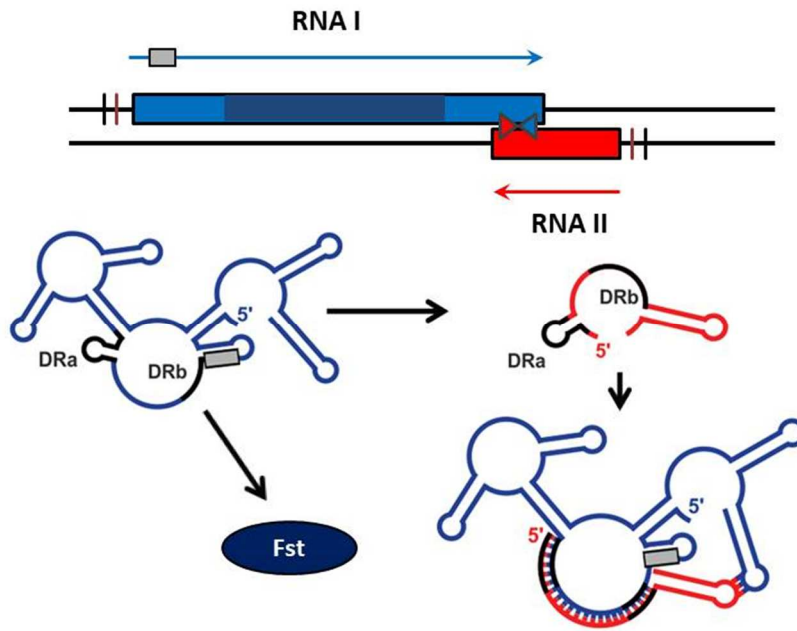
Figure 2. Schematic genetic organization of the *par* locus (top). RNAI (blue box) and RNAII (dark blue box) are transcribed by inverse promoter (-35 is the black line and the -10 is the dark red line) in a convergent direction with a common terminator region (triangle).RNAI is able to fold in a unique structure leading to expression of Fst toxin (blue oval). In presence of RNAII the shared terminator (located on the RNAI and RNAII hairpin apex) mediate the first binding event that subsequently leads to an extended RNA duplex formation thanks to two complementary sequence (black segments).

Toxin effect

Typical type I toxins are very small hydrophobic peptides. All currently known hydrophobic type I toxins have an identical predicted or experimentally confirmed secondary structure containing an α-helical transmembrane domain and are supposed to be localized in the cell membrane [13].

It has been demonstrated that overexpression of Hok leads to formation of 'ghost' cells, which are characterized by condensed cell poles and a centrally located clearing resulting in cell death [5]. For this reason, Hok proteins are usually supposed to kill cells by causing irreversible damage to the cell membrane. In accordance with this observation, Hok overexpression leads to the collapse of membrane potential, respiratory arrest, and both efflux and influx of ions and small molecules [2]. Overexpression of the pAD1-encoded Fst toxin from *E. feacalis* [14] is not only toxic in its original host but also in several bacilli, including *B. subtilis* and in *S. aureus* [15,16].

Toxicity can also be detected in *E. coli*, when the 5' SL of *fst* mRNA is deleted [17], indicating that Fst does not have a host-specific target.

Fst overproduction in both *B. subtilis* and *E. coli*, causes an elongation of cells due to the inhibition of cell division at an early time point, in *S. aureus* the division septa remains structurally incomplete, *E. faecalis* misplaced septa generates daughter cells with little or without DNA, indicating a segregation defect [15].

Recently, it was proposed that Fst induces upregulation of energy-requiring membrane transporters (pumps), although very different physiological alterations has been observed under Fts overexpression, the condensation of the nucleoid represents a common and relevant effect detected in all four bacterial species [15].

***Lactobacillus rhamnosus* TA system**

The *L. rhamnosus* TA locus was identified as overexpressed sequence in a set of genes related to the growth of L. *rhamnosus* in a cheese-like medium identified by cDNA-amplified fragment length polymorphism (cDNA-AFLP)[18].

By means of bioinformatics tools, two small convergently transcribed RNAs (RNA I and RNA II), were identified.

RNA I encodes a 29 amino acids hydrophobic peptide with a putative role of toxin named *Lactobacillus* plasmid toxin (Lpt) displaying high similarity with Fst $_{pAD1}$ toxin (E = 2 × 10−17). Both RNA I and RNA II contain a 24 nt highly complementary sequence (DR) that may be involved in molecular interaction. Secondary structure prediction of RNA I and RNA II suggests folds which are similar to those proposed for toxin and antitoxin RNAs in the Fst TA system. In the structural model of the Lpt-encoding RNA a putative UH is identified at the 5' end, followed by a SL region that includes most of the RBS sequence. The RNA I DR sequence includes the Lpt start codon and is located in a paired region characterized by a low pairing stability, whereas the antitoxin RNA II DR sequence is mainly located in a single stranded region (Figure 3). By analogy with the Fst TA system, the authors suggest that the Lpt toxin synthesis is controlled by two different mechanisms of translation inhibition: an intramolecular regulation involving SL region capable of targeting the RBS sequence, and an intermolecular mechanism mediated by the interaction between complementary DR sequences of RNA I and RNA II [18].
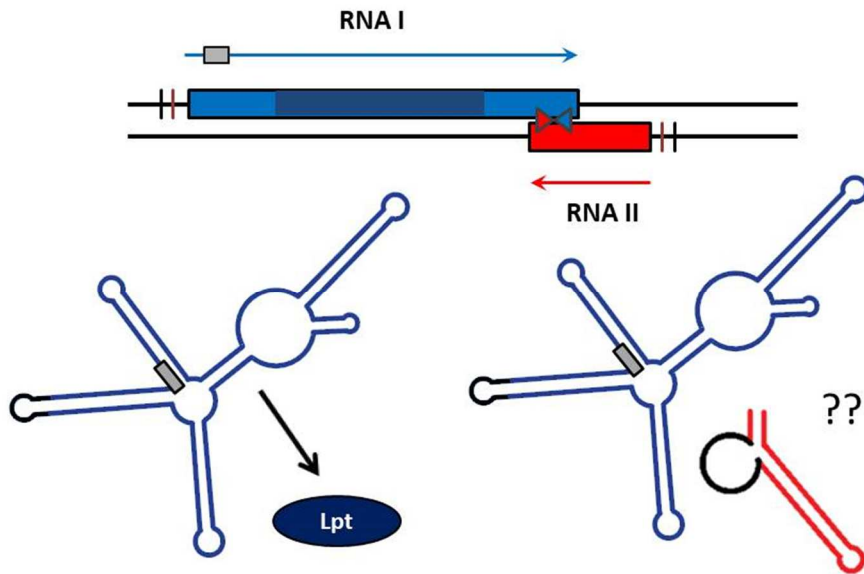
Figure 3. Schematic genetic organization of the *lpt* locus (top) resembling the *par* loculs. RNAI is able to fold in a unique structure leading to expression of Lpt toxin (blue oval). As for the par system, presence of RNAII molecule could lead to a repressive RNA complex but the molecular mechanism is yet to be defined.

Research purpose

Having regard to the good level of similarity between Lpt and Fst I studied the expression effect of Lpt in order to understand the effect of this peptide. *L. rhamnosus* lacks efficient expression vector with a very low basal expression level. This is a key feature due to the strong selective pressure exerted by expression of a toxic protein, even at small concentration.

Therefore I choose to study the effect of overexpression of the Lpt protein in *E. coli* c41(DE3) strain.

E. coli C41 is frequently used to overcome the toxicity associated with overexpressing recombinant proteins using the bacteriophage T7 RNA polymerase expression system[19].

Result and Discussion

In order to employ the C41 expression strain, the protein has been sub-cloned from pSRKKm to pET 11b+.

Similarly to the observations in DH10b strain, the expression of the toxin in C41 strain caused a delayed cell growth with respect to C41 cells without plasmid (Figure 4A).

Given the negative effect on the membrane integrity and on the nucleoid morphology of the Lpt sequence analogue, I analyzed the impact of the toxin expression by means of Atomic Force and fluorescence microscopies.

In the majority of the cells imaged, the expression of toxin caused the appearance of a central clear zone in bright-field images resembling the "ghost cell" produced by Hok expression. Nucleoid localization inside the cells, was determined by staining the sample with DAPI (as described in Materials and Methods chapter).

The images acquired with the fluorescence microscope revealed that the nucleoid is located exactly in the translucent zone and is considerably compacted with respect to the non-induced control. In the non-induced sample there is a great variability of the calculated areas, while after induction the nuclei are compact at an average value of 78 pixels^2.

In order to detect membrane integrity defects, I used a combined Ethidium bromide/ DAPI staining with subsequent AFM cell analysis.

Ethidium bromide is known to be excluded from cells with intact membranes staining only nucleic acids inside damaged cells [20]. Conversely, DAPI can permeate both intact and damaged cells where it binds the DNA minor groove. Staining has been optimized in order to detect the nucleoid compaction by avoiding DAPI and Ethidium bromide signal overlapping.
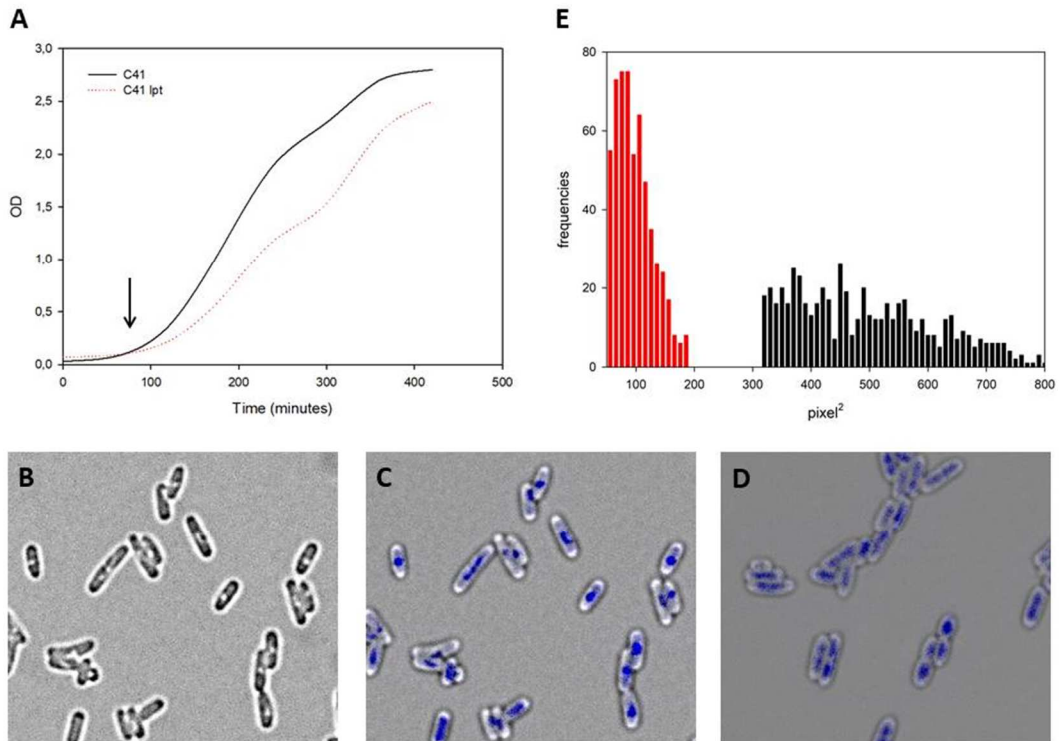
Figure 4. A) Growth curve of C41 wt and C41*lpt* containing strains(IPTG wa added at the arrow indicating point).**B)** bright-filed images taken 1 hour after Lpt induction. it's clearly visible the central transparent region. **C)** overlapped bright-filed(gray)-florescent(blue) images taken 1 hour after Lpt induction**. D)** overlapped bright-filed(gray)-florescent(blue) images of the pre-induction C41*lpt* strain. **E)** Histograms of the detected nucleoid areas. The non-induced nucleoid(black bricks) occupies a large distribution of values, spanning from 350 to 830 pixels^2. The 1 hour induced sample diplay a peak distribution centered on a 78 pixel^2 value indicating at least a five-fold decreasing in nucleoid occupied area.

This analysis revealed that the Lpt expression caused a relevant Ethidium bromide entry into the cells up to two hours after the toxin induction. Interestingly, after three hours of induction, the permeability of the cells is comparable to that the pre-induction state, with a clear predominance of cells that did not internalize Ethidium bromide.

In order to rule out that the return to pre-induction state was not due to the loss of efficacy of the inducer, IPTG was added every hour after sampling at a final concentration

of 1 mM. Independently of this precaution, the majority of the bacterial cells were able to recover membrane integrity after three hours.
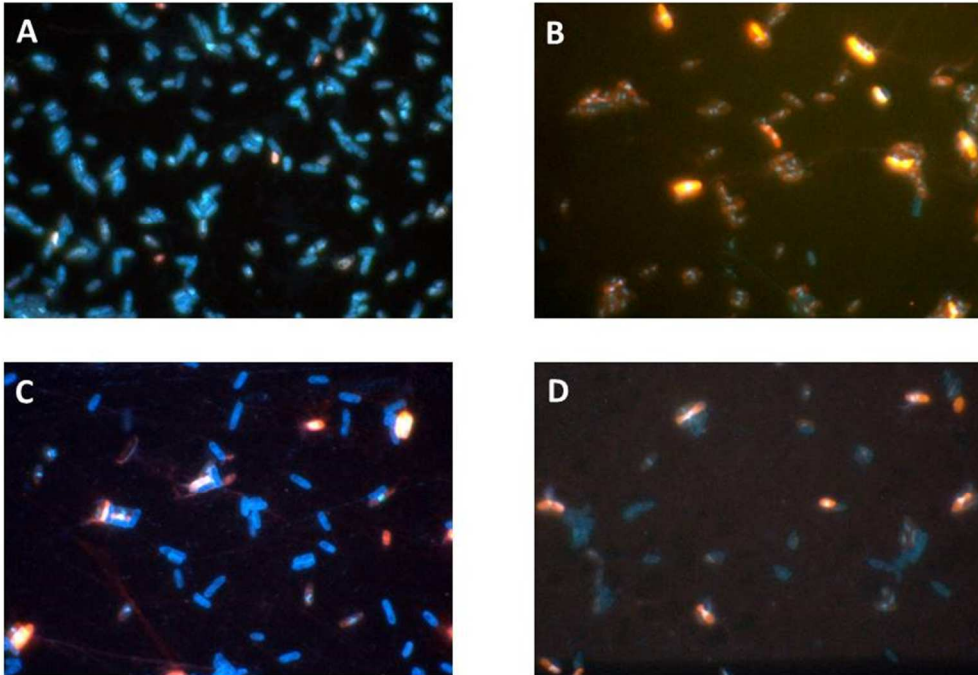

Figure 5. A) fluorescence image of *E. coli* c41 collected before induction; **B)** after 1 hour of induction; **C)** after 2 hour of induction and D) after 3 hour of induction of the Lpt petide. in all the sample the cells were stained with DAPI and Ethdium-bromide.

Given the high compaction frequency of the nucleoid and the subsequent recovery of membrane integrity after three hours, it is possible that the toxin induction causes a reversible stalemate of bacterial growth rather than death. Similarly to Hok toxin, Lpt expression could cause membrane pores that dissipate the proton motive force (PMF), expression of the phage shock proteins (Psps) and proteorhodopsin can buffer the negative effect of toxin expression [21,22].

In order to reveal pore-like structure on the cellular surface, I employed the high surface resolution of AFM.

AFM images demonstrated that the translucent zone was actually a depression of about 40-60 nm.

Thanks to the coupling of fluorescence microscopy with AFM, it was possible to exactly correlate the permeability differences with a change in morphology(Figure 6); the cells that incorporate more Ethidium are found to be 'deflated', with a height below 100nm, and exhibit the highest degree of surface deformity visible as 'holes-like structures' (Figure 7).
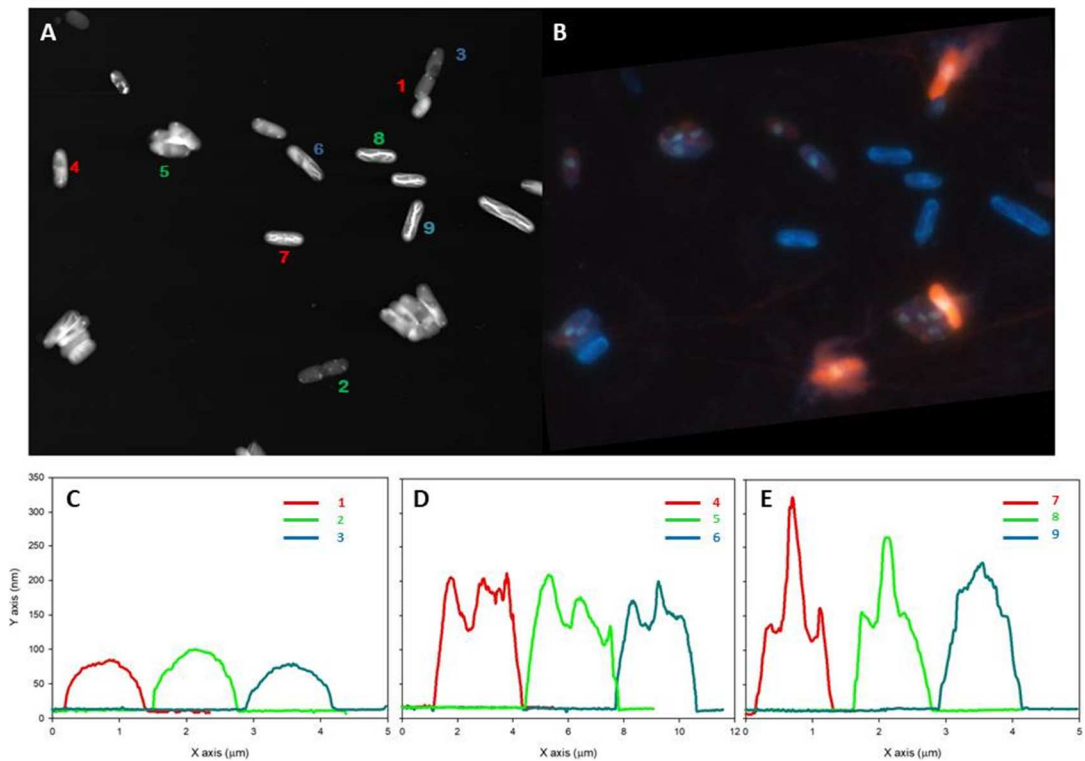

Figure 6. Atomic force(A) and flurescence microscopy (B) of C41 Lpt cells after 1 hour form the induction and stained with DAPI and Ethidium bromide. On the bottom it is reported the profile of three cells displaying a high (C); an intermediate D) and low E) degree of red fluorescence
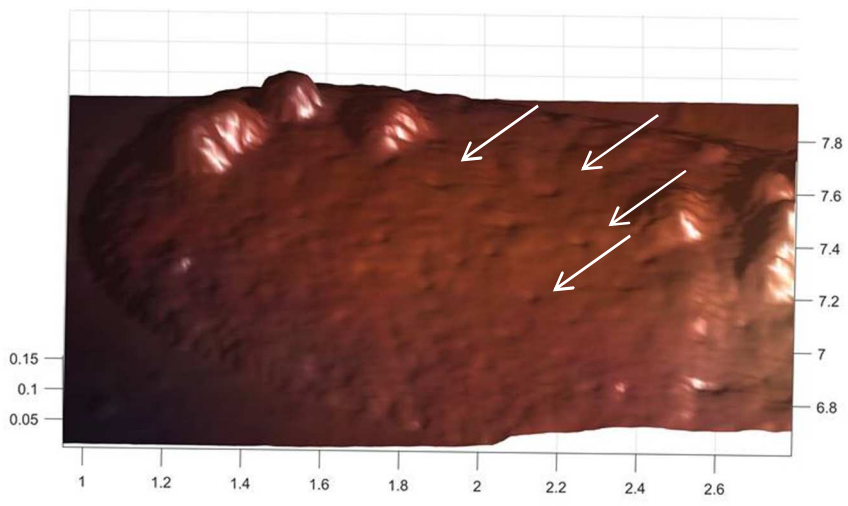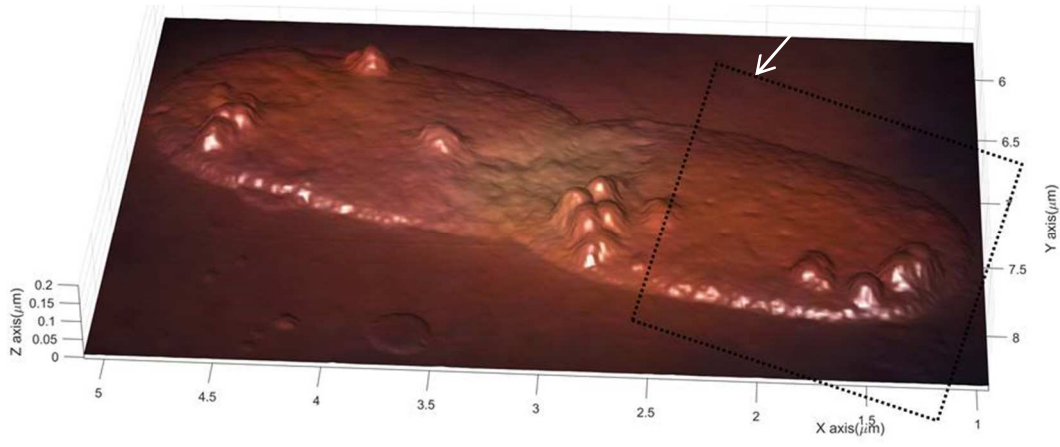
Figure 7. Atomic force three dimensional data integrated with fluorescence microscopy image of a C41 Lpt exhibiting high morphological damage (blebs ad 'holes-like structures') coupled with a high level of Ethidium-bromide fluorescence(top), magnification of the marked area displaying holes-like structures indicated from the white arrows (bottom). The values on Cartesian axes are expressed in micrometers.

Probably these cells produce a greater amount of Lpt peptide that damages not only to the internal but also to the external membrane, leading to the bacterium death.

Cells that have the compact nucleoid structure and lower Ethidium-induced fluorescence were 150-200 nm tall with deformations similar to blebs, usually associated with the action of antimicrobial peptides [23]. Since no 'holes-like structures' were observed on the surface of these cells, possible defects could occurred in the internal membrane. Interestingly, cells that did not show induction signs showed a very similar morphology to that described in Chapter 3 with a central ridge overlapped by the fluorescence signal.

Conclusion

Both AFM and fluorescence microscopy images suggest that the Lpt toxin acts at the membrane level, causing an alteration of membrane integrity, perturbation of the membrane permeability and formation of blebs and 'holes-like structures' that, in most cases, leads to cell death figure.

A reversible collapse of the nucleoid structure was also detected. This phenomenon has already been observed in other toxins even if the molecular mechanisms have not been studied. Nucleoid compaction may be a passive phenomenon due to the exit from the cell of essential elements, such as Mg^{2+} or Ca^{2+}, or the perturbation of the correct localization of proteins critical in nucleoid proper folding.

Materials and methods

Lpt subcloning

The coding sequence of Lpt peptide was extracted form pSRKKm-lpt plasmid using the restriction enzyme NdeI-BamH1 (New England Biolabs) and ligate with a pET 11b(+) plasmid previously digested with the same restriction enzyme. the ligation was used to transform Escherichia coli (DE3) C41 strain by electroporation. the verification of the presence of the Lpt peptide was confirmed by colony PCR using T7 universal primers.

Sample preparation

A starter culture of *Escherichia coli DE3 c41(Lpt)* was obltein from an over-night LB growth culture from stab. The starter culture was diluted at an OD_{600} of 0,06 to restart the growt. The production of Lpt protein was induced at an OD_{600} of 0,2. After one to three hours 2 mL of culture were collected at 13K rpm for 1 minute, washed 3 times with 2 mL of PBS 1X and then suspended in 100 μL of PBS. For cell staining the cells were incubated with 10μg/mL of DAPI (4',6-diamidino-2-phenylindole) for 5 minutes alone or in combination with 10μg/mL of Ethidium-Bromide. After incubation, the cell volume was carried to 1 mL with PBS 1X and washed twice with PBS 1Xpellets after the last centrifuge is resuspended in 50μL of PBS 1X.

A volume of 50 μL of this solution was deposited onto a pre-functionalized glass coverslip (as described in the materials and method in chapter 3). I refer to the paragraph materials and methods in the chapter for the part of microscopy and image processing.

Bibliography

1. Bennett PM. Plasmid encoded antibiotic resistance: Acquisition and transfer of antibiotic resistance genes in bacteria. *Br J Pharmacol*. 2008;153(SUPPL. 1):347-357. doi:10.1038/sj.bjp.0707607.

2. Gerdes K, Gultyaev AP, Franch T, Mikkelsen ND. ANTISENSE RNA-REGULATED. 1997:1-31.

3. Surovtsev I V., Campos M, Jacobs-Wagner C. DNA-relay mechanism is sufficient to explain ParA-dependent intracellular transport and patterning of single and multiple cargos. *Proc Natl Acad Sci*. 2016;113(46):E7268-E7276. doi:10.1073/pnas.1616118113.

4. Koyama AH, Wada C, Nagata T, Yura T. Indirect selection for plasmid mutants: isolation of colVBtrp mutants defective in self maintenance in Escherichia coli. *J Bacteriol*. 1975;122(1):73-79.

5. Gerdes K, Larsen JEL, Molin S. Stable inheritance of plasmid R1 requires two different loci. *J Bacteriol*. 1985;161(1):292-298.

6. Unterholzner SJ, Poppenberger B, Rozhon W. Toxin-antitoxin systems. *Bioengineered*. 2014;5(3):1-13. doi:10.4161/mge.26219.

7. Gerdes K, Thisted T, Martinussen J. Mechanism of post-segregational killing by the hoklsok system of plasmid R1: sok antisense RNA regulates formation of a hok mRNA species correlated with killing of plasmid-free cells. *Mol Microbiol*. 1990;4(11):1807-1818. doi:10.1111/j.1365-2958.1990.tb02029.x.

8. Thomas Thisted; Kenn Gerdes. Mechanism of post-segregational killing by the hok/sok system of plasmid R1: Sok antisense RNA regulates hok gene expression indirectly through the overlapping mok gene. *J Mol Biol*. 1992;223(1):41-54. doi:10.1016/0022-2836(92)90714-U.

9. Kenn Gerdes, Allan Nielsen, Peter Thorsted EGHW. Mechanism of killer gene activation. Antisense RNA-dependent RNase III cleavage ensures rapid turn-over of the stable Hok, SrnB and PndA effector messenger RNAs. *J Mol Biol*. 1992;226(3):637-649. doi:10.1016/0022-2836(92)90621-P.

10. Weaver KE, Clewell DB, An F. Identification, characterization, and nucleotide sequence of a region of Enterococcus faecalis pheromone-responsive plasmid pAD1 capable of autonomous replication. *J Bacteriol*. 1993;175(7):1900-1909.

11. Weaver KE. The par toxin-antitoxin system from Enterococcus faecalis plasmid pAD1 and its chromosomal homologs. *RNA Biol*. 2012;9(12):1498-1503. doi:10.4161/rna.22311.

12. Greenfield TJ, Franch T, Gerdes K, Weaver KE. Antisense RNA regulation of the par post-segregational killing system: Structural analysis and mechanism of binding of the antisense RNA, RNAII and its target, RNAI. *Mol Microbiol*. 2001;42(2):527-537. doi:10.1046/j.1365-

2958.2001.02663.x.

13. Fozo EM, Hemm MR, Storz G. Small Toxic Proteins and the Antisense RNAs That Repress Them. *Microbiol Mol Biol Rev*. 2008;72(4):579-589. doi:10.1128/MMBR.00025-08.

14. Weaver KE, Jensen KD, Colwell A, Sriram S. Functional analysis of the Enterococcus faecalis plasmid pAD1-encoded stability determinant par. *Mol Microbiol*. 1996;20(1):53-63. doi:10.1111/j.1365-2958.1996.tb02488.x.

15. Patel S, Weaver KE. Addiction toxin Fst has unique effects on chromosome segregation and cell division in Enterococcus faecalis and Bacillus subtilis. *J Bacteriol*. 2006;188(15):5374-5384. doi:10.1128/JB.00513-06.

16. Weaver KE, Weaver DM, Wells CL, Waters CM, Gardner ME, Ehli EA. Enterococcus faecalis plasmid pAD1-encoded Fst toxin affects membrane permeability and alters cellular responses to lantibiotics. *J Bacteriol*. 2003;185(7):2169-2177. doi:10.1128/JB.185.7.2169-2177.2003.

17. Shokeen S, Patel S, Greenfield TJ, Brinkman C, Weaver KE. Translational regulation by an intramolecular stem-loop is required for intermolecular RNA regulation of the par addiction module. *J Bacteriol*. 2008;190(18):6076-6083. doi:10.1128/JB.00660-08.

18. Folli C, Levante A, Percudani R, et al. Toward the identification of a type i toxin-antitoxin system in the plasmid DNA of dairy Lactobacillus rhamnosus. *Sci Rep*. 2017;7(1):1-13. doi:10.1038/s41598-017-12218-5.

19. Dumon-Seignovert L, Cariot G, Vuillard L. The toxicity of recombinant proteins in Escherichia coli: A comparison of overexpression in BL21(DE3), C41(DE3), and C43(DE3). *Protein Expr Purif*. 2004;37(1):203-206. doi:10.1016/j.pep.2004.04.025.

20. Aeschbacher M, Reinhardt CA, Zbinden G. A rapid cell membrane permeability test using flourescent dyes and flow cytometry. *Cell Biol Toxicol*. 1986;2(2):247-255. doi:10.1007/BF00122693.

21. Gerdes K. Hypothesis: type I toxin-antitoxin genes enter the persistence field-a feedback mechanism explaining membrane homoeostasis. *Philos Trans R Soc Lond B Biol Sci*. 2016;371(1707):20160189. doi:10.1098/rstb.2016.0189.

22. Jovanovic G, Lloyd LJ, Stumpf MPH, Mayhew AJ, Buck M. Induction and function of the phage shock protein extracytoplasmic stress response in Escherichia coli. *J Biol Chem*. 2006;281(30):21147-21161. doi:10.1074/jbc.M602323200.

23. Brogden KA. Antimicrobial peptides: pore formers or metabolic inhibitors in bacteria? *Nat Rev Microbiol*. 2005;3(3):238-250. doi:10.1038/nrmicro1098.